Advances in Functional Imaging with Emission Computer Tomography

by

LAU Chi Hoi, BEng(Hons)

A thesis submitted for the Degree of Master of Philosophy

in the Department of Electronic Engineering

of the Hong Kong Polytechnic University

Department of Electronic Engineering

The Hong Kong Polytechnic University

May 1999

To my parents

Abstract

With the advent of technology for emission computer tomography, functional imaging technique, using either Positron Emission Tomography (PET) or Single Photon Emission Computer Tomography (SPECT), provides a powerful tool to yield invaluable information of the physiological processes under study. Based on this technique, quantitative portrayal of both structure and function of these processes are obtained. It has created opportunities for researchers to examine increasingly complex biomedical systems, thereby leading the way to a deeper understanding of fundamental complexities of life. It has also greatly improved the diagnosis and treatment of human diseases.

In spite of the wide applicability in both scientific researches and clinical diagnostic procedures, functional studies are still of limited uses due to a number of factors. For example, the cost of PET scanners is much expensive than the other imaging modalities, which make them not commonly available in most hospitals. Although effort has been made in studying the use of less expensive SPECT scanner to perform the similar dynamic studies, the incompleteness of the projection data introduces artifacts to the reconstructed images which will affect the accuracy of subsequent parameter estimation. Furthermore, little attention has been paid to systematically investigate the scanning duration which usually determined based on clinician's intuition and experience. The slow kinetics of typical SPECT tracers may require unrealistically long total acquisition times to obtain reliable estimation of the slower rate constants. Finally, dynamic PET studies require the measurement of tracer concentration in blood plasma which is invasive, time-consuming and tedious. The blood measurement process also exposes the clinical personnel to the danger of fatal blood infection and radiation.

In this thesis, three different techniques were presented in order to solve the aforementioned limitations. Our primary focus is to develop computationally efficient techniques to minimize the inconvenience of performing functional

imaging using emission computed tomography, by means of either PET or SPECT.

In the first part of the thesis, we investigated the possibility of using rotating detector systems to perform functional studies, rather than full ring detector systems. The rotating detector systems are usually of much lower cost than the full ring detector systems. We study the problem of parameter estimation using measurements recorded by rotating detector systems and propose an approach to improve the accuracy of parameters estimated using the above detector systems. The method involves interpolation across projections so as to provide an improved estimate of the projections, closer to those which would be obtained for a stationary detector system. The interpolated projections are then reconstructed using the conventional filtered back-projection (FBP) algorithm and the kinetic parameters are estimated using a weighted least squares cost function based on the integral of activity. The proposed method is based on several previously validated techniques which, in combination, provide a simple and computationally efficient solution.

The second part of the thesis is to systematically investigate the reliability of parameter estimation as a function of total acquisition time, with Thalium-201 (Tl-201) dynamic SPECT as our typical example. We also suggest and evaluate a clinically practical alternative to prolonged continuous dynamic acquisitions. In addition, the minimum number of frames and their duration are investigated using the optimum sampling schedule (OSS) technique. While this study concentrates on applying the methodology to Tl-201 kinetics, the methodology developed here is also applicable to other dynamic SPECT studies.

In the final part of the thesis, we propose an approach to estimate the parameters of a pre-assumed tracer kinetic model when performing dynamic studies, eliminating the requirement of measuring the tracer concentration in blood sampling. The approach involves a denoising step for the projection data. In our case, we use a wavelet denoising approach, given its advantage of preserving the

structural information of the image when filtering the noise. The denoised projections are then reconstructed using the FBP. From the reconstructed dynamic images, tissue time activity curves (TTACs) are extracted from regions of interest (ROIs) and are re-sampled using linear interpolation. Based on these TTACs, an eigen-vector based blind deconvolution technique is applied to estimate the kinetic parameters.

On the whole, the aim of these studies is to develop computationally efficient algorithms to reduce the inconvenience associated with functional studies using emission computed tomography. We hope that such studies can be more commonly and extensively used in both scientific researches and clinical environments.

Acknowledgments

There have been many individuals along the way who have offered encouragement, time and support to me. I would like to take this opportunity to express my sincere gratitude to each of them.

First of all, I would like to thank my chief supervisor, Dr Daniel Lun P. K., for his support and guidance during both my undergraduate and graduate studies. His open-mindedness allows me to freely purse my interests and explore new research areas. I am very grateful for his constant encouragement and his perspectives on life at large.

I would also like to thank my co-supervisor, Prof. David Feng D.. I am benefited tremendously from his professional advice and vision. In addition, his plentiful experience in the way of life is also a precious knowledge which I have learnt. I deeply believe that they will be very much useful in my future study and career.

I am also thankful to Prof. Siu W. C., Head of the Department of Electronic Engineering, the Hong Kong Polytechnic University. This study could not reach its present level without his constant and kindly support.

In addition, I am greatly indebted to Brain F. Hutton, who is the physicist of the Department of Medical Physics in the Westmead Hospital, Stefan Eberl, Steven Mekel and Roger Futon, who are the physicists of the Department of Nuclear Medicine in the Royal Prince Alfred Hospital. Their expert knowledge has helped me to overcome many difficulties in my studies. I would also like to thank my friends and colleagues at the Hong Kong Polytechnic University for their friendship and support, in particular, Dr Chan Y. L., Dr Bity Chau L. P., Dr Clifford Choy S. T., Mr Stephen Choy, Mr Philip Hong S. W., Mr Hsung T. C., Mr Hui W. L., Dr James Kwok, Mr Stephen Kwok, Mr Cleve Ku, Mr Barry Leung, Ms Li W., Ms James Lu, Dr Ser P. K., Mr Shen T. W., Mr Jamin Tse, Mr

Wong K. P., Mr Wong W. H., and those who have worked with me in these years. It has been a wonderful time for me to work with them.

A special note of heartfelt goes to Melanie Chan for her love, encouragement and support over the years. She has been a constant source of inspiration. Her persistent effort in persuading me to purse a higher degree made this thesis possible.

Finally, I must express my sincere gratitude to my parents, my elder brother and sister for their endless support and encouragement. Without them, this study would not have the chance to be completed.

Statement of Originality

The following contributions reported in this thesis are claimed to be original.

1. A novel approach is proposed for estimating kinetic parameters from dynamic studies recorded by rotating detector systems. (Chapter 3, Section 3.2)

   By using this approach, artifact-free dynamic images, reflecting the bio-distribution of radio-pharmaceuticals within the body, can be obtained by using projection data acquired with rotating detector systems. The proposed approach can also provide parameter estimates comparable to those obtained with a full ring detector system, as is typical of conventional Positron Emission Tomography (PET). The approach suggested here is intrinsically simple. It is not computation intensive compared with methods where modeling is performed directly from projections and, therefore, it has appeal for general clinical application. In addition, this technique should also be applicable to data acquired using systems such as single or multi-detector Single Photon Emission Computed Tomography (SPECT), coincidence detection or low-cost PET systems which involve detector rotation rather than a stationary ring of detectors.

2. A methodology for determining the duration of image acquisition time and for optimizing sampling schedule of dynamic SPECT studies is developed. (Chapter 4, Section 4.2 and 4.3)

   The methodology developed here provides a means for determining the image acquisition time and for deriving an optimum sampling schedule for dynamic SPECT study, such that a reliable estimation of all parameters of interest can be obtained. The methodology applied here to Thalium-201 (Tl-201) should also be applicable to other SPECT tracers.

3. A clinically practical alternative, consisting a short dynamic at the start of the study and a short delayed scan, to prolonged continuous dynamic

acquisitions is proposed for Tl-201 dynamic SPECT study. (Chapter 4, Section 4.2)

For continuous data acquisition sampling schemes, it is found that accurate estimates of the volume of distribution (Vd) required an acquisition time of at least 90 minutes. This is clearly impractical for routine clinical studies and difficult for patient to tolerate. We thus suggested and evaluated an alternative sampling scheme, based on a short dynamic at the start of the study and a short delayed scan. It is found that, with an additional scan at approximately 3 hours, the initial dynamic can be reduced to 30 minutes and we can still achieve similar accuracy for Vd as a continuous 120 minutes acquisition. The time requirements for the split session sampling scheme are similar to current Tl-201 rest/redistribution studies, and are thus clinically practical. Further, estimation of blood flow related parameter, K_1, and Vd should eliminate the need for 24 hours images, which may in fact reduce the total study time.

4. An approach is proposed for the quantification of dynamic PET study, obviating the requirement of blood sampling. (Chapter 5, Section 5.2)

By using the proposed approach, we can estimate the rate constants for a pre-assumed tracer kinetic model using only the tissue time activity curves (TTACs). The advantages of the approach include: (1) simplification of the procedure for performing functional imaging; (2) markedly reduced radiation exposure to the blood sampler; (3) non-invasiveness; and (4) minimization of fatal blood infection. Furthermore, although we applied the proposed technique specifically to the tomographic studies based on [^{18}F] labeled fluoro-deoxy-glucose (FDG) model, the proposed technique can potentially be applied to other tracer kinetic model.

List of Figures

List of Tables

Author's Publications

International Conference Papers

1. Chi-Hoi Lau, Dagan Feng, Daniel Pak-Kong Lun, Wan-Chi Siu, "Tomography Dynamic Imaging and System Identification with Partially Sampled Noisy Radio-active Signal", Proceedings of the IEEE Region 10 Conference, Perth, Australia, 25-28 Nov., 1996, Vol. 1, p. 462-467 1996.

2. Stefan Eberl, Chi-Hoi Lau, Dagan Feng, Hidehiro Iida, Pak-Kong Lun, Wan-Chi Siu, Geroge J. Bautovich, "Optimum Sampling Schedule for Tl-201 Dynamic SPECT", 44th Annual Meeting, Society of Nuclear Medicine held at Texas, U.S.A., 1-6 June, 1997, Journal of Nuclear Medicine, Vol. 38, No. 5(supplement), p. 223p, 1997.

3. Chi-Hoi Lau, Daniel Pak-Kong Lun, Dagan Feng, "Non-Invasive Quantification of Physiological Processes with Dynamic PET using Blind Deconvolution", Proceedings, IEEE International Conference on Acoustics, Speech and Signal Processing, Vol. 3, p 1805-1808, Seattle, Washington, U.S.A., 12-15, May, 1998.

Recent Submissions

1. Chi-Hoi Lau, Dagan Feng, Daniel Pak-Kong Lun, Wan-Chi Siu, "Techniques for Image reconstruction and Kinetic Modelling from Rotating Camera Systems", IEEE Transactions on Medical Imaging, accepted 9/1998.

2. Chi-Hoi Lau, Stefan Eberl, Dagan Feng, Hidehiro Iida, Pak-Kong Lun, Wan-Chi Siu, Yoshikazu Tamura, Geroge J. Bautovich, Yukihiko Ono, "Minimum Dynamic SPECT Image Acquisition Time Required for Tl-201 Tracer Kinetic Modelling", IEEE Transactions on Medical Imaging, Vol. 17, No. 3, p. 334-43, 1998.

Table Of Content

Chapter 1 Introduction

1.1 Overview of Functional Imaging

With the advent of technology, modern medical imaging techniques create the opportunities of measuring sequence of images in which the intensity of each pixel is proportional to the concentrations of tracers (by emission computed tomography (ECT)), of X-ray absorbing contract materials (fast Computer Tomography (CT)), or of native chemical substances (Nuclear Magnetic Resonance (NMR)) in tissue regions at identifiable locations in three-dimensional space. Mathematical analysis of such image sequence provides a powerful tool to yield valuable insight of the physiological processes under study, giving a quantitative portrayal of both structure and function: such is the approach of functional imaging.

The capability of functional imaging in quantifying physiological processes has created opportunities for researchers to examine increasingly complex biomedical systems, thereby leading the way to a deeper understanding of fundamental complexities of life. For example, Positron Emission Tomography (PET) are used by researchers to relate regions of the brain to various cognitive and visual skills; and also to psychological disorder. Furthermore, functional imaging has also greatly improved the diagnosis and treatment of human diseases. Some clinical applications include its uses in localizing tumor sites, measuring myocardial perfusion, studying various cancers, grading brain tumors, and determining the effectiveness of radiation therapy, chemotherapy, and surgery.

To perform functional imaging, a wide range of imaging modalities are available. In addition to the ECT (either by means of using PET or single photon emission computed tomography (SPECT)), fast CT and NMR described above, other image modalities for performing functional imaging includes: magnetic resonance spectroscopy (MRS), electron paramagnetic resonance imaging

(EPRI), magneo-encephalography (MEG) as well as some other newer techniques such as electrical impedance tomography (EIT), near infra-red imaging, active microwave tomography and laser doppler imaging of blood flow. A survey of these imaging modalities has been given in [1].

Among the various medical imaging modalities, PET is quite unique and has been playing an important role in scientific researches and clinical studies. The development of PET in the 1970's has not only increased the capability to get in vivo measurement non-invasively but also made it possible to quantitatively characterize the features and functions of living processes. The capability of measuring physiological characteristics of human brain and heart, such as blood flow, utilization of oxygen, and the metabolic rate of glucose, has led PET to become a useful patho-physiological and diagnostic tool. With PET, more accurate differentiation of tissues with different local metabolic rate of glucose would aid the early detection of tumors and other abnormalities. Furthermore, improved accuracy of local metabolic rate of glucose estimation would allow PET to measure more reliably a tumor's response to a particular therapy. In clinical studies, PET can provide essential information that cannot be obtained with any of the other imaging modalities, such as, Magnetic Resonance Imaging (MRI) and X-ray CT. They complement PET because they provide mostly anatomical information.

1.2 PET and Functional Imaging

1.2.1 Historical development of PET

The development of PET has involved the efforts of many investigators. Positron imaging was first suggested in 1951 by Wrenn et al [2] and Brownell, as reported by Sweet [3]. The first successful positron scanner was described by Brownell and Sweet in 1953 [4] (also Burham and Brownell in 1972 [5]). In 1959, Anger described his version of a positron imaging device using the scintillation camera [6]. These systems were designed and used for two-dimensional imaging of positron radio-nuclide distributions in the human body.

Transverse-section imaging with positron was first described in 1962 [7,8] with a circular array of 32 NaI(Tl) detectors for studies of the brain. Similarly, Kuhl and Edwards [9] were developing the concept of transverse- and longitudinal-section scanning with single photon emitting radio-nuclides. Anger [10], Muehllehner and Wetzel [11], Todd-Pokropek [12], Bowley et al [13], Tanaka [14], and Burham and Brownell [5] also investigated and developed techniques for performing emission tomography. All these approaches were limited by problems encountered from inadequate mathematical reconstruction algorithm (i.e. none were CT approaches), computational hardware, number of angular views, and image distortions resulting from photon attenuation and statistical limitations. These approaches employed many of the principles of focal plane or blurring tomography originally developed for X-ray techniques by Bocage in the 1930s [15].

In 1973, Kuhl et al [16] presented a paper on quantitative section scanning in which they employed multiplicative correction factors applied to orthogonal scan profiles in an effort to compensate for the blurring present in their section scanning. In 1976, Kuhl et al [17] published an article on the Mark IV scanner, which consisted of a square array of 32 NaI(Tl) detectors employing an exact CT reconstruction algorithm. In 1974, Budinger and Gullberg [18], and in 1975, Kay and Keyes [19], published articles describing the feasibility of single-photon CT with rotating scintillation cameras.

The first positron computed tomography system was developed by Phelps et al in 1975 [20,21]. This system was referred to as the PETT II (Positron Emission Transaxial Tomography). The PETT II consists of a hexagonal array of NaI(Tl) detectors connected in coincidence between bank pairs. It utilizes a Fourier-based CT algorithm, proper sampling and an exact attenuation correction. In 1975 and 1976, these investigators published results from the first whole-body PET (PETT III) which was developed for human studies [21-24]. This system

was subsequently redesigned by Phelps et al [25] and commercially produced as the ECAT.

Since then, numerous PET systems were developed. The principles of the developed PET systems that have been developed were reviewed in details elsewhere [20,26-29]. It is obvious that PET system design has involved a variety of different strategies. However, some concepts of PET system design have achieved general acceptance. Circumferential designs employing hexagonal, octagonal, or circular geometries are preferred because they maximize efficiency in the image plane. This is a key factor since the minimum imaging time is determined by the time required to gather sufficient data for a single plane. Sodium iodide detectors have been replaced by BGO or CsF detectors. The advantages of BGO is its capability of providing high spatial resolution and efficiency while CsF has a short decay time, which can be used to reduce image noise through the use of time-of-flight measurements. Although there are different system design approaches, a properly designed PET scanner can provide analytical measurements of local tissue radio-activity concentrations to allow the use of tracer kinetic techniques.

1.2.2 Advantages of PET

PET was developed for functional imaging because it offers a number of unique features. First of all, the positron-emitting isotopes of carbon (^{11}C), nitrogen (^{13}N), oxygen (^{15}O), and fluorine (^{18}F) can be used to label a wide variety of substances, metabolites, drugs, and other biologically active compounds or their analogs without disrupting their chemical or biochemical properties. Secondly, with PET, the measurement of functional processes in the human is performed non-invasively using external radiation detection and mathematical image reconstruction techniques, leaving the subject under study in an undamaged and undisturbed state. These two features, together with the tracer kinetic models, provide a unique way of measuring local biochemical processes in the human brain.

In addition, the properties of positron decay are well suited to the requirement of CT. In positron decay, the positron annihilates with an electron to emit two 511 keV photons 180° apart. This allows the use of an electronic form of photon collimation by recording simultaneous detection of these photons in opposing detectors. This is referred to annihilation coincidence detection (ACD). ACD provides uniform and high spatial resolution, high detection efficiency, and simultaneous collection of linear and angular data. ACD also provides exact or near-exact methods for photon attenuation and a high degree of geometry discrimination against scattered radiation, factors which reduce quantification and can produce artifacts in CT. These properties allow PET to give a quantitative information of the process under study.

1.2.3 Physiological characteristics that can be obtained by PET

Currently, most of the PET studies are devoted to the analysis of human brain. There are numerous variables that one would like to measure in determining local function of the brain. The primary variables of interest would be cerebral blood flow (CBF), cerebral metabolic rates of oxygen ($CMRO_2$) and glucose (CMRGlu), since they normally form the supply-demand basis of local function in the brain. By assessing such variables, we can obtain an understanding of altered states of cerebral function. In addition, PET can also be used to evaluate specific changes in other processes such as (1) blood-brain barrier transport, (2) cell membrane transport, (3) the distribution of the various receptors involved in excitation or inhibition, and (4) protein synthesis for evaluation of structural degeneration, regeneration, reorganization, or other protein synthesis requirements of cerebral function.

1.2.4 Procedure involved in PET

The application of PET in the quantification of physiological processes requires a number of steps:

1) Labeling a selected compound with a positron-emitting radio-nuclide.
2) Administering the labeled compound to the subject.

3) Estimating the distribution of the labeled compound.

4) Using the estimated distribution to determine parameters of physiological models that provide the information of interest.

The positron-emitting radio-nuclides that are used most often are ^{11}C, ^{13}N, ^{15}O and ^{18}F. These radio-nuclides are used to label compounds such as sugars, amino acids, and neuro-transmitter receptor ligands. Because of their short half-lives, positron-emitting radio-nuclides cannot be stored and must be generated on-site using an accelerator (e.g., cyclotron) which requires a significant amount of capital and technical expertise to maintain.

After it is administered to the subject, the labeled compound is absorbed by various regions of the organ of interest. As the radio-nuclide decays, positrons are emitted in regions of high absorption, and less positrons are emitted in regions of low absorption. For example, labeled glucose is used more by the regions of the brain that are more active when a certain task is performed. Another example is cancerous tissue's utilization of more glucose than healthy tissue. When a positron is emitted, it annihilates with a nearby electron creating two photons that fly off in nearly opposite, random directions.

Surrounding the organ of interest is one or several rings of detectors that are designed such that a count is incremented whenever a pair of detectors senses two photons in coincidence, i.e., the two photons are registered by a pair of detector within a small time interval.

The measurements of observed photons are reconstructed into visual images that each pixel indicates the concentration of radio-nuclide. This process is called image reconstruction. In the beginning, the image reconstruction algorithms were developed based on deterministic projection model and based on Fourier transform techniques. The convolution back-projection (CBP) and direct Fourier reconstruction (DFR) methods are two typical examples of this approach. These algorithms were later found to be sensitive to the perturbation of measurements,

especially in PET where the recorded projections are quite noisy. One way to reduce noise sensitivity is to model the emission process as a random process and develop reconstruction algorithms based on the statistical model using statistical estimation techniques. The maximum likelihood (ML) and maximum a posterior (MAP) methods are two typical statistical methods. However, among other problems, these statistical algorithms are generally very computationally demanding. Another approach to reduce noise sensitivity is to filter measurement data before employing a deterministic model based reconstruction algorithm. It seems to provide a satisfactory result and is the current practice in clinical environment.

From the measurements obtained from the reconstructed images, tissue time activity curves (TTACs) are extracted from Regions-of-Interest (ROIs). These time activity curves in conjunction with an appropriate tracer kinetic model allow quantitative information about physiological processes to be extracted. Tracer kinetic model is a mathematical model which describes the dynamic behavior of the tracer in terms of mathematical representations. The known information on the behavior of the tracer or the system is incorporated by restricting the representation to a limited set of functions that are consistent with the known information. With the mathematical representation, the number of variables required to characterize the tracer kinetic is greatly reduced. In other words, tracer kinetic modeling can incorporate known information, such as a bio-chemical sequence, membranes that must be crossed, etc., about the tracer or the process to facilitate the extraction of useful physiological or bio-chemical information from the tracer kinetic measurements. Care must be taken, however, to ensure the correctness of the information incorporated in the models. Otherwise, erroneous interpretation will result from the use of the models.

1.2.5 Applications of cerebral PET

PET provides the investigators and the clinician the opportunity to examine quantitatively physiological functions as well as the anatomical distribution of

such activities. Studies in normal subjects allow for the non-invasive and three-dimensional investigation of functional "resting" states, in addition to sensory, motor, and behavioral responses to specific tasks. Such data are essential in defining the neuro-anatomical location and response characteristics of the normal brain. They serve as a necessary prelude to future studies of pathological states and patterns of recovery that functional brain systems undergo in their response to injury. Studies of brain pathology using these techniques have focused on the major clinical diagnostic problems of neurological disease. The general areas include cerebral vascular disease, damentia, seizure disorders, degenerative disease and neoplasm.

1.2.6 Limitations of PET

In spite of the fact that PET has a wide applicability in both medical and physiological diagnostic procedure, PET studies are still of limited uses due to a number of factors. First of all, the cost of a PET scanner is much expensive than the other imaging modalities. Such a high cost limits the widespread usage of PET scanner. In addition, positron-emitting radio-nuclides are usually of short half-lives, requiring an on-site generator (e.g., cyclotron). The expensive cost of cyclotron, although may be shared in case a number of PET center is set up, still significantly increases the capital cost associated with operating a PET center and hinders the usage of PET studies.

The second limitation is the total acquisition time for performing functional imaging with PET. It is of great importance, especially, for clinical studies. For example, dynamic Thalium-201 (Tl-201) SPECT studies in dogs have demonstrated the feasibility of estimating myocardial blood flow and volume of distribution [30]. However, acquisition times in these studies were up to 4 hours, which are impractical in daily clinical operation and also difficult for the patient to tolerate.

The third limitation is that one of the inherent components involved in performing dynamic PET studies is the tracer concentration in blood plasma, i.e. the plasma time activity curve (PTAC), which acts as the input function for the kinetic model. The tracer concentration in blood plasma are usually obtained by direct arterial blood sampling. This process is invasive, time-consuming and requires extra-staff. It introduces additional radiation exposure to clinical personnel and increases the possibility of spreading infectious diseases. Therefore, it is desirable to have methods which enable quantification of physiological processes with reduced number of blood samples so that the inconvenience caused can be minimized.

1.3 Present Works

In this thesis, we focused on performing functional imaging using emission computed tomography, including both PET and SPECT. Three techniques were presented in order to solve the aforementioned limitations. The overall aim of these studies is to reduce the inconvenience of performing functional imaging studies using emission computed tomography, hoping that such studies can be more commonly and extensively used in both academic and clinical environments.

1.3.1 Reduction of capital cost for dynamic functional imaging

Recently there has been interest in reducing the capital cost for performing dynamic functional imaging with the introduction of systems which acquire data over a limited angle, with rotation over time [31,32]. Also, coincidence studies have recently been performed using dual opposing detectors which are conventionally used for SPECT where the detectors rotate around the patient [33]. There is an increasing interest in deriving parametric images from these systems. In the case of SPECT there have been significant improvements in the quantitative accuracy of reconstruction as well as the development of multi-detector cameras which permit efficient detection. As a consequence, acquisition of kinetic data with associated modeling is possible on these systems and has

been demonstrated by a number of groups [34-37]. These systems have similar constraints to PET systems based on rotating detectors since, at any point in time, partial data are acquired. It is possible that the radio-pharmaceutical distribution changes during the acquisition of the set of projections necessary for reconstruction. The resulting images may contain artifacts which influence the accuracy of any subsequent parameter estimation [38-40]. Such artifacts may be alleviated by reducing the acquisition time for each image. However, the reduction of acquisition time is limited by the physical constraints of mechanical rotation, and by the limited counts acquired by a system whose acquisition geometry limits detection efficiency.

To avoid such kind of artifacts arisen in the reconstructed images and the subsequent parameter estimation error, Limber et al [41] and Zeng et al [42] have developed methods to recover the parameters of the time activity curve in each pixel directly from the projection data. They have shown that they can accurately recover time activity curves for a simple mono-exponential model. Extension to more complex models may be feasible, although the solution is likely to be computationally demanding.

Thus, in the first part of the thesis, we propose an approach for estimating the kinetic parameters from dynamic studies recorded by rotating detector systems. Such systems include single or multi-detector SPECT, coincidence detection systems and low-cost PET systems which involve detector rotation rather than a stationary ring of detector. The method involves interpolation across projections so as to provide an improved estimate of the projections for a stationary detector system. This interpolation process is applicable either to estimation of parameters directly from projections or to solutions involving conventional reconstruction prior to kinetic modeling. The interpolated projections are then reconstructed using the conventional filtered back-projection (FBP) algorithm and the kinetic parameters are estimated using a modified weighted least squares cost function. The proposed method is based on several previously validated

techniques which, in combination, provide a simple and computationally efficient solution.

1.3.2 The sampling requirement of performing dynamic studies

Dynamic studies and compartmental modeling are well established in PET. Most attention to the design of image frame sampling or recording schedule has thus been directed to PET image frame sampling schedules to increase the quantitative accuracy. Hawkins et al [43] studied the effects of temporal sampling on the glucose model using 18-fluoro-deoxy-D-glucose (FDG). Mazoyer et al [44] proposed a general method for estimating the precision of parameters resulting from the use of various experimental designs, including the rate of tomographic data collection. Delforge et al [45] applied an experimental design optimization framework and various criteria to the estimation of receptor-ligand reaction model parameters with dynamic PET data. Jovkar et al [46] addressed the general problem of finding an optimized scan schedule in PET dynamic studies which minimizes the parameter estimation errors. They found that there is a monotonic improvement in the index of parameter accuracy with increasing sampling frequency and concluded that a higher sampling frequency (more image samples), particularly in the early stage, should be used. The above conclusion was mainly due to using a cost function based on the assumption that sample points represent instantaneous activity concentration at the sample time, while in fact each sample point represents the integral of the changing activity concentration over the duration of the collection frame. Based on this fact, Li et al [47] proposed an optimum image sampling techniques using a modified cost function based on integrated activity concentration for PET modeling. They showed that by combining several adjacent image frames, the resulting smaller number of image frames can produce a comparable parameter estimation accuracy.

However, in these studies, little attention has been paid to systematically investigate the total scan duration which is usually decided empirically based on the following factors:

(1) the physical and physiological half life of the radio-tracer;

(2) the existence of blood metabolites;

(3) model consideration, (For example of ^{11}C acetate, the model is only validated for the initial 15 - 20 minutes);

(4) the clinical consideration to keep the scan as short as possible for the convenience of patients.

For dynamic SPECT, there are further limitations compared to PET. The lower sensitivity and the need for mechanical rotation of the detectors limit the shortest frame duration which can be reliably acquired. For clinical studies, the total acquisition time is also of great importance. For example, dynamic Tl-201 SPECT studies in dogs have demonstrated the feasibility of estimating myocardial blood flow and volume of distribution [30]. However, acquisition times in these studies are up to 4 hours, which are clinically impractical.

Therefore, the second part of the thesis is to systematically investigate the minimum required acquisition time for reliable parameter estimation, with Tl-201 dynamic SPECT as our typical example. In addition, the minimum number of frames and their duration were investigated using the optimum sampling schedule technique. The optimum sampling schedule can substantially reduce the total number of frames compared with a full dynamic study and reduce the need for a fast dynamic collection which is difficult to achieve on rotating SPECT cameras. The method for determining optimum sampling schedule and total acquisition time applied here to Tl-201 should also be applicable to other SPECT tracers.

1.3.3 Quantification of physiological processes for dynamic studies without the blood sampling procedure

Another limitation of performing functional imaging with PET is the requirement of the tracer concentration in blood plasma, i.e. PTAC, which acts as the input function for the kinetic model. The tracer concentration in blood plasma is usually obtained by direct arterial blood sampling which is considered to be invasive and time-consuming. It also exposes the clinical personnel to the danger of fatal blood infection and radiation. Therefore, it is desirable to have methods which enable quantification of physiological processes with reduced number of blood samples so that the inconvenience caused can be minimized.

In that light, Stefan et al [48] proposed using a population-based input functions, that were calibrated with two arterialized-venous blood samples, in the measurement of regional cerebral metabolic rate of glucose (rCMRGlu). Burger et al [49] has examined the possibility of mathematical metabolite correction. The mathematical metabolite correction was implemented by first approximating the input curve after its peak activity by a sum of three decaying exponentials. The amplitudes and characteristic half-times of which were then estimated together with the kinetic tissue parameters using a weighted least squares curve fitting routine. Both methods, however, assumed that certain parts of the PTAC are measured, i.e., the blood sampling procedure cannot be completely eliminated. Recently, Carson et al [50] and Watabe et al [51] have proposed techniques that completely eliminate the process of blood sampling. Both methods were developed for estimating the regional cerebral blood flow (rCBF) using PET. Extension of these two methods to more complex model is possible but may be computationally intensive.

Thus, in the last part of the thesis, we propose an approach to estimate the physiological parameters for a pre-assumed tracer kinetic model when performing dynamic PET studies, without taking arterial blood samples. The approach involves a denoising step for the projection data. In our case, we use a wavelet denoising approach. Wavelet denoising has the advantage of preserving

the structural information of the image when filtering the noise. The denoised projections are then reconstructed using FBP. From the reconstructed dynamic images, two TTACs are extracted from ROIs and are re-sampled using interpolation. Based on these two curves, a blind deconvolution technique is then applied to estimate the kinetic parameters.

1.4 Organization of the thesis

This thesis is organized into six chapters. Chapter 1 (this chapter) gives firstly a brief overview of the functional imaging. Particular attention is paid on performing functional imaging with PET. Its procedure and limitations are introduced. A summary of the proposed methods is also given. Chapter 2 presents some background materials on basic principles and quantification of PET and SPECT. Then the image reconstruction algorithm, tracer kinetic modeling, parameter estimation, input function acquisition and noise model are also described. In Chapter 3, a new approach for performing dynamic studies using rotating detector system is proposed. In Chapter 4, a systematic approach for investigating the minimum image acquisition time for performing dynamic studies is introduced. An alternative sampling schedule based on two sessions is suggested. In Chapter 5, a method for the quantification of dynamic studies without the requirement of input function is investigated. In these three chapters, the theory of the proposed methods, simulation studies and results are detailed. Finally, a summary of the work done is given in Chapter 6 of this thesis. Future extensions of the present work are also discussed.

Chapter 2 Preliminary

2.1 Introduction

In this chapter, we are going to review a number of subject areas which are fundamental for performing functional imaging with emission tomography. The aim of these sections is to provide the background materials to facilitate the discussion in other chapters.

To perform functional imaging with emission tomography, a radio-active tracer is usually introduced into the system under study. With different labeling of radio-nuclide, the studies can be classified either as Positron Emission Tomography (PET) or Single Photon Emission Computed Tomography (SPECT) studies. Since the physical decay is different for these two types of emission tomography, the quantification procedures of PET and SPECT are different. Therefore, in section 2.2, the basic physics and quantification of PET and SPECT are introduced.

The radio-active tracer will be delivered to and be extracted by the organ of interest, via the blood circulation system. The imaging system placed outside the subject can then continuously accumulate the photons emitted from the radio-nuclide based on a sampling protocol, which is a sequence of time intervals. A sequence of dynamic images, corresponding to the sequence of time intervals in the sampling schedule, are then reconstructed based on the accumulated counts from different angles. Different image reconstruction algorithms will have different characteristics and hence, give different performance. Thus, in section 2.3, we review two different types of image reconstruction algorithms which will be used in the subsequent chapters. Filtered back-projection (FBP) algorithm, which is developed assuming deterministic data, has been commonly used in x-ray tomography, and also, is the trivial choice for emission tomography. Another emerging imaging reconstruction algorithm is the order-subset expectation maximization (OSEM) algorithm which is based on statistical model. It has been

found that OS-EM can provide better performance for emission tomography and will become popularly used.

From the sequence of reconstructed images, quantitative temporal information about the changes of tracer concentration in a localized region is obtained. The measurements of the tracer concentration in tissue, or tissue time activity curves (TTACs), are always obtained from the reconstructed images either by drawing a regions of interest (ROIs) or by directly taking the values of individual pixels. The measurements of the tracer concentration in plasma, or plasma time activity curve (PTAC), can be obtained from peripheral blood sampling. These time activity curves in conjunction with an appropriate tracer kinetic model are then used to estimate regional bio-chemical or physiological parameters about the dynamic process using parameter identification techniques. This procedure requires effective integration of several areas, including tracer kinetic modeling, parameter estimation and input function acquisition. Therefore, in sections 2.4 to 2.6, we will briefly describe these subjects, respectively.

To carry out simulations for the proposed methods, appropriate addition of measurement noise in computer simulation is a necessary step in evaluating the effect of noise to the performance of the proposed methods in real situation. In this respect, a noise model is exploited to characterize the variance of the error in the measurements obtained from emission tomography. This noise model will be introduced in section 2.7.

2.2 Basic physics and quantification of Emission Tomography

2.2.1 Basic physics of PET

PET is a technique for measuring the concentrations of positron-emitting radio-isotopes within a three-dimensional object by using external measurements of the radiation from these isotopes. The location is sufficiently accurate to allow the data generally to be presented as a gray scale image of a cross-section of the object, with the intensity of each picture element or pixel proportional to the

isotopes concentration at that position of the object. Among the readily prepared positron-emitting radio-nuclides are isotopes of carbon, nitrogen, oxygen and fluorine. Since these elements are contained in essentially all the compounds that constitute or are consumed by the human body, PET is an obvious technique for the study of the fate of these compounds in vivo.

Proton-rich radioisotopes have two means of decay that will reduce excess positive charge on the nucleus: (1) the nucleus can capture an orbital electron and neutralize positive charge with the negative charge of the electron, or (2) a positive electron (a positron) can emit from the nucleus. The positron is an anti-electron that, after traveling a short distance, will combine with an electron from the surroundings and annihilate. On annihilation, the masses of both the electron and the positron are converted to electromagnetic radiation. In order to conserve energy and linear momentum, the electromagnetic radiation is in the form of two gamma rays of equal energy (511 keV), which are emitted 180° to each other (Figure 2-1). It is this annihilation radiation that can be detected externally and is used to measure both the quantity and the location of the positron emitter.

The external detection and localization of a positron emitter inside an object take advantage not only of the fact that the two annihilation photons are emitted 180° to each other, but also of the fact that they are created simultaneously. This phenomenon is called the annihilation coincidence detection (ACD), as we introduced in Section 1.2.2. Simultaneous or coincidence detection of two of these photons by detectors on opposite sides of an object places the site of the annihilation on or about a line connecting the centers of the two detectors (Figure 2-1). If the annihilation originates outside the volume between the two detectors, only one of the photons can be detected, and since the detection of a single photon does not satisfy the coincidence condition, the event is rejected.

Summing many such coincidence photons results in quantities that approximate line integrals through the radio-isotope distribution. For two-dimensional imaging, these line integrals form a discrete approximation of the Radon

transform of a cross-section of the radio-isotope concentration and can be inverted to form an image of the radio-isotope distribution.
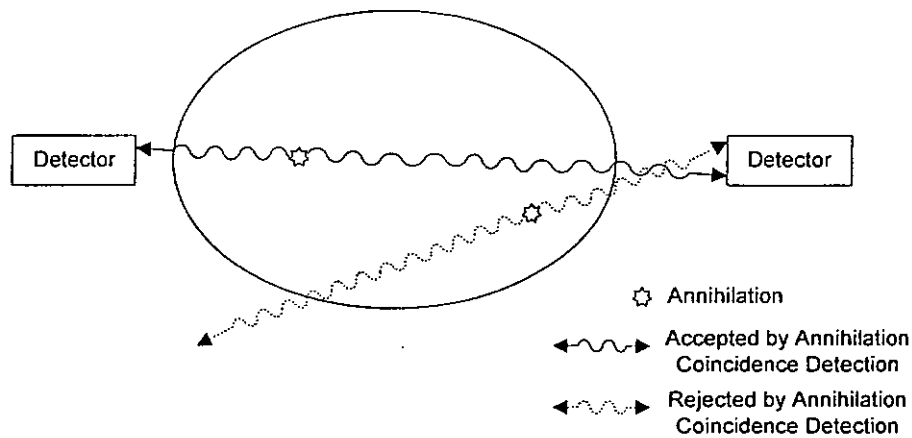
Figure 2-1 Principle of annihilation coincidence detection (ACD). When a proton-rich radio-isotope decays by means of emitting a positive electron (positron), the positron combines with a nearly electron and annihilate to produce two 511 keV gamma rays which are 180° to each other. If two gamma detectors are placed on opposite sides of an object containing the radio-isotope, the detection of two annihilation photons simultaneously, or in coincidence, places the original position of the annihilation along the line connecting the two detectors (solid line). Gamma rays from annihilation originates outsides the volume between the two detectors will only have one photon detected. Since the detection of a single photon does not satisfy the coincidence condition, the event is rejected (dash line).

2.2.2 Quantification of PET

Ideally, the only coincidence events recorded by a PET are those which arise from a unique positron annihilation that occurred along the line between two activated detectors. These are referred to as true coincidences and they carry useful information about the location of the positron emitter. However, other types of coincidence events, including accidental, scatter and multiple coincidences, occur and degrade the measurement. Besides, PET also suffers from the problems of attenuation, limitation of spatial resolution, partial volume

effect, resolution uniformity and resolution losses because of patient motion. Therefore, correction or compensation algorithms for these limitations have been an active area of research. A survey of these limitations and the corresponding correction algorithms can be found in [52].

2.2.3 Basic physic of SPECT

SPECT is a very similar procedure to PET. The only difference is that the decay of the particular radio-nuclides results in one or more independent photons instead of two annihilated photons. Individually emitted and thus spatially and temporally un-correlated radiation, such as gamma-rays associated with isomeric transition as well as x-rays associated with electron capture or internal conversion, form the basis of SPECT. Since the photons from each point inside the object under studied are emitted isotropically (equal numbers in all directions), collimation is needed to form a projection image. The collimator, usually made of lead, only allows x- or gamma-rays approaching the collimator from a nearly perpendicular direction to pass through (Figure 2-2). As a result, a projection image of the radio-nuclide distribution inside the object is formed. Each point in such projection images is simply the summation of the counts emitted along the projection through the body and approximates the line integral through the radio-isotope distribution. Therefore, as in PET, these line integral form a discrete approximation of the Radon transform of a cross-section of the radio-isotope concentration and can be inverted to form an image of the radio-isotope distribution.

2.2.4 Quantification of SPECT

Due to the use of lead collimator, the limited count statistics in most clinical studies affect the accuracy and precision of quantitative SPECT. With the advent of multi-detector technology which allows for efficient detections, SPECT has great potentials for the quantification of activity distribution in vivo. There are, however, several factors that must be considered in quantitative SPECT studies. Some of these factors are the system sensitivity and spatial resolution, dead-time

and pulse pile-up effects, the linear and angular sampling intervals of the projections, attenuation and scattering. Reviews of these limitations and correction algorithms can be found in [53].
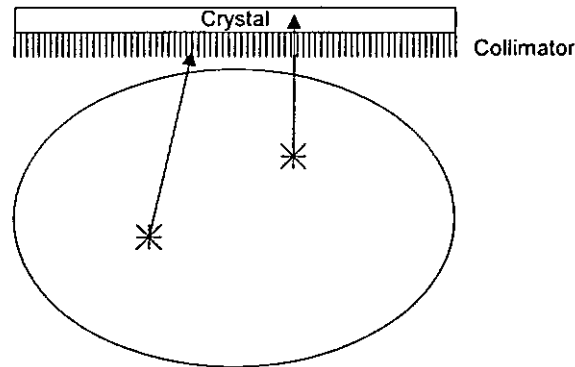
Figure 2-2 Collimation of a scintillation camera. The collimator forms the projection image by permitting x- or gamma-ray photons approach the camera from nearly perpendicular direction to reach the crystal while absorbing most of the other photons.

2.3 Image Reconstruction

The goal of image reconstruction is to recover the radio-tracer concentration from the measurements. Generally, image reconstruction algorithms are either based on Fourier or statistical methods. Fourier based algorithms are developed from a deterministic model, while statistically based ones rely on the Poisson model.

Fourier based algorithms are extremely fast, but suffer from artifacts and perform poorly when the number of observed coincidences is low. Low count scenarios are common and occur when radiation doses are low and/or scan times are short. Radiation doses are minimized for patient safety and scan times are kept short for patient comfort. Also, Fourier based algorithms do not account for the random nature of the PET data and fail to incorporate errors appropriately. In contrast, statistics based algorithms perform well in low count cases and have the ability to account for errors in the data. Unfortunately, they have the disadvantage of requiring computationally expensive iterative methods for

estimating the emission intensities. This high computational expense is the main reason that statistically based methods have not yet become popular in daily clinical operation or commercial medical imaging systems. Nonetheless, with the development of new fast algorithm as well as fast computing hardware, such statistical methods will be popularly used in the next generation of imaging systems.

2.3.1 Fourier based method

One of the most commonly used Fourier based reconstruction algorithms is the Filtered back-projection (FBP) method. The method was discovered by Bracewell [54] and independently by Ramachandran and Lakshminarayanan [55], who demonstrated that the object $f(x,y)$ is related to its projections, p, by a simple integral

$$f(x,y) = \int_0^\pi p_f(t,\theta)d\theta \tag{2.1}$$

where the function p_f is a "filtered" version of the projection acquired at angle θ, and the variables t is related to x, y, and θ by the formula

$$t = x\sin\theta + y\cos\theta \tag{2.2}$$

The filtered projection is best described in the frequency space. For a given angle θ, the Fourier Transform of p_f is the product of the Fourier Transform of the projection p and the function $|\omega|$:

$$p_f(\omega) = p(\omega)|\omega| \tag{2.3}$$

Thus, the FBP method consists of four steps (Figure 2-3):

1) Compute the one dimensional Fourier Transform of each projection.

2) Multiply the transform by the frequency filter.

3) Compute the inverse Fourier Transform, yielding p_f.

4) Back-project p_f.
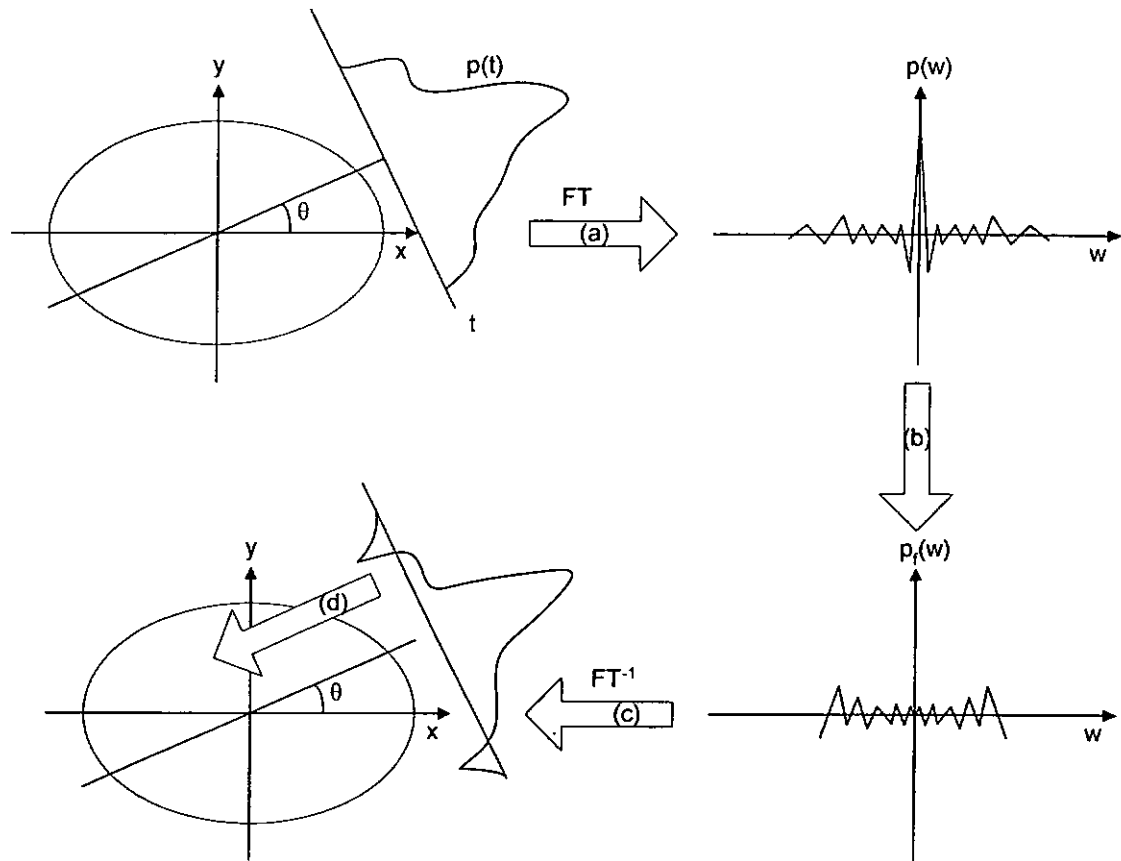
Figure 2-3 The basic steps of the FBP algorithm. (a) One-dimensional Fourier Transform of each projection. (b) Multiplication of the transformed projection by the ramp filter in frequency domain. (c) Inverse Fourier Transform of filtered projection. (d) Back-projection of filtered projection data.

The principal advantage of FBP is its simplicity and flexibility. Moreover, when using FBP, each projection can be processed as soon as it is measured. Therefore, the reconstructed image can be displayed shortly after the last view is completed.

In the above equation, the ramp filter, $|\omega|$, by itself will reconstruct the function exactly, but it will also enhance the high frequency components due to noise. To eliminate the noise, we could perform high frequency filtering as a separate step. Several commonly used filters include the Hamming filter, Parzen filter, Butterworth filter and Metz filter. [56]

2.3.2 Statistical based method

One of the statistical based image reconstruction algorithms is the expectation maximization (EM) approach. The EM approach was introduced to emission tomography by Rockmore and Macovski [57]. However, it is the development of a simple version of the algorithm by Shepp and Vardi [58] and independently by Lange and Carson [59] that made EM one of the most popular image reconstruction methods for emission tomography.

While the quality of the reconstructed image is good, the application of EM is computational intensive and has slow convergence rate, even with standard acceleration techniques [60]. Therefore, Hudson et al [61] proposed the order subsets expectation maximization (OS-EM) algorithm that sub-divides the available projections into ordered subsets and the standard EM algorithm is applied to each subset in turn. The resulting reconstruction becomes the starting estimate for the next subset. A single iteration through all the subsets involves an amount of computation equivalent to one iteration of conventional EM, yet yields a reconstruction similar to N iterations of conventional EM, where N is the number of subsets used. Thus, the procedure accelerates convergence by a factor proportional to the number of subsets.

More specifically, the OS-EM algorithm is summarized as follows:
Assume that the emitter activity is modeled as a Poisson point process. This activity is assumed to be uniform within the pixels of a grid imposed on the region. The expected number of photon emissions from pixel j is denoted by x_j. Define the image to be the vector $x = \{x_j: j=1,...,J\}$. The emitted photons are binned to provide counts y_t on detectors indexed by t. Also, weights a_{tj} is defined to represent the probability that an emission from pixel j is recorded at detector element t. Then, detector counts are Poisson distributed with expected values $\mu = Ey = Ax$, where A is the projection matrix.

Let $\hat{x}^0$ be a pre-specified starting image, e.g. uniform. Denote $\hat{x}^m$ the estimate of x after iteration m. Let $S_1, \ldots, S_n$ denote the chosen detector subsets in the order selected. The algorithm is then as follows:

(1) $m = 0$, $\hat{x}^m$ initialized to be positive

(2) Repeat until convergence of $\hat{x}^m$

   (a) $x^1 = \hat{x}^m$, $m = m + 1$

   (a) For subsets $i = 1, \ldots, n$

      Project: Calculate expected values for cumulated counts y as

$$\mu_t^i = \sum_{j=1}^{J} a_{tj} x_j^i \tag{2.4}$$

      for detector $t \in S_i$.

      Back-project: Calculate

$$x_j^{i+1} = x_j^i \frac{\displaystyle\sum_{t \in S_i} \frac{y_t a_{tj}}{\mu_t^i}}{\displaystyle\sum_{t \in S} a_{tj}} \tag{2.5}$$

      for pixel $j = i, \ldots, J$

(3) $\hat{x}^m = x^{n+1}$. $\tag{2.6}$

Further details of the OS-EM algorithm and the selection of order subsets can be found in [61].

Figure 2-4 shows the images reconstructed using the FBP and OSEM algorithms. In the figures, sinogram is firstly generated using the MCAT phantom (as shown in Figure 2-4a) and then reconstructed to give the cross-sectional image using the two algorithms (Figure 2-4c for FBP and 2-4d for OSEM). The effects of body attenuation is also demonstrated using the attenuation map shown in Figure 2-4b. The reconstructed images are shown in Figure 2-4g and 2-4h for FBP and OSEM, respectively. It should be noted that no attenuation correction is applied in both reconstruction. Also shown in Figure 2-4 are the profiles across the reconstructed images. In figures 2-4 e, f, i and j, the solid lines are the profiles for the original MCAT phantom. The dotted lines

are the profiles for the reconstructed images using either FBP or OSEM algorithms.
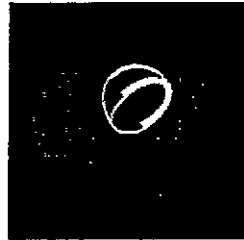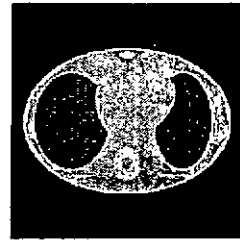
(a) MCAT Phantom   (b) Attenuation Map

(Without Attenuation)
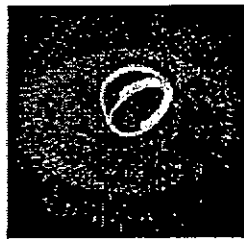
(c) FBP Reconstructed Image   (d) OSEM Reconstructed Image
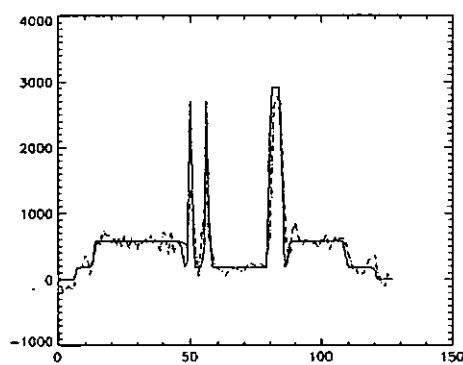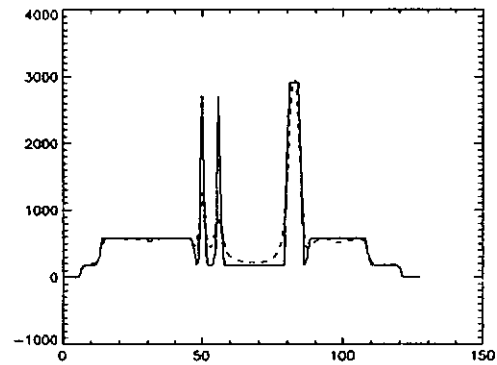
(e) FBP Profile   (f) OSEM Profile

Figure 2-4 A comparison of reconstructed images and profiles for FBP and OSEM algorithms.

(With Attenuation)

(g) FBP Reconstructed Image   (h) OSEM Reconstructed Image

(i) FBP Profile   (j) OSEM Profile
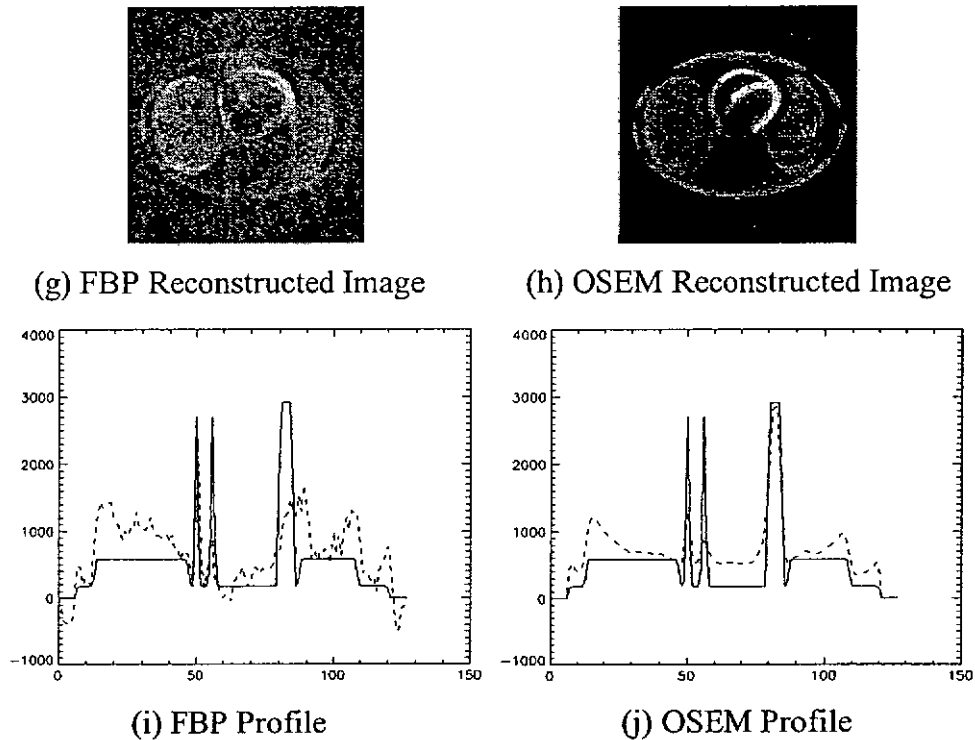
Figure 2-4 (cont.) A comparison of reconstructed images and profiles for FBP

and OSEM algorithms.

(a) The original MCAT phantom (Slice 71).

(a) The attenuation map (Slice 71).

(a) and (g) are the reconstructed images using FBP without and with

attenuation effects, respectively.

(a) and (h) are the reconstructed images using OSEM without and

with attenuation effects, respectively.

(a) and (i) are the profiles of the reconstructed images using FBP

without and with attenuation effects, respectively.

(a) and (j) are the profiles of the reconstructed images using OSEM

without and with attenuation effects, respectively.

In figures (e), (f), (i) and (j), the solid lines are the profiles for the

original MCAT phantom. The dotted lines are for the reconstructed

images using either FBP or OSEM algorithms.

Figure 2-4 demonstrated that both the FBP and OSEM algorithms provide

comparable performance when attenuation is not included (Figure 2-4e and 2-

4f). However, when the body attenuation is included, the FBP reconstructed image deviates significantly from the original image, while the OSEM reconstructed image can still provide satisfactory result.

2.4 Tracer Kinetic Modeling in Emission Tomography

Based on the sequence of images reconstructed from the accumulated counts at different time intervals, time functions can be extracted from either regions of interest or pixel by pixel. Such time functions show the dynamic of the tracer concentration in a local region. In conjunction with the tracer kinetic model and the input function, these time functions can be used to calculate the physiological parameters in a local region. (See Figure 2-5)

2.4.1 Basic assumption of tracer kinetic modeling

In tracer kinetic techniques, an appropriate tracer is required to follow the dynamic process of interest. There are several basic assumptions on applying tracer kinetic modeling:

1. Usually, a tracer must either be structurally related to the natural substance involved in the dynamic process (e.g. metabolic processes) or have similar transport properties (e.g. for flow systems). Furthermore, the tracer must be measurable and distinguished (in terms of measurements) from the natural substance that it intends to trace.

2. The tracer introduced is assumed to be in a trace amount, so that the process being measured is not perturbed by the introduction of the tracer. Otherwise, the measured results would reflect the effect of the tracer introduction and would not represent the process in its original state.

3. The dynamic process being evaluated with a tracer kinetic technique is usually assumed to be in a steady state. In other words, the rate of transport or reaction of the system is not changing with time, and the amount of substance in any part of the system is constant during the evaluation period. The steady-state condition is considered to be satisfied if the amount of change within the time of evaluation is small compared to the magnitude of

the process itself. For stable cyclic changes (e.g., pulsation of blood flow) with a cycle much shorter than the length of the measurement time, the method is still applicable, but the measurement will be the average value over the cycles.
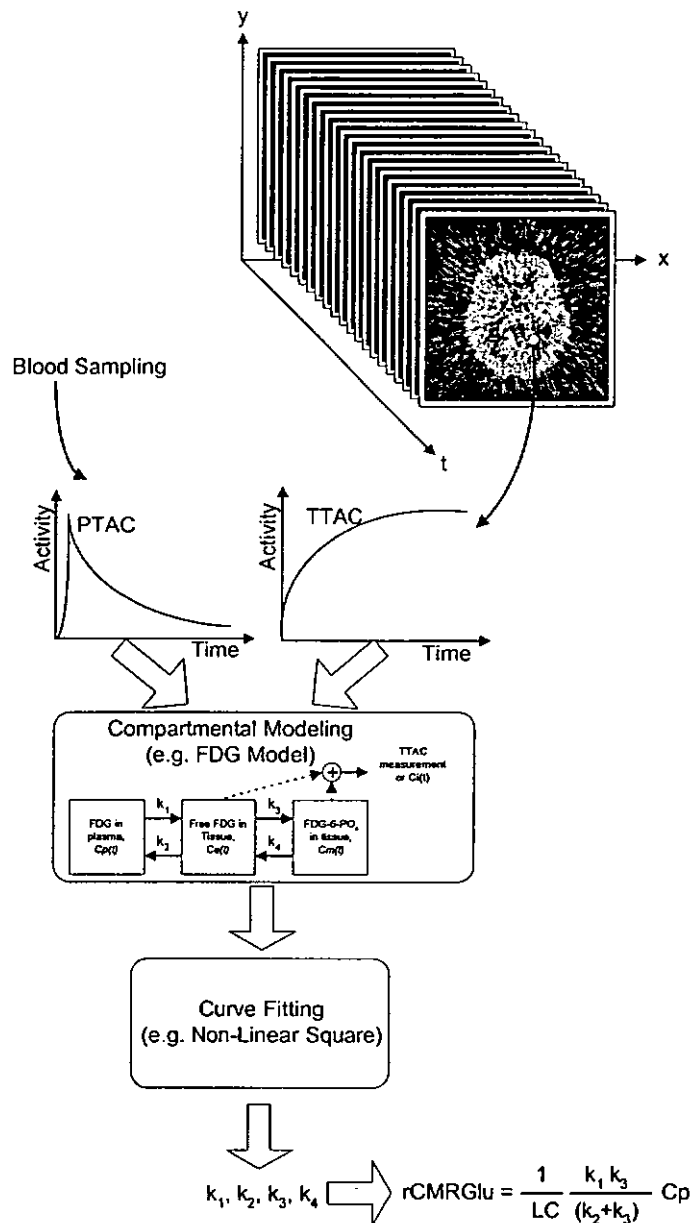
Figure 2-5 Steps involved in tracer kinetic modeling with PET. (i) Tracer activity in blood plasma is obtained by blood sampling. (ii) Tracer activity in tissue region is obtained from the sequence of reconstructed images. (iii) A compartmental model is assumed to incorporate known information about the process under study and to provide a framework to allow the interpretation of measurements. (iv) The rate constants for the compartmental model are estimated using parameter estimation technique, based on the measured PTAC, TTAC and the assumed compartmental model. (v) The estimated k_1-k_4 are used to calculate the physiological parameter in a local region.

2.4.2 Compartmental Models

Mathematical models are generally used to incorporate known information about a process to provide a framework or representation to allow the interpretation of measurements. For tracer kinetics, there exist various kinds of mathematical models of widely different mathematical characteristics: deterministic versus stochastic, distributed versus non-distributed, compartmental versus non-compartmental, and linear versus non-linear [62]. In biomedical applications, linear compartmental models are most frequently used.

A compartmental model (Figure 2-6) is usually represented by a number of compartments linked together by arrows indicating transport between compartments. A compartment is defined as a space in which the tracer is distributed uniformly. The amount of tracer leaving a compartment is assumed to be proportional to the total amount in the compartment. The arrows indicate the possible pathways the tracer can follow. The symbol k_i next to the arrow is called the rate constant, which has the unit of inverse time and the fraction of the total tracer that would leave the compartment per unit time.
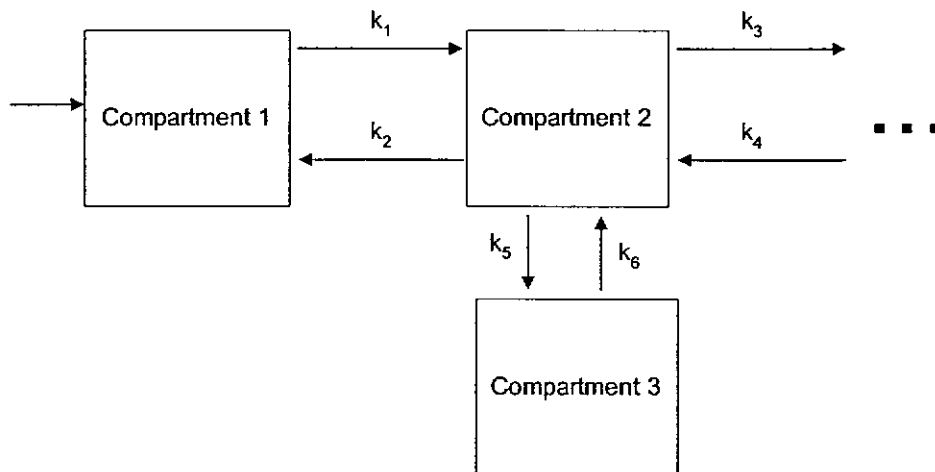
Figure 2-6 Compartment Modeling. Each square represents a compartment. Arrows represent possible pathways of the tracer. k_i (where i = 1, 2, ..., 6) represent the rate constants of the transport pathways.

There are a number of attractive properties of using compartmental model. First of all, it is conceptually simple, consistent with the way we commonly describe or think of the transfer of tracer in the tissue or in the body. In addition, based on the descriptions and definitions of the compartments, the tracer kinetics of a compartmental model can be described in terms of a set of linear, first-order, constant-coefficient, ordinary differential equations as long as the tracer is in small amount compared with its natural counterpart. Because of this linearity for the tracer, the kinetics of a physiological or biochemical process can be completely represented by a response function. The response function of a system will be exactly the tracer kinetic measurements from the system, if the tracer is delivered to the system as an impulse. For any other type of tracer delivery condition, the kinetic measurements will be simply the convolution of the delivery function (input function) and the response function of the system. In other words, if the input function (i.e. arterial blood or PTAC) and kinetic measurements in tissue are known, the response function of the system can be deduced by deconvolving the input function from the measured kinetics of the system. The response function so deduced would characterize the state of the system and provide the physiological or biomedical information desired. Furthermore, if certain conditions are satisfied [62], the response function of a compartmental model will consist of a sum of exponential functions [63]. The number of exponential components is usually equal to the number of compartments in the model [63]. Thus, by analyzing the response function in terms of exponential components, one can estimate the number of compartments required for constructing a model for the system.

2.4.3 Example: 3-compartment Fluoro-deoxy-glucose (FDG) model

Figure 2-7 shows the 3-compartment FDG model which is the mathematical model employed to determine the transport rate constants of radioactive FDG after it has been injected intravenously into the human body. This compartment model was proposed by Huang et al [64]. It was modified from the Sokoloff model [65] which was originally developed to measure the rates of glucose

utilization in the central nervous system in conscious rats by applying the [^{14}C]-deoxy-glucose (DG) radio tracer and quantitative autoradiography. The three compartments represents: (1) the concentration of FDG in plasma, $Cp(t)$, (2) the concentration of free FDG in tissue, $Ce(t)$, and (3) the concentration of FDG-6-PO$_4$ in tissue, $Cm(t)$, respectively. The four rate constants, k_1-k_4, in the model represent the tracer transport rates in this dynamic system. Parameters k_1 and k_2 represent forward and reverse transport rates of FDG across the capillary and their units are ml/gm/min and 1/min, respectively. Parameters k_3 and k_4 are the rate constants for phosphorylation of FDG and dephosphorylation of FDG-6-PO$_4$, respectively, and they have the unit of 1/min. Details of this FDG model were reported elsewhere [64,66]. Mathematically, the FDG kinetics obey the following first order system:

$$\frac{d}{dt}Ce(t) = k_1 Cp(t) - (k_2 + k_3)Ce(t) + k_4 Cm(t) \tag{2.7}$$

$$\frac{d}{dt}Cm(t) = k_3 Ce(t) - k_4 Cm(t) \tag{2.8}$$

The solutions to these differential equations are (see [64]):

$$Ce(t) = \frac{k_1}{\alpha_2 - \alpha_1}((k_4 - \alpha_1)e^{-\alpha_1 t} + (\alpha_2 - k_4)e^{-\alpha_2 t}) \otimes Cp(t) \tag{2.9}$$

$$Cm(t) = \frac{k_1 k_3}{\alpha_2 - \alpha_1}(e^{-\alpha_1 t} - e^{-\alpha_2 t}) \otimes Cp(t) \tag{2.10}$$

$$Ci(t) = \frac{k_1}{\alpha_2 - \alpha_1}((k_3 + k_4 - \alpha_1)e^{-\alpha_1 t} + (\alpha_2 - k_3 - k_4)e^{-\alpha_2 t}) \otimes Cp(t) \tag{2.11}$$

where $Ci(t)$ is the total ^{18}F activity in tissue, i.e. TTAC, the symbol $\otimes$ denotes the operation of convolution integral, and

$$\alpha_1 = (k_2 + k_3 + k_4 - \sqrt{(k_2 + k_3 + k_4)^2 - 4k_2 k_4})/2 \tag{2.12}$$

$$\alpha_2 = (k_2 + k_3 + k_4 + \sqrt{(k_2 + k_3 + k_4)^2 - 4k_2 k_4})/2 \tag{2.13}$$

Since $Ci(t)$, or equivalently TTAC, can be measured with PET scanner, and $Cp(t)$, equivalently PTAC can be obtained by taking blood samples, the values of the rate constants, k_1-k_4, of FDG model can be estimated by performing a non-linear least square optimization.

The estimated k_1-k_4, namely $\hat{k}_1 - \hat{k}_4$, are then used to calculate the metabolic rate of glucose in a local region, $rCMRGlu$, given as

$$rCMRGlu = \frac{1}{LC} \frac{\hat{k}_1 \hat{k}_3}{\hat{k}_2 + \hat{k}_3} Cp \qquad (2.14)$$

where LC denotes the lumped constant, accounting for the differences between FDG and glucose in transportation and phosphorylation, and Cp denotes the cold glucose concentration in plasma. Both LC and Cp are assumed constant and can be determined in advance. We are interested in the parameter $rCMRGlu$ because it represents the activity of a particular part of human body. This gives a useful information to medical practitioner in various diagnostic applications.
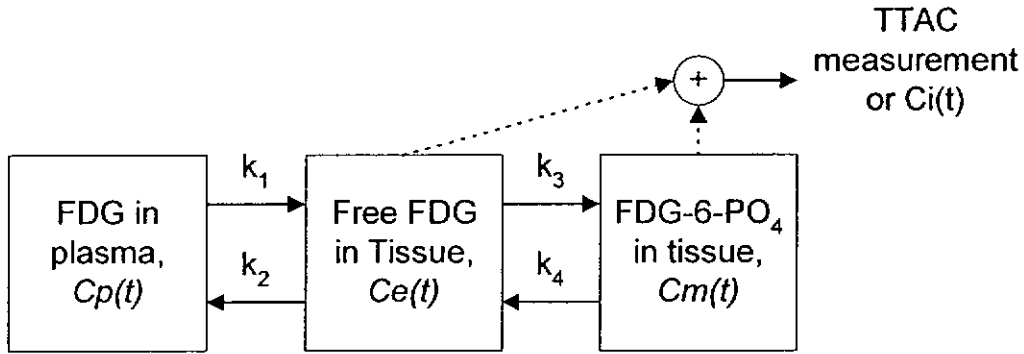
Figure 2-7 3-compartment FDG model. Left compartment represents vascular space for FDG. Center compartment represents tissue space for free FDG. Right compartment represents tissue space for FDG-6-phosphate. The activity measured by PET scanner is the summation of the activity from the center and right compartments, i.e. free FDG in tissue and FDG-6-phosphate in tissue.

2.5 Parameter Estimation in Emission Tomography

As it is stated previously, if the input function (i.e. arterial blood or PTAC) and kinetic measurements in tissue are known, the response function of the system can be deduced by deconvolving the input function from the measured kinetics of the system [67]. Unfortunately, most deconvolution routines have inherent computational difficulties with noisy data and are not easy to implement. The usual strategy is to use the known input as input to the model (numeric or analytic) representing the impulse response function and thereby fit this model predicted output to the actual measurements. In order words, the deconvolution

problem is converted to a curve fitting problem. One common example of these approaches is the Non-linear Least Square Approach (NLS).

2.5.1 Non-linear Least Square Approach (NLS)

With the FDG model described above as an example, the solution of the FDG model given in (2.11) can be expressed by the macro-parameters of the model as

$$Ci(t) = (B_1 e^{-L_1 t} + B_2 e^{-L_2 t}) \otimes Cp(t) \tag{2.15}$$

where

$$L_1 = (k_2 + k_3 + k_4 - \sqrt{(k_2 + k_3 + k_4)^2 - 4k_2 k_4})/2$$

$$L_2 = (k_2 + k_3 + k_4 + \sqrt{(k_2 + k_3 + k_4)^2 - 4k_2 k_4})/2$$

$$B_1 = \frac{k_1}{L_2 - L_1}(k_3 + k_4 - L_1)$$

$$B_2 = \frac{k_1}{L_2 - L_1}(L_2 - k_3 - k_4) \tag{2.16}$$

The resulting operational equation is non-linear with the macro-parameters, L_1, L_2, B_1 and B_2. When the NLS method is used, the macro-parameters are varied using certain optimization algorithm, such as the Newton-Gaussian or Levenberg-Marquardt algorithm [68,69] until the residual sum of squares (*RSS*) reaches its minimum. The *RSS* is defined as

$$RSS = \sum_{t=1}^{T} \left| Ci^{measured}(t) - (B_1 e^{-L_1 t} + B_2 e^{-L_2 t}) \otimes Cp(t) \right|^2 \tag{2.17}$$

where T is the number of samples of TTAC, $C_i^{measured}(t)$ is the measured sample which is usually taken as the average count-rate for the acquisition interval, and $(B_1 e^{-L_1 t} + B_2 e^{-L_2 t}) \otimes Cp(t)$ is the instantaneous model-predicted count-rate for the acquisition interval. The RSS denotes the residual differences between the measured tissue time activities, $Ci^{measured}(t)$, and the estimated tissue time activities. The curve fitting procedure is iterative. Once the macro-parameters have been estimated using this procedure, the corresponding micro-parameters of the model can be calculated as follows:

$$\hat{k}_1 = \hat{B}_1 + \hat{B}_2$$

$$\hat{k}_2 = \frac{\hat{B}_1 \hat{L}_1 + \hat{B}_2 \hat{L}_2}{\hat{B}_1 + \hat{B}_2}$$

$$\hat{k}_3 = \frac{\hat{B}_1 \hat{L}_2 + \hat{B}_2 \hat{L}_1}{\hat{B}_1 + \hat{B}_2} - \frac{\hat{L}_1 \hat{L}_2 (\hat{B}_1 + \hat{B}_2)}{\hat{B}_1 \hat{L}_1 + \hat{B}_2 \hat{L}_2}$$

$$\hat{k}_4 = \frac{\hat{L}_1 \hat{L}_2 (\hat{B}_1 + \hat{B}_2)}{\hat{B}_1 \hat{L}_1 + \hat{B}_2 \hat{L}_2} \tag{2.18}$$

where $\hat{L}_1$, $\hat{L}_2$, $\hat{B}_1$ and $\hat{B}_2$ are the estimated macro-parameters and $\hat{k}_1$-$\hat{k}_4$ are the estimated micro-parameters of the model. The estimates obtained using this method are expected to have optimal statistical accuracy in parameter estimation.

The above described method is the NLS. A weighted version of NLS performs similarly except that the RSS is modified as

$$RSS = \sum_{t=1}^{T} w_t \left| Ci^{measured}(t) - (B_1 e^{-L_1 t} + B_2 e^{-L_2 t}) \otimes Cp(t) \right|^2 \tag{2.19}$$

The weighting w_t reflects the relative accuracy of the measurements made at different times.

2.5.2 Other Approaches

In addition to NLS, there are a number of other approaches for parameter estimation include Autoradiographic Approach (ARA), Generalized Linear Least Squares Method (GLLS), Linear Least Squares Approach (LLS), Patlak Graphical Approach (PGA), Weighted Integration Method (WIM). An evaluation of these approaches, as well as NLS, is given in [70].

2.6 Input function Acquisition

In general, the amount of activity measured in an organ depends on the kinetics of the metabolic process, the transport properties between the blood and the site of the process in the cell, and the amount and time course of the delivery of the activity to the organ by the blood. Therefore, it is necessary to obtain independent measurements of the level of activity as a function of time in both

the tissue, with the imaging system, and the arterial blood, with well counter samples. The measurement of the arterial level of tracer as a function of time, or equivalently PTAC, acts as the input function for the tracer kinetic model. PTAC can be obtained in two different ways. The first one is obtained by taking blood samples throughout the studies. This procedure is considered to be invasive and the blood collection and processing process are both tedious and time consuming. Therefore, an alternative approach is to model the PTAC with an analytic function and calibrate the function with a few blood samples. Both methods will be described in the following.

2.6.1 Acquiring the Input function by taking blood samples

The usual method of obtaining the input function is to catheterize an artery of the subject and to take a series of blood samples following the injection of radio-tracer. The blood samples must be obtained with a frequency and over a length of time adequate to define the level of activity and shape of the input function. The frequency of sampling depends on the rate of injection and the rate of clearance of the activity from the blood. The length of time for sampling depends on the kinetics of the process being measured. The requirements of the sampling must be determined on an individual basis for each procedure. The weight or volume, as well as the activity, must also be determined for each blood sample.

Two methods have been developed to avoid arterial puncture in the measurement of input function. The first takes advantages of the fact that, when the temperature of the hand is raised, there is dilation of the blood vessels and the blood in the surface veins is effectively arterialized [71]. This produces a very high blood flow in the hand without an increase in metabolic function, and the extraction of the substrate in the hand is typically small. This method will probably be valid in those cases in which the rate of injection and rate of change of activity in the blood are relatively slow and the normal temperature extraction of the tracer in the tissue of the hand is relatively low. In practice, the hand is heated in a 43°C water bath and the blood samples are drawn from the vein of

the hand. The second method uses the PET system to measure the input function directly by measuring the amount of activity in the left ventricle, aorta, or other large artery as a function of time. This method requires that the system be capable of accumulating images rapidly enough to satisfy the temporal sampling requirements of the particular input function. This method is also limited to those cases in which the left ventricle or an adequately large artery intersects at least one image plane.

2.6.2 Input function Modeling

Another approach of acquiring the input function is to model the input function with an analytic function and calibrate the function with a few blood samples [48,72]. The tracer behavior in the blood circulatory system can be approximated by a compartment model, which contains four compartments or pools as shown in Figure 2-8. The first pool can be loosely considered as a pool consisting of the veins where the tracer is introduced; the second pool can be loosely considered as the arteries (plus the arterialized veins) where blood samples are taken for the measurements of tracer concentration; the third pool can be considered mainly as the tissue vascular and interstitial space. The tracer in Pool 3 is reversibly exchangeable with Pool 4 which consists of the cellular space of the tracer and its reversible products in tissue. In the tissue pool, the tracer may be excreted or sequestered. For simplicity, it is assumed that radio decay of the tracer has been corrected. A delay unit is introduced to simulate the delay due to the time required for the mixing of the tracer in the blood pool and for the tracer to be transported from the input pool to the measurement pool. For simplicity, this delay unit is assumed to be at the top of Pool 1. Based on this four-compartment model, a PTAC model can be mathematically expressed as

$$Cp^{\text{model}}(t) = \begin{cases} [A_1(t-\tau) - A_2 - A_3]e^{\lambda_1(t-\tau)} + A_2 e^{\lambda_2(t-\tau)} + A_3 e^{\lambda_3(t-\tau)} & t > \tau \\ 0 & t \leq \tau \end{cases} \quad (2.20)$$

where $Cp^{\text{model}}(t)$ is the tracer plasma concentration at time t; and A_1, A_2, A_3, λ_1, λ_2, λ_3 and τ are model parameters, with τ representing the time delay of the curve. Further details of this seven parameters PTAC model can be found in

[72]. This PTAC model has also been used in several previous simulation studies [73-75] and in the simulations of subsequent chapters to generate the PTAC.
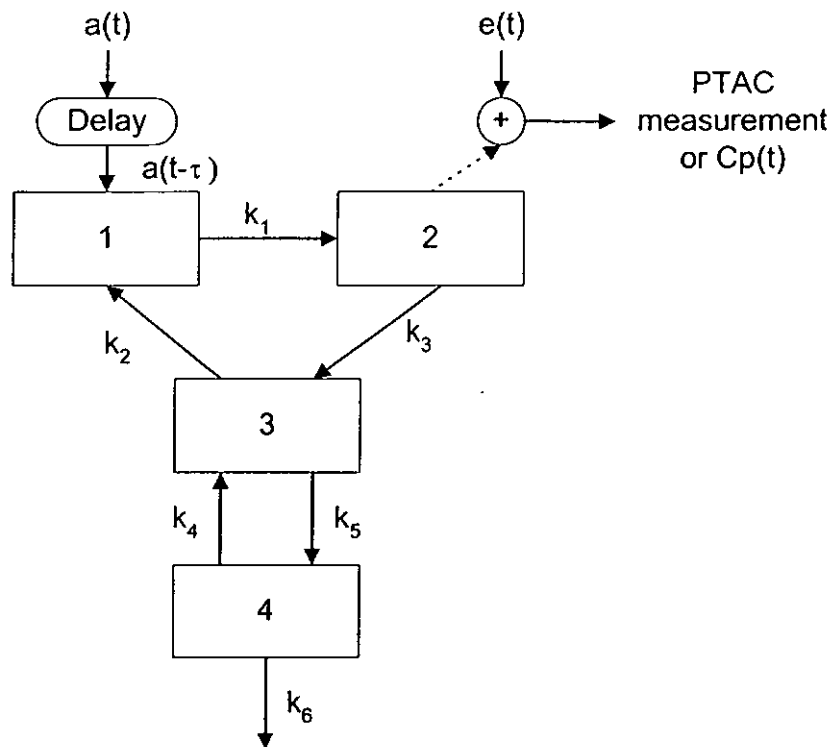
Figure 2-8 4-compartment model for input function modeling.

2.7 Noise Model

Since we perform computer simulations to validate our proposed methods, appropriately adding of measurement noise is necessary to simulate the actual environment and also to investigate the robustness of the proposed approaches. A noise model is exploited to characterize the variance of error in the measurements obtained from emission tomography.

As indicated before, the emission tomography imaging system accumulates the photons emitted from the radio-nuclide in a sequence of N scanning time intervals. Let $y(t)$ be the tracer concentrations to be sampled by an imaging system and N_k be the accumulated count (number of photons) over a certain time interval, then

$$N_k = \int_{t_{k-1}}^{t_k} y(t)dt + e_k \tag{2.21}$$

where the integral limit t_{k-1} and t_k are the end points of the interval and e_k is the noise in N_k. The variance of this count, denoted by $Var\{N_k\}$, is proportional to

$\int_{t_{k-1}}^{t_k} y(t)dt$, and mathematically it can be expressed as

$$Var\{N_k\} = Var\{e_k\} = c \times \int_{t_{k-1}}^{t_k} y(t)dt \qquad (2.22)$$

where c is a proportionality constant which determines the measurement noise level. In tracer kinetic modeling with emission tomography, it is a common practice that averaged count over the time interval, denoted by z_k, is used, that is

$$z_k = \frac{N_k}{\Delta t_k} = \frac{1}{\Delta t_k} \int_{t_{k-1}}^{t_k} y(t)dt + \frac{e_k}{\Delta t_k} \qquad (2.23)$$

where $\Delta t_k = t_k - t_{k-1}$ is the length of the time interval. The variance of z_k, therefore, can be derived as follows:

$$Var\{z_k\} = Var\{\frac{N_k}{\Delta t_k}\} = \frac{1}{(\Delta t_k)^2} Var\{N_k\} = \frac{c \times \int_{t_{k-1}}^{t_k} y(t)dt}{(\Delta t_k)^2} \qquad (2.24)$$

In tracer kinetic modeling with emission tomography, z_k is usually regarded as a measurement of y at mid-scan time equals to ($t_k + t_{k-1}$)/2.

The variance structures given in (2.22) and (2.24) will be used under different simulation environments. When the simulation noise is added directly to the projection data, which is usually taken as the accumulated counts over certain time interval, the variance structure in (2.22) is used. When the simulation noise is added to the TTAC, which is usually taken as the average measurement within a certain time interval, variance structure in (2.24) is used. In both cases, however, the variance structures given above only serve as a reasonable approximation to the variance of the PET measurement. It is equivalent to an experimental variance model [46], and it has been used in numerous studies [75,76,77]. More complicated variance structures for the PET measurement can be found in [78,79].

Chapter 3 Dynamic Imaging and Tracer Kinetic Modeling for Emission Tomography using Rotating Detectors

3.1 Introduction

As introduced in the previous chapters, emission tomography opened the possibility to record the bio-distribution of radio-pharmaceuticals within the body. Using emission tomography, it is possible to reconstruct a sequence of dynamic images which the pixel values represent the activity of regions of interest as a function of time. From these dynamic images, information relating to function of the living human body can be directly visualized. Furthermore, parametric images depicting physiological parameters, such as the metabolic rate of glucose in tissue, can be derived from these dynamic images using compartmental modeling [64]. A basic premise for extraction of quantitative parameters is that the time course of tracer in tissue can be reliably recorded. This can be achieved using stationary detectors as in the ring geometry most commonly available for positron emission tomography (PET) and similarly designed single photon emission computed tomography (SPECT) systems based on detector rings [80-82].

However, the ring geometry PET scanner or SPECT systems based on detector rings are not yet commonly available in clinical environment because of the high capital cost associated with such scanners. The high cost also hinders the developments of scientific research associated with PET studies. Therefore, alternative PET systems which acquire data using pairs of rotating detectors [31,32] have been developed. The total number of detectors in these systems is much lesser than their full ring equivalent which represents a significant reduction in cost. Also, coincidence studies using dual head SPECT scanner, with detectors rotating around the patient, have been performed recently [33]. Such system can provide the same performance achieved with present SPECT

scanners when operating as a SPECT system for imaging single photon emitters. It provides clearly superior performance to a 511 keV collimated SPECT scanner when operating in the coincidence mode. Deriving parametric images from these systems is becoming feasible. On the other side, recent advances in attenuation and scatter correction and multi-detector gamma cameras have significantly improved the quantitative accuracy of reconstruction for SPECT studies. As a consequence, acquisition of kinetic data with associated modeling is possible on these systems and has gained increased attention [34-37].

These systems, however, have similar constraints to PET systems based on rotating detectors which, at any point in time, only partial data are acquired. There is a possibility that the radio-pharmaceutical distribution changes during the acquisition of the set of projections necessary for reconstruction. Such redistribution will result in the acquisition of inconsistent projection data, leading to artifacts in the reconstructed image. Bok et al [83] investigated the problems of SPECT imaging in which tracer activity changed during acquisition and found that points of activity were smeared into ellipse that become more and more irregular as the duration of acquisition increases. Similar smearing effect were also reported by Links et al [39] on studying the effects of differential tracer washout during acquisition in a model of teboroxime clearance. Nakajima et al [84] found bands or "tails" of activity spreading across the field of view as activity changed substantially during the acquisition. These artifacts influence the accuracy of any subsequent parameter estimation [38-40].

One possible approach to reduce the artifacts in the reconstructed images is to sequentially acquire multiple short acquisition instead of one long acquisition. However, the reduction of acquisition time is limited by the physical constraints of mechanical rotation, and by the limited counts acquired by a system whose acquisition geometry limits detection efficiency. An alternative approach is to estimate physiological parameters of the process by using parametric images reconstructed directly from projections, rather than using a dynamic sequence of images. A general approach based on the weighted integration method was

proposed for SPECT [85] and was previously applied to PET data [86]. The third approach is to recover the parameters of the time-activity curve in each pixel directly from the projection data [41,42]. These approaches assume an explicit mono-exponential model for the time-activity distribution for each pixel in the images. They have shown that they can accurately recover the parameters of time-activity curves using simulated data. Extension to more complex models may be feasible, although the solution is likely to be computationally demanding.

In this chapter, we propose an approach for estimating the kinetic parameters from dynamic studies recorded by rotating detector systems. These systems include single or multi-detector SPECT, coincidence detection systems or low-cost PET systems which involve detector rotation. The method involves interpolation across projections to provide an improved estimate of the projections for a stationary detector system. The interpolated projections are reconstructed using the conventional filtered back projection (FBP) algorithm and the kinetic parameters are estimated using a modified weighted least squares cost function. The proposed method is based on several previously validated techniques which, in combination, provide a relatively simple and computationally efficient solution. To evaluate performance, we use the [^{18}F] labeled fluoro-deoxy-glucose (FDG) model, as introduced in Section 2.4.3, which has well documented kinetics and potential application in both PET and coincidence imaging.

3.2 Theory for the Proposed Method

3.2.1. A common nomenclature for PET and SPECT dynamics

To introduce the proposed approach it is useful to establish a nomenclature which is common to both PET and SPECT, specific to rotating detector systems as opposed to stationary systems. The usual mode of acquisition (typical of rotating camera SPECT systems) involves acquisition of projections at

individual angular positions with rotation of the detectors between subsequent

projection angles. It is useful to distinguish between the time taken to acquire a

single projection and the time taken to acquire all projections which constitute a

single rotation (or, more exactly, which would contribute to a single

reconstruction). A dynamic sequence consists of multiple rotations. We define

the following terms:

Frame-interval is the period of time for a complete rotation or acquisition of

one complete set of projections (contributing to a single reconstruction). For

example, a single head camera rotating over $360°$ between times t_0 and t_1 would

acquire all projections in the frame-interval $[t_1-t_0]$. We use this term with

reference to **frames** in the dynamic sequence as commonly used in nuclear

medicine. For a stationary detector all projections are normally acquired

simultaneously for the complete frame-interval. However, in a rotating detector

system, each individual projection occupies a **projection-interval** which, for a

single head camera equals [frame-interval / number of angles]. The data for

different projections will be acquired sequentially in each frame-interval. In the

general case, neither the frame-interval nor the projection-interval are constant

for sequential rotations. For any underlying tracer kinetics a time-activity curve

can be postulated for a single pixel in the projection domain. At a given angle the

acquisition over multiple rotations results in a set of measured samples of the

underlying time-activity curve, each sample occupying a projection-interval. We

refer to these as **projection-samples**. For a stationary detector, where the

projection-interval equals the frame-interval, the projection-sample is the total

counts acquired for the frame-interval, though normally considered as a sample

at the mid-point of the interval. In the case of the rotating detector the projection-

sample is the total counts for the projection-interval. However, the total counts

for the frame-interval can only be determined by interpolation between

projection-samples. We further define the selection of frame-intervals for the

complete multi-rotation study as **frame-sampling** to remove any ambiguity with

projection-sampling. Figure 3-1 illustrates the definition of frame-interval,

projection-interval and projection-sample.
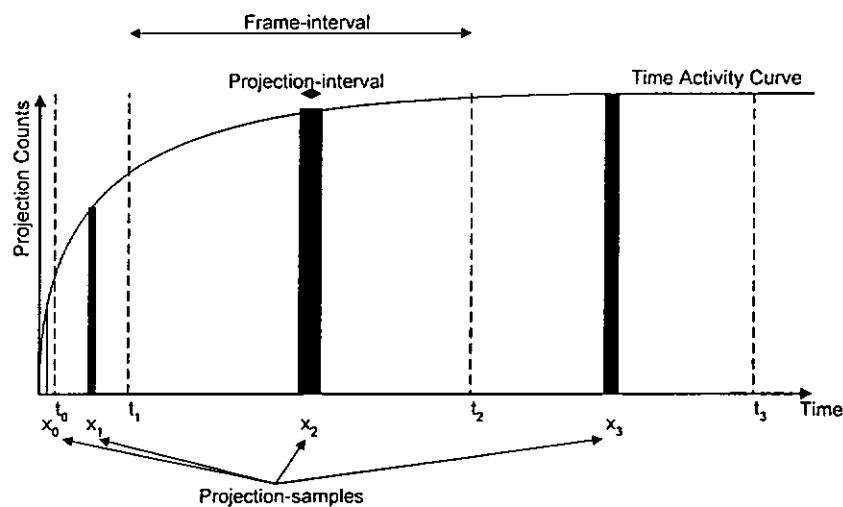
Figure 3-1 Definition of frame-interval, projection-interval and projection-sample. The solid curve simulates the actual tracer uptake curve. The solid black rectangles represent the projection samples which are taken as the count rates average over the projection-intervals centered at times x_i, where $i = 0,1,2,3$. The times t_i, where $i = 0,1,2,3$, define the boundaries between adjacent frames.

3.2.2 Basis of the method

To accurately estimate kinetic parameters from a dynamic study normally necessitates acquisition of multiple short frames, particularly near the start of the study. These short frames tend to be noisy and may occupy considerable memory space. If, instead, longer acquisition times are used, then there is likely to be tracer redistribution during early frame-intervals which may result in artifacts. Our proposed approach is to use the minimum number of frames, minimizing memory space and processing time. An interpolation technique is used to minimize the influence of tracer redistribution on the results. Fundamental to the approach is the adoption of a strategy where parameters are estimated based on the total counts over the frame-interval [44,87-91]. It is different from the traditional approach which uses the normal assumption that measurements represent estimates of the instantaneous mid-interval values. Using the modified premise, a more accurate interpolation scheme can be

defined in projection space [92] so that conventional reconstruction (e.g., using FBP) is feasible with reduced artifacts. The interpolation scheme adopted, unlike others, e.g., use of Simpson's rule [93], is not limited to acquisition with equal frame-intervals. Consideration of the optimal frame-sampling required for a specific model provides a solution with the minimum possible number of frame-samples, with different duration for each frame [94]. The suggested approach is practical, requiring a small number of rotations of the detector system, each rotation of different duration. The detailed steps and techniques are outlined below.

3.2.3 Estimation of projections by interpolation

The first step of the proposed approach is to estimate, as accurately as possible, the total counts in each pixel of the projection data for each frame-interval so that more reliable dynamic images can be reconstructed. The simplest technique to achieve this is by linear interpolation [95] as illustrated in Figure 3-2. For each pixel in the projection domain, we assume linear change of activity between projection-samples. We can then calculate the total counts within each frame-interval by summing the appropriate areas. We divide the total area by the corresponding frame-interval to obtain an average count-rate. It is recognized that this approach may be inaccurate for certain curve shapes (as illustrated). An alternative approach, based on the integration of overlapped parabolas, has therefore been developed [92]. The method is applicable to non-uniformly sampled measurements and can be efficiently computed.
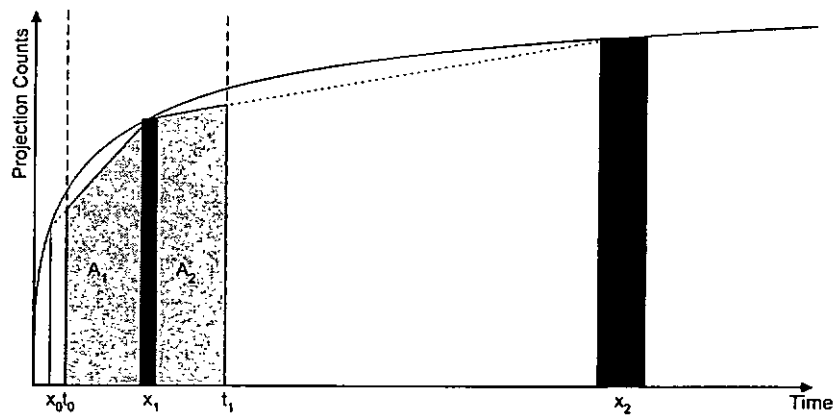
Figure 3-2 Linear Interpolation of projection data. For illustration purpose, this figure magnifies the early part of Figure 3-1. For linear interpolation, we use straight lines (dotted lines) to interconnect the measured projection-samples at x_i and approximate the area under the solid curve for the relevant frame-interval (say, $[t_0, t_1]$) by the area under the straight lines (i.e., $A_1 + A_2$).

The approach is illustrated in Figure 3-3. Our objective is to estimate the total counts between times t_i and t_{i+1}, with projection-samples for a given projection angle at times $x_1, x_2, ..., x_n$, where n is the number of frame-intervals. For the projection-sample at x_j located in the frame-interval between t_i and t_{i+1}, the total counts within the segment from t_i to x_j is calculated as the average integral of the two parabolas fitted to the projection samples at (x_{j-2}, x_{j-1}, x_j) and (x_{j-1}, x_j, x_{j+1}), respectively, between the limits t_i and x_j. The total counts within the segment from x_j to t_{i+1} is similarly calculated using the appropriate projection-samples. The total counts between times t_i and t_{i+1} are calculated as the summation of the integrals of these two segments. These total counts are then divided by the corresponding frame-interval to obtain an average count-rate for the frame-interval $[t_{i+1} - t_i]$. The above interpolation process is applied to every pixel of the projections. The resultant projection data, which better approximate the projections for a stationary detector system, can then be used to reconstruct the dynamic images using filtered back projection.
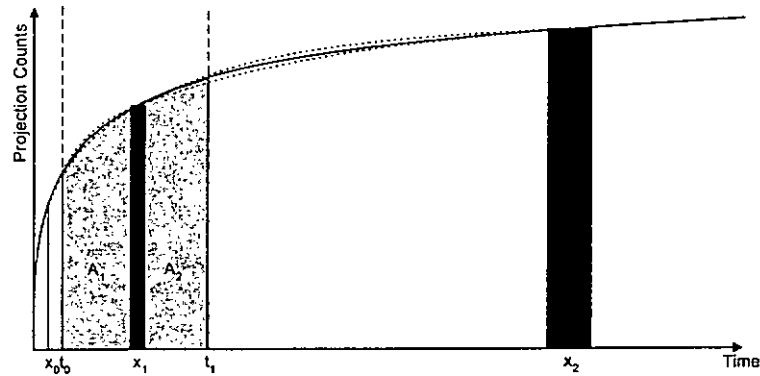
Figure 3-3 Interpolation of projection data using the overlapped parabolas method. This figure magnifies the early part of Figure 3-1. For overlapped parabolas, the area under the solid curve is estimated by averaging the area under two parabolas. For example, A_1 is the average of the area under the two parabolas, fitted with (origin,x_0,x_1) and (x_0,x_1,x_2), for the interval [x_1-t_0] and A_2 is the average of the area under the two parabolas, fitted with (x_0,x_1,x_2) and (x_1,x_2,x_3), for the interval [t_1-x_1] (x_3 is not shown in the figure.) Then, the total area under the solid line within [t_0,t_1] is approximated by A_1+A_2.

3.2.4 Tracer kinetic modeling

After we obtain dynamic set of reconstructed images, the next step is to perform physiological parameter estimation. Conventional modeling is based on the use of instantaneous curve values (as described in Section 2.5.1) whose estimation may include significant error since they are derived by taking the average over the frame-interval [87]. To reduce error, we make use of a modified approach which is based on the area under the curve [44,87-91]. This approach differs from the traditional technique in that a modified weighted least squares cost function or residual sum of squares (RSS) is adopted. Traditionally, RSS is defined as in Equation 2.17 (or Equation 2.19) and is given in the following:

$$RSS = \sum_{t=1}^{T} w_t \left| Ci^{measured}(t) - (B_1 e^{-L_1 t} + B_2 e^{-L_2 t}) \otimes Cp(t) \right|^2 \tag{3.1}$$

where T is the number of samples, w_i is a weighting factor, $C_i^{measured}(t)$ is the measured sample which is usually assumed to be the average count-rate for the frame-interval, and $(B_1 e^{-L_1 t} + B_2 e^{-L_2 t}) \otimes Cp(t)$ is the instantaneous model-predicted count-rate for the frame-interval. The problem for such RSS is that, when the dynamics change rapidly, the duration of acquisition must be sufficiently small, otherwise $C_i^{measured}(t)$ may not be a good approximation of the instantaneous measurement at t. In other words, we typically need a large number of frame-samples when the activity changes rapidly. To avoid this requirement, the RSS is modified to be

$$RSS = \sum_{i=1}^{T} w_i \left| Ci^{measured}(t) - \frac{1}{\Delta t_i} \int_{\Delta t_i} (B_1 e^{-L_1 t} + B_2 e^{-L_2 t}) \otimes Cp(t)dt \right|^2 \qquad (3.2)$$

where $\dfrac{1}{\Delta t_i} \displaystyle\int_{\Delta t_i} (B_1 e^{-L_1 t} + B_2 e^{-L_2 t}) \otimes Cp(t)dt$ is the average count-rate over the

frame-interval Δt_i. In this case approximation error can be reduced. It has been shown [94] that, by using the above modified fitting algorithm, only four dynamic images are necessary to estimate the metabolic rate of glucose using the four-parameter FDG model. In this case Δt_i may be relatively large.

3.3 Simulation Method

As indicated earlier we have chosen to validate the proposed method using the FDG model [64], as introduced in Section 2.4.3. The input function for the model, i.e. the FDG concentration measured in blood plasma, was generated numerically using the input function model introduced in Section 2.6.1, a commonly adopted approach [96-98]. We assume that the time delay of the input function model is equal to zero. The mathematical expression of this simplified input function model, $Cp^{model}(t)$, is given as follows:

$$Cp^{model}(t) = \begin{cases} (A_1 t - A_2 - A_3)e^{\lambda_1 t} + A_2 e^{\lambda_2 t} + A_3 e^{\lambda_3 t} & t > \tau \\ 0 & t \leq \tau \end{cases} \qquad (3.3)$$

where, as previously published [72]:

$$A_1 = 851.1, A_2 = 21.88, A_3 = 20.81 \qquad [\mu Ci/ml]$$

$$\lambda_1 = -4.134, \lambda_2 = -0.1191, \lambda_3 = -0.0104 \qquad [1/\text{min}]$$

The proposed method was tested using the phantom shown in Figure 3-4 which contains three regions with different kinetics. Activities in the left ellipse, right ellipse and the circle were simulated to represent the kinetics which are typical of brain white matter (Region 1), grey matter (Region 2) and an intermediate value (Region 3). The resulting tracer time-activity curves are shown at the top right, middle right and bottom right, respectively. The outer largest ellipse has constant activity. The transport rate constants, k_1-k_4, for the three regions were obtained from [64] and are listed in Table 3-1 below:

	k_1	k_2	k_3	k_4	K
Right ellipse	0.1020	0.1300	0.0620	0.0068	0.0329
Left ellipse	0.0540	0.1090	0.0450	0.0058	0.0157
Circle	0.0780	0.1195	0.0535	0.0063	0.0241

Table 3-1 The transport rate constants, k_1-k_4, for the three regions. The derived parameter, K, which equals $k_1 * k_3/(k_2 + k_3)$ and is proportional to the metabolic rate for glucose, is also shown.
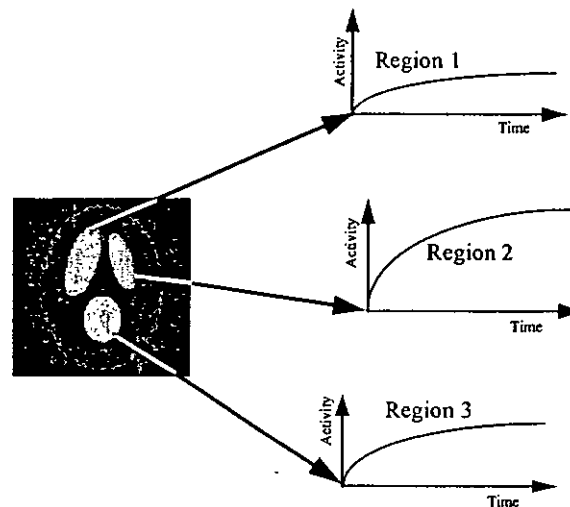
Figure 3-4 Simulated phantom. The activity in the left ellipse (Region 1), right ellipse (Region 2) and the circle (Region 3) simulate the tracer kinetics of brain white matter, grey matter and an intermediate value. The tracer time activity curves are shown at the top right, middle right and bottom right, respectively.

For simplicity, $K = k_1*k_3/(k_2+k_3)$, which is proportional to the metabolic rate for glucose, is used as our final estimation result to compare the performance for different methods.

As indicated earlier, it has previously been demonstrated that the FDG kinetics can adequately be estimated by acquiring four frame-samples. According to [94], the four frames are of different duration and they are, in minutes, [0,2.7], [2.7,15.7], [15.7,77.1], [77.1,120]. For each of these frame-intervals, 32 projections, each with 64 bins, were simulated, assuming 180° rotation.

Activity was simulated as the total counts detected over the complete frame-intervals as in conventional PET using a ring of detectors (Type A) and the counts correspond to the projection-interval for a specific projection, assuming rotation of the detector (Type B). The simulation did not include attenuation, scatter or distance dependent detector response.

The projection data were scaled to count densities which might be expected for multi-detector SPECT (with 0.02k to 0.05k counts/sec in the last frame-interval), coincidence imaging (with 0.1 to 0.2k counts/sec in the last frame-interval), and PET (with 1k to 2k counts/sec in the last frame-interval). Poisson noise was added to the projection data (See Section 2.7).

Four methods for analysis were compared. The data acquired with full ring geometry (Type A above) were reconstructed using FBP, and kinetic modeling was performed on the reconstructed images using the modified RSS described in Section 3.2 (Method 1). This method has fully recorded projection data for each frame-interval. For the data acquired with a rotating detector (Type B above), the data were reconstructed and analyzed without interpolation (Method 2). For this Type B data set, curve integrals on projections were also determined using interpolation (linear versus overlapped parabolas), prior to FBP reconstruction and modeling with the modified RSS approach (Methods 3 and 4). In the case of overlapped parabolas, projection data were normalized to account for systematic

errors in the interpolation. To determine the appropriate normalization factors, true time-activity curves for a full ring detector system were simulated for the range of expected model parameters (typical of grey to white matter). The integrated counts for each frame-interval were compared to the integral estimated from the projection-samples which would be obtained from a rotating detector. The ratio of these integrals was used to normalize the projections. Figure 3-5 shows the normalization ratio calculated at different angles. The dashed line, dotted line and the solid line represent ratios for grey matter, white matter and the intermediate value respectively. The systematic error was found to be reasonably independent of the underlying kinetic parameters and therefore normalization was based on the values obtained using the intermediate set of kinetic parameters (as per the third row of Table 3-1).
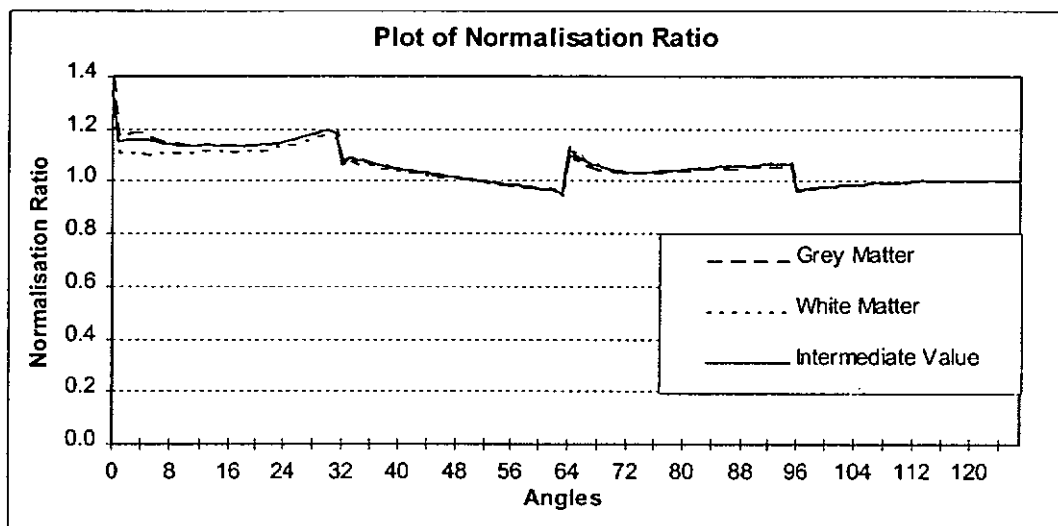
Figure 3-5 The normalization ratio at different angles. The dashed line, dotted line and the solid line are the ratio for grey matter, white matter and an intermediate value.

K, which is proportional to the metabolic rate for glucose, was estimated for the four different methods at different simulated count densities. For each count density, the simulations were carried out for one hundred independent trials to obtain average performances for each method. The percentage errors in K compared to the true parameters and the coefficient of variation (CV) of the estimated K's were determined

3.4 Simulation Results

Figure 3-6 illustrates the first reconstructed frame of the simulated dynamic study for the four methods: (i) ring detectors, (ii) rotating detectors with no interpolation, (iii) linear interpolation and (iv) interpolation using overlapped parabolas. These images are noise-free to better illustrate the artifacts present when activity changes rapidly. Both linear interpolation and interpolation based on overlapped parabolas provide qualitatively improved reconstruction. The curves in Figure 3-7 represent selected profiles through the same images as illustrated. For the left column of Figure 3-7 the lower peak of the curves represents the tracer activity in the left ellipse which has kinetic parameters simulating brain white matter. For the right column of Figure 3-7 the highest peak represents the tracer activity of the right ellipse which simulates brain grey matter. For all six figures, the solid line represents data simulated for full ring detectors. The dotted line represents the data using a rotating detector: (a) and (b) with no interpolation, (c) and (d) using linear interpolation, and (e) and (f) using overlapped parabolas for interpolation. As can be seen, the use of overlapped parabolas for interpolation provides significant improvement compared to linear interpolation, resulting in close agreement with the result obtained for a ring detector system.

(i)   (ii)   (iii)   (iv)
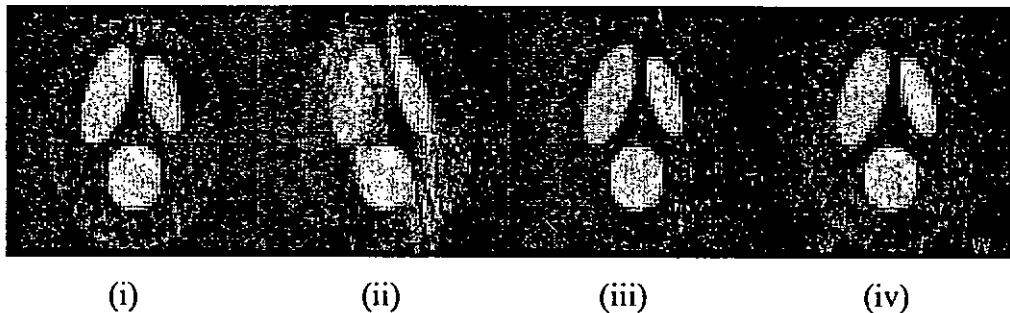
Figure 3-6 Reconstructed images for the first frame-interval using the four different methods: (i) ring detectors, (ii) rotating detectors without interpolation, (iii) rotating detectors with linear interpolation and (iv) rotating detectors with interpolation using overlapped parabolas. These images are noise free to better illustrate the artifacts present when activity changes rapidly.
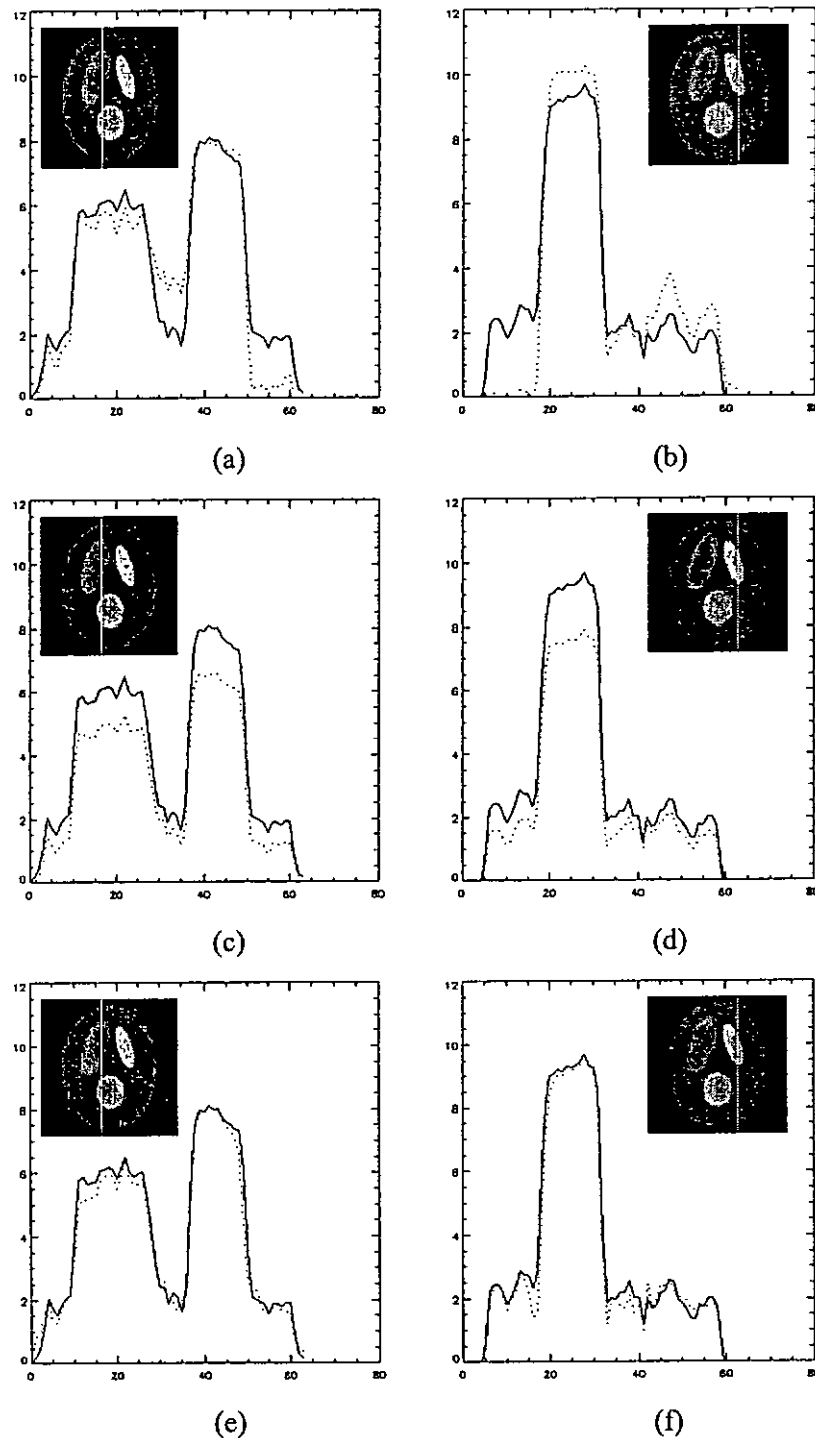
Figure 3-7 Selected profiles through the images reconstructed using rotating detectors with different interpolation methods. The solid lines in all figures are from the data simulated for ring detectors. The dotted lines represent the profiles through the image reconstructed using rotating detectors with different methods: (a) and (b) without interpolation, (c) and (d) linear interpolation, and (e) and (f) interpolation based on overlapped parabolas. The lower and higher peaks of the curves on the left column simulate the tracer activity of Region 1 and Region 3, respectively. The highest peak on the right column simulates the tracer activity of the Region 2. These images correspond to noise free data.

Based on the dynamic images reconstructed using the four different methods, the modified modeling technique was used for parameter estimation. The results for estimation of metabolic rate of glucose (K) are illustrated in Figure 3-8a and 3-8b where the percentage error and CV for K are displayed graphically. As expected, the use of rotating detectors can introduce error to parameter estimates. Although linear interpolation provides lower CV, there is significant percentage error in the parameter estimates for all three regions in the phantom. The proposed interpolation method based on overlapped parabolas provides similarly low percentage error to the results obtained with a ring detector system although the CV is higher than that obtained using linear interpolation.
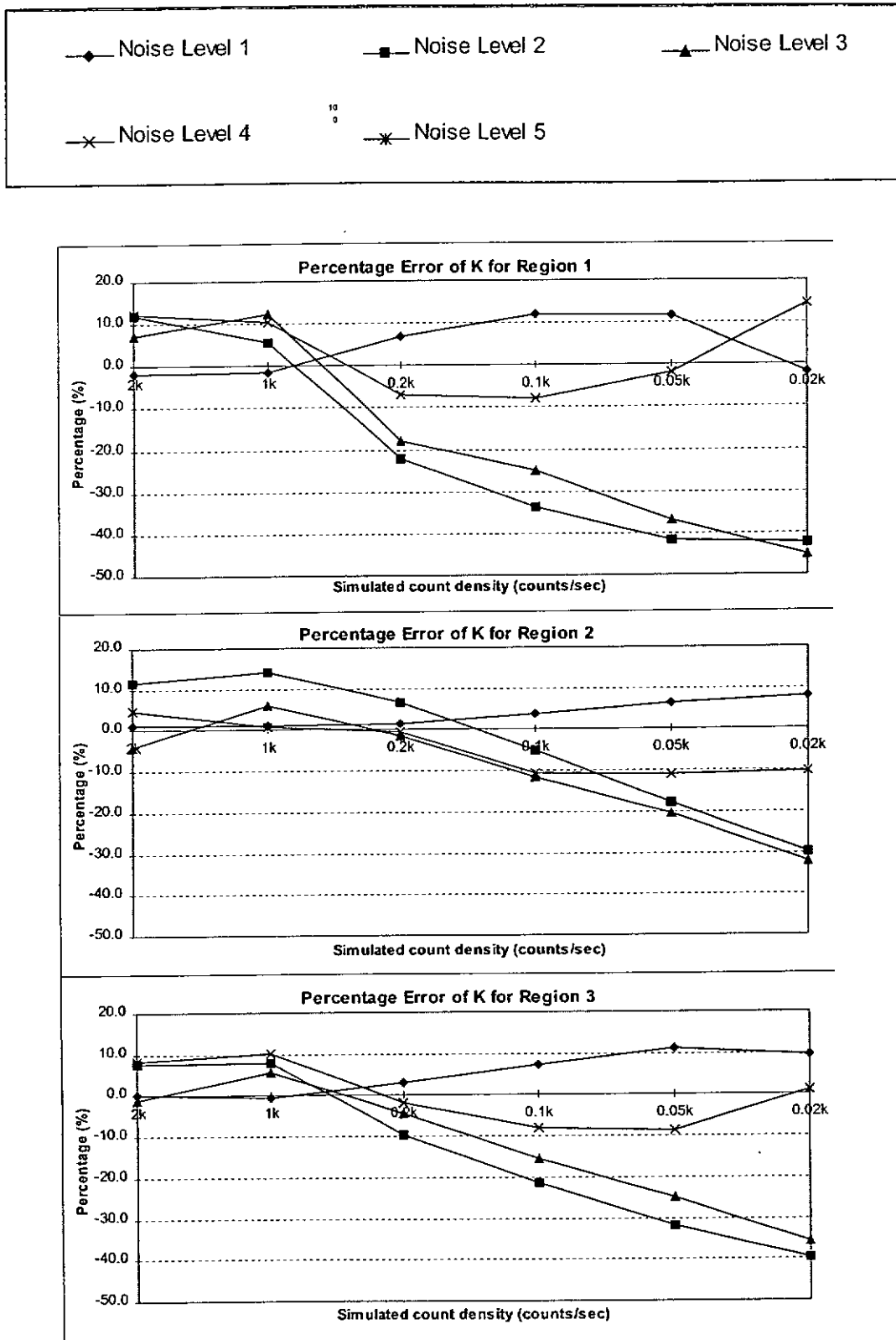
Figure 3-8a Percentage error of estimated K for the three regions.
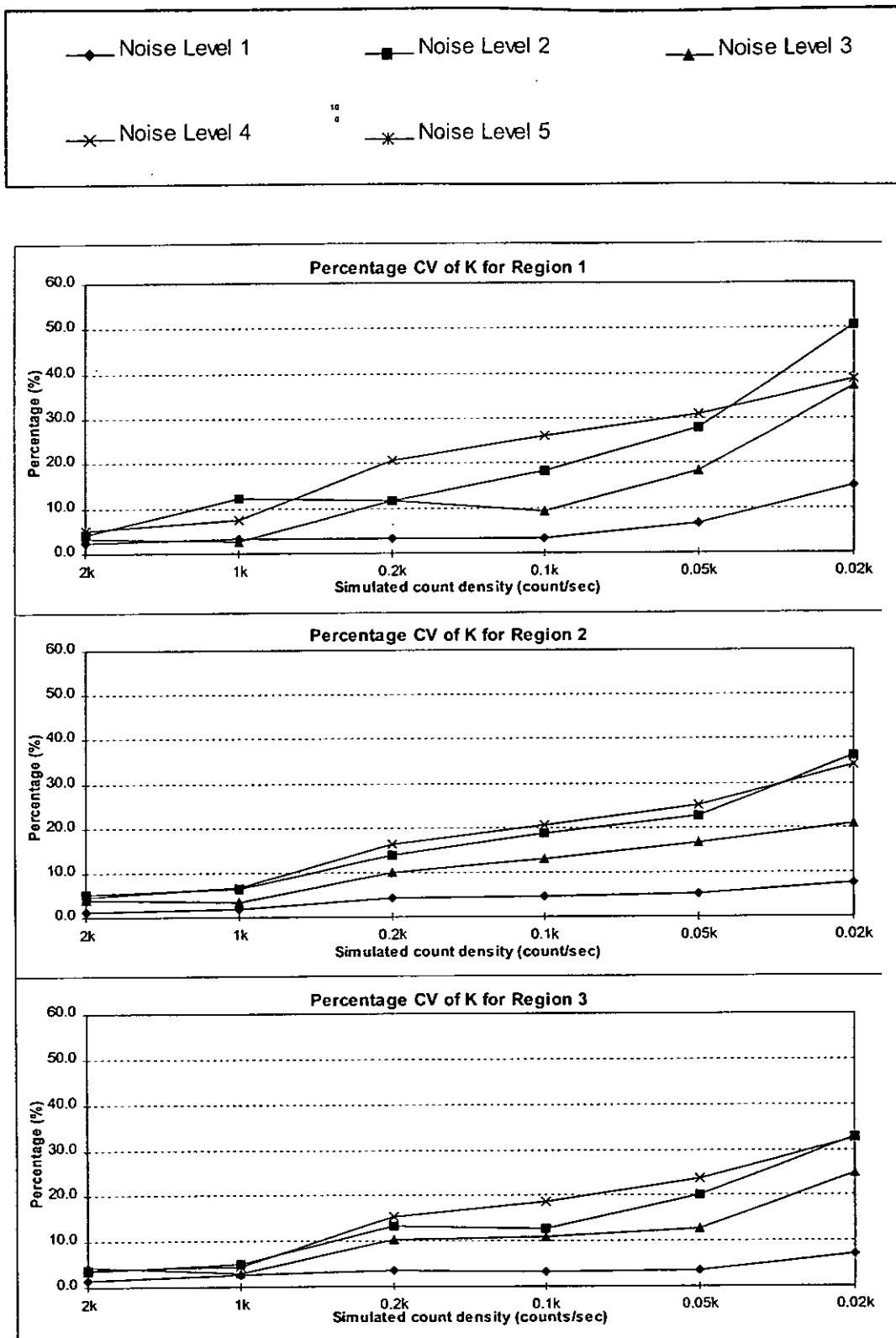
Figure 3-8b Coefficient of variation (CV) of estimated K for the three regions.

3.5 Discussion

There is increasing interest in analysis of kinetic data since the range of potentially useful tracers is expanding and suitable detection systems are becoming more affordable. However the accurate estimation of tracer kinetic parameters from low-cost tomographic systems, which typically do not have a full ring of detectors, is not straight-forward. Several groups have suggested approaches for determining kinetic parameters directly from projections to overcome the problems associated with rapidly changing activity. These approaches can provide unbiased parameter estimates for simple models but their general applicability has yet to be demonstrated. The approach suggested here is intrinsically simple, based mainly on the integrals of counts during the time course of a tracer rather than the instantaneous values. This provides the basis for the interpolation method for which the total counts in the frame-interval is directly estimated. It also gives rise to a modified parameter fitting algorithm and a frame-sampling scheme which would appear to be favorable for the situation where rotating detector systems are used. The proposed techniques are not computation intensive compared with methods where modeling is performed directly from projections. They therefore have appeal for general clinical applications. Using the proposed method, artifact-free dynamic images, which reflect the bio-distribution of radio-pharmaceuticals within the body, are available. Detailed comparison of the proposed methods with alternative techniques will be the subject of future investigation and has not been included in this thesis.

The simulation results presented here are intended to be illustrative rather than conclusive. FDG has been chosen, given the interest in its application on low cost coincidence detection systems or rotating PET systems. The geometry of detection simulated is intended to illustrate the worst-case situation rather than to exactly simulate the detection geometry of a particular PET or SPECT system. Indeed the detection geometry more closely resembles a rotating SPECT system, for which the proposed methods have relevance. This chapter does not address

other physical constraints on the accuracy of measurement such as attenuation, scatter or, in the case of PET, random coincidences. Simplifications in the overall simulation were considered necessary to isolate the influences which were the primary concern in this study (i.e., possibility of tracer movement in a single rotation). The input function can be accurately measured in patients based on counting of arterial blood samples (although less invasive methods are desirable). We did not examine the influence of input function shape on the results of this study, however we do not anticipate that the input function would be a dominant factor, as, in general, relatively small differences in input function shape occur between individuals for a given tracer.

The method of interpolation used in the proposed approach has several appealing properties compared to some other interpolation schemes. Firstly it provides a valid integral rather than a simple point value. As has been stated above, this has direct relevance to the proposed methods as it facilitates the use of optimized frame-sampling to reduce the number of detector rotations. The technique does not rely on having equally spaced frame-samples but is generally applicable for any sampling scheme. This study does not address the question of how this technique compares with other non-linear approaches to interpolation. It also does not explore the limits of the technique's application. However it is well demonstrated that, for the case of FDG, which is widely used in clinical practice, the technique provides results which are similar to those obtained for a stationary ring detector.

One problem with the interpolation method is the difficulty in handling points near the start of the study. The reason for this is that two of the three points used for fitting the parabola are very close together (the first point at time 0). As a result the best-fit parabola can deviate significantly from the true curve. Our results (Figure 3-5) demonstrate that the problem is small except for a small number of projections. There are alternative approaches to solve this problem (e.g., constraint in the turning value of the parabola could be applied). However in the proposed approach we have chosen to adopt a normalization method

which applies a correction based on the range of errors which could be anticipated for the family of possible kinetic curves. This method provides a practical solution with good results. Further work would be necessary to compare alternative strategies.

The simulation uses a frame-sampling scheme which particularly favors relatively low efficiency detection such as in SPECT. It has been demonstrated that the choice of four frame-samples is sufficient for accurate determination of the kinetic parameters for FDG. The use of four frame-samples has appeal since this minimizes the data storage requirements as well as minimizing the time required for reconstruction.

Parameter estimates for data acquired using a rotating detector were very close to those obtained using a stationary ring detector. However the coefficient of variation for parameter estimates was larger. It is clear that interpolation, based on noisy projection-samples, introduces an uncertainty in the derived frame-sample counts used to determine the parameter estimates. This results in an increased CV, particularly in the case of low count density.

3.6 Summary

In this chapter, we proposed a novel approach for reconstruction of dynamic images and determination of tracer kinetic parameters using data acquired from a rotating detector system. The method involves the use of an interpolation method which provides an improved estimate of the total counts within each frame-interval, together with application of an integral-based model-fitting algorithm. The reliability of the proposed method has been tested by computer simulations over a range of count densities. The results demonstrate that the proposed approach provides artifact-free images and parameter estimates comparable to those obtained with a ring detector system, as is typical of conventional PET. The technique can potentially be applied to data acquired using systems such as single or multi-detector SPECT, coincidence detection or low-cost PET systems

which involve detector rotation rather than a stationary ring of detectors. The techniques therefore have widespread clinical appeal.

Chapter 4 Minimum Dynamic SPECT Image Acquisition Time required for Tl-201 Tracer Kinetic Modeling

4.1 Introduction

Dynamic Single Photon Emission Computed Tomography (SPECT) and recent advances in attenuation and scatter correction have opened the possibility of quantifying physiological parameters with SPECT and tracers with suitable kinetics. Recently Iida et al have shown that absolute regional cerebral blood flow and volume of distribution can be calculated using dynamic Iodine-123 (I-123) SPECT and compartmental modeling [35,36]. Similarly, Onishi et al have applied dynamic SPECT to estimate receptor binding [99]. Technetium-99m (Tc-99m) teboroxime has been suggested for measuring myocardial blood flow. Teboroxime exhibits fast kinetics, which makes it unsuitable for traditional static SPECT imaging, but is well suited to estimating physiological parameters with short, fast dynamic acquisitions [34,100]. Iida et al have demonstrated the feasibility of estimating myocardial blood flow with Thallium-201 (Tl-201) dynamic SPECT, which exhibits much slower kinetics, more in line with typical SPECT tracers [30].

While dynamic SPECT studies have only recently gained increased attention, dynamic Positron Emission Tomography (PET) studies and compartmental modeling are well established. Great attention has been paid to the design of PET image frame sampling schedules to increase the quantitative accuracy. Hawkins et al [43] employed a series of simulations to evaluate temporal sampling in FDG kinetics studies, specially the effect of the length of the initial scans upon estimated parameter values. Mazoyer et al [44] proposed a general method for the evaluation of the precision of parameter estimates resulting from dynamic emission tomography studies and applied it in an analysis of the influence of the data acquisition protocol. Delforge et al [45] presented a general framework and

various criteria to measure the 'goodness' of an experimental protocol, which allows an optimization of the experimental design for any model. This methodology is applied to the estimation of receptor-ligand reaction model parameters with dynamic PET data. Jovkar et al [46] developed a procedure to compare scan schedules for the accuracy of parameter estimation by evaluating the variance-covariance matrix of the estimated parameters as an index of parameter accuracy. All these studies found that there is a monotonic improvement in the index of parameter accuracy with increasing sampling frequency and concluded that a higher sampling frequency (more image samples), particularly in the early stage, should be used.

However, it has been demonstrated [101] that the above conclusion was mainly due to using a cost function based on the assumption that sample points represent instantaneous activity concentration at the sample time, while in fact each sample point represents the integral of the changing activity concentration over the duration of the collection frame. The assumption of instantaneous sample points introduces increasing errors with increasing frames times, which prevents the reduction of the image frame numbers without adversely affecting accuracy. Therefore, Li et al used a modified cost function based on integrated activity concentration for PET modeling [47] and developed the optimum sampling schedule (OSS) algorithm. The OSS algorithm can systematically and automatically minimizes the image sampling number as well as achieving good accuracy and precision in parameter estimation. It provides a formalized methodology for determining the acquisition times of the minimum number of frames required to describe the selected kinetic model. Based on this approach, OSS for PET input function [73], PET output function [94], and whole-body PET image acquisition [102] have recently been investigated.

Nevertheless, with the exception of Chatziioannou et al [103] who performed some systematic analysis of total scan time as part of their data processing schemes to reduce noise, little attention has been paid to systematically

investigate the total scan duration. Instead total scan duration is usually decided empirically based on the following factors:

(1)   the physical and physiological half life of the radio-tracer;

(2)   the existence of blood metabolites;

(3)   model consideration (For example the C-11 acetate model is only validated for the initial 15 - 20 minutes);

(4)   the clinical consideration to keep the scan as short as possible for the convenience of patients.

In addition, clinical practicality is a particularly important consideration for dynamic SPECT sampling schedules. The slow kinetics of typical SPECT tracers may require unrealistically long total acquisition times to obtain reliable estimation of the slower rate constants. As shown by Iida et al, the number of frames and the total time the patient is in the scanner can be reduced by separating the study into two scanning sessions and assuming a single tissue compartment model [35,36]. Alternatively, some of the rate constants or their ratios can be set to fixed values to simplify the model and provide more reliable parameter estimation with limited data [104]. However, these assumptions may not be generally applicable to all SPECT tracers and a generally applicable methodology for optimizing sampling within the constraints imposed by dynamic SPECT would be of benefit.

The aims of this study were to:

(1)   systematically investigate the reliability of parameter estimation as a function of total acquisition time;

(2)   determine the minimum required continuous dynamic SPECT acquisition time for the relatively slow kinetics of Tl-201;

(3)   determine if there was a critical acquisition time length, beyond which little improvement in reliability is achieved;

(4)   investigate a clinically practical alternative to prolonged continuous dynamic acquisitions;

(5)   to determine if the reduced frames of OSS can provide similar accuracy as full dynamic acquisition for dynamic SPECT studies.

While this study concentrates on applying the methodology to Tl-201 kinetics, the methodology developed here should also be applicable to other dynamic SPECT studies.

4.2 Theory for the Proposed Method

4.2.1 Optimum Sampling Schedule

The optimum sampling schedule (OSS) technique provides a mechanism to maximize the information matrix, M, and, conversely, to minimize the covariance matrix of the estimated parameters by rearranging the sample intervals, based on the minimum number of required samples, and a given total study duration and model [94,105,106]. According to the Cramer-Rao theorem, the covariance matrix of an unbiased estimate, $\hat{p}$, of the parameter vector, p, is lower bounded by the inverse of M, i.e.

$$CV(\hat{p}) \geq M^{-1} \qquad (4.1)$$

Since the determinant of $CV(\hat{p})$ is proportional to the volume of the parameter confidence region [107], it provides a criterion for discriminating between various experimental protocols. The sampling schedule is adjusted iteratively to maximize the determinant of M ($det(M)$) as follows: Starting with the full dynamic sampling schedule, at each iteration, each interval is adjusted in turn in the direction which increases the $det(M)$ of the parameter estimates for the TTAC re-sampled with the adjusted interval. Adjusting interval i will also adjust interval $i+1$ by the same amount but in the opposite direction to maintain the same total collection time and avoid overlap. When the length of an interval falls below a set value (10 sec in this study), it is merged with the next interval provided that the merging increases the $det(M)$. The iterations are repeated until $det(M)$ converges to a specified tolerance. The OSS will depend on the exact shape of the TTAC. As this is unknown prior to the measurement, OSS derived for TTAC simulated from mean parameter set was used for all other parameter sets to investigate the applicability of a single OSS scheme to a range of Tl-201 kinetics.

The optimum sampling schedule methodology was also employed to find optimum sampling based on two sessions of scanning: A short (10-45 min) multi-frame acquisition immediately post tracer injection and a delayed single frame acquisition. The timing for the delayed frame is determined by adjusting the mid-scan time of the minimum number of required frames with fixed duration of 10 min within an overall time period of 240 min until again *det(M)* is maximized. This results in a mid scan time of 173 min for the last time point. A single 10 min frame is then fixed at 173 min and optimum sampling schedule technique is then applied to determine the sampling requirements for the first session. Sampling schedules are derived for total first session acquisition times ranging from 10 min to 45 min. This scheme is similar to current clinical studies, where an acquisition is performed soon after Tl-201 injection, followed by a redistribution study at around 3-4 hours. Thus the following optimum sampling schedules were investigated:

(1) Continuous data collection over the whole study duration (i.e., single session of scanning) ranging from 30-240 min, which is the conventional OSS approach.

(2) Initial data collection for a shorter period (10-45 min) accompanied by a delayed study at 173 min (i.e., two sessions of scanning)

4.3 Simulation Method

4.3.1 Simulations of Tissue Time Activity Curves

Simulated tissue time activity curves (TTAC) were derived from rate constants estimated from dynamic Tl-201 SPECT studies in 16 dogs. The dog studies were carried out as follows:

> The dogs were anaesthetized and positioned on a dual head gamma camera (Toshiba GCA7200). A transmission study was carried out using a line source at the focus of a fan beam collimator. The dynamic SPECT study was initiated at the start of a 3 min infusion of 110 MBq of Tl-201.

Frequent arterial blood samples were drawn throughout the dynamic study. The detectors rotated continuously completing a 360° acquisition every 15 sec. The 15 sec frames were added on-line to provide the following 42 frame dynamic sequence for resting studies: 10 x 1 min, 6 x 2 min, 3 x 4 min, 5 x 5 min and 18 x 10 min for a total acquisition time of 4 hours. Studies were also carried out in dogs with increased blood flow achieved by constant infusion of adenosine and reduced blood flow produced by beta-blockers. The total study duration for the adenosine and beta-blocker studies was limited to 1 hr.

Tl-201 data were corrected for scatter using transmission dependent scatter correction [108-110] and reconstructed with the ordered subset expectation maximization algorithm (OSEM) [61] using transmission data based measured attenuation correction. Regions of interest (ROIs) were drawn on a central slice through the myocardium for anterior, lateral, apical, septal and inferior myocardial areas and TTACs were generated. The TTACs were fitted with 1 and 2 tissue compartment models using non-linear least square fitting (Figure 4-1).
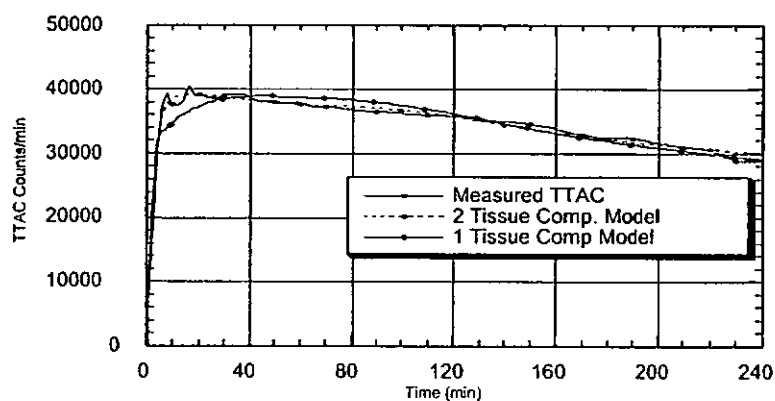
Figure 4-1 Measured tissue time activity curve from one of the dynamic SPECT dog studies fitted with 1 and 2 tissue compartment models. The 2 tissue compartment model provides a visually better fit to the measured TTAC than the 1 tissue compartment model.

From the results of the compartmental fitting, the two tissue compartments (extra-cellular and intra-cellular Tl-201 compartments - Figure 4-2) model was assumed for the simulations. This model is also in line with recent literature reports [111]. K_1 is the influx constant and is proportional to blood flow for a flow limited tracer like Tl-201. Other rate constants are as shown in Figure 4-2. TTACs were generated for the five selected sets of rate constants (K_1-k_4) given in Table 4-1. Rate constant sets were selected to cover a range of flow conditions. Set 1 represents mean rate constants from all 16 dogs, set 2 is from a dog with resting flow, set 3 and 4 from dogs with reduced flow induced by constant beta blocker infusion and flow for set 5 was increased by constant adenosine infusion over the study duration.
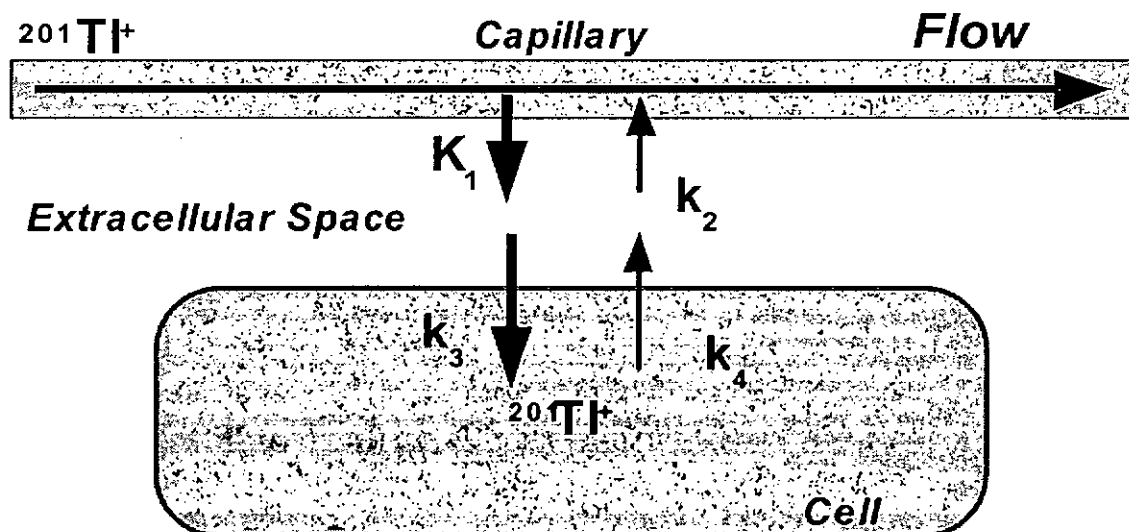
Figure 4-2 Assumed compartmental model for Tl-201 with two tissue compartments: extra-cellular and intra-cellular compartment.

	K_1	k_2	k_3	k_4	Vd
Set 1	0.68080	0.90024	0.14529	0.04136	34.1264
Set 2	0.72961	0.03595	0.04151	0.01554	74.5205
Set 3	0.18749	0.02068	0.06021	0.02004	36.3078
Set 4	0.25643	0.08405	0.25912	0.00926	88.3939
Set 5	1.51312	0.19493	0.28104	0.06796	39.8610

Table 4-1 The four rate constants (K_1-k_4) and the volume of distribution (Vd) for the five selected parameter sets. Units for the rate constants are min^{-1}.

The derived volume of distribution macro parameter (*Vd*) given by

$$Vd = \frac{K_I*(k_3+k_4)}{k_2*k_4}$$ (4.2)

is also shown in Table 4-1. Of particular interest were the influx rate constant K_1, which is related to blood flow (K_1 = flow * extraction fraction) and Vd, which is related to the cells' ability to concentrate Tl-201, an important indicator for viability. For each set of rate constants, time activity curves were generated by convolving the compartmental model function with the plasma time activity curve (PTAC) derived from the average of the 16 dogs (Figure 4-3).
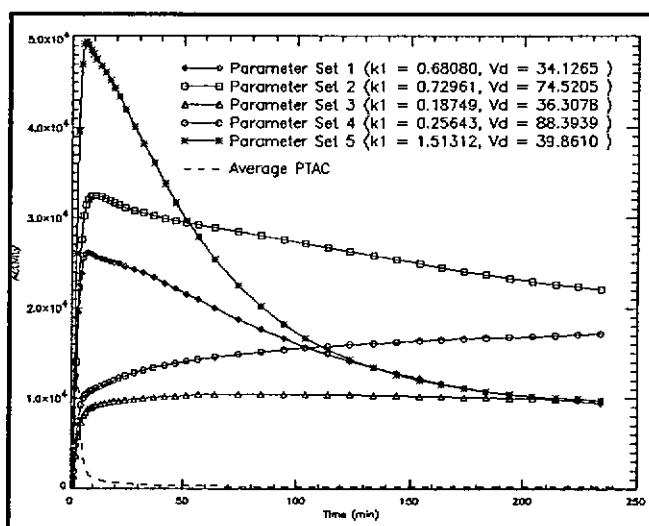
Figure 4-3 The average plasma time activity curve (PTAC) and the five noise free tissue time activity curves for the five selected parameter sets.

To simulate the actual environment and also to investigate the robustness of the proposed approach, adding measurement noise to the simulated data is necessary. In this simulation, the measurement noise was added to the samples of TTAC using the variance structure described in Equation 2.24. Five different noise levels were investigated with c = 2, 10, 23, 41 and 65. A simulated TTAC with c=65 is shown in Figure 4-4 together with the corresponding measured TTAC curve from the dog ROI analysis. The estimated noise coefficient of variation (CV) near the peak counts and for 1 min samples ranged from 1.8% to 9.2% for the simulations with c = 2 to 65, respectively. Estimated noise CV for

the measured TTAC was approximately 3-5%, corresponding approximately to a noise constant between $c = 10$ and $c = 23$.
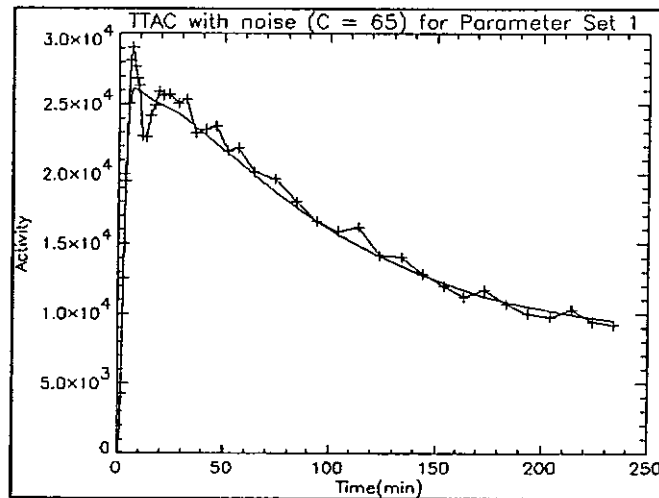
Figure 4-4 A measured TTAC (solid line) and corresponding simulated TTAC (crossed line) with noise constant C=65.

4.3.2. Evaluation of OSS

The coefficient of variation (CV) and error in estimating the parameters were evaluated for both the continuous (OSS-1) and the two session (OSS-2) optimum sampling schemes and compared to conventional full dynamic sampling (as used in the original dog studies) for both the continuous (DynSS-1) and the two session sampling schemes (DynSS-2) using Monte Carlo simulation technique as follows:

1. For each selected parameter set, noiseless TTACs were generated by convolving the compartmental model function with the PTAC, according to the different sampling schedules.

2. Noise was then added to the noiseless TTACs at the 5 noise levels according to Equation 2.24. For each noise level, 100 curves were generated using different noise seeds.

3. Rate constants were estimated with non-linear least square curve fitting from the simulated data. The modified cost function [94], based on the integral counts over the frame duration, was used for the fitting. The fitted rate constants were constrained to be positive.

4. Coefficient of variations (CV) were determined for each parameter from the 100 curve fits. Error was calculated by comparing the mean fitted parameters to the known parameter values used for generating the TTACs.

4.4 Simulation Results

4.4.1 Optimum Sampling Schedule

Table 4-2 shows the optimum sampling schedule OSS-1 as well as the full dynamic sequence DynSS-1. It should be noted that for different study duration, the number of samples for DynSS-1 ranged from 18 samples for 30 minutes to 42 samples for 4 hours. For OSS-1, there were only 4 samples, which is the minimum number of samples required to estimate the four parameters (K_1-k_4) used in the model [101]. Table 4-3 shows the sampling schedule for OSS-2 and DynSS-2, using the same notation as Table 4-2. The schedules taken in different sessions are separated by square brackets. The results of the optimized intervals are shown in the right column of the table and the optimized mid-scan time for the second session was 173 minutes post-injection. As indicated before, these OSS were derived for TTAC simulated from mean parameter set (Set 1 in Table 4-1) and were used for all other parameter sets to investigate the applicability of a single OSS scheme to a range of Tl-201 kinetics

Total Length	DynSS-1	OSS-1
30 min	10x1 min, 6x2 min, 2x4 min	1x5 min, 1x7 min, 1x11 min,1x6 min
45 min	10x1 min, 6x2 min, 3x4 min, 2x5 min	1x5 min, 1x5 min, 1x18 min, 1x11 min
60 min	10x1 min, 6x2 min, 3x4 min, 5x5 min	1x5 min, 1x10 min, 1x25 min, 1x19 min
90 min	10x1 min, 6x2 min, 3x4 min, 5x5 min, 3x10 min	1x5 min, 1x10 min, 1x38 min, 1x36 min
120 min	10x1 min, 6x2 min, 3x4 min, 5x5 min, 6x10 min	1x6 min, 1x11 min, 1x48 min, 1x54 min
150 min	10x1 min, 6x2 min, 3x4 min, 5x5 min, 9x10 min	1x6 min, 1x11 min, 1x57 min, 1x75 min
180 min	10x1 min, 6x2 min, 3x4 min, 5x5 min, 12x10 min	1x6 min, 1x11 min, 1x63 min, 1x99 min
210 min	10x1 min, 6x2 min, 3x4 min, 5x5 min, 15x10 min	1x6 min, 1x12 min, 1x68 min, 1x124 min
240 min	10x1 min, 6x2 min, 3x4 min, 5x5 min, 18x10 min	1x6 min, 1x12 min, 1x71 min, 1x151 min

Table 4-2 Sampling schedules for single session of scanning. The left, middle and right columns show the total study duration, the sampling schedules of the DynSS-1 and OSS-1, respectively. The first entry "10x1min" in the middle column means that 10 samples, each 1 minute long, were taken.

Protocol	DynSS-2	OSS-2
(A)10 min + 10 min	[10x1 min],[1x10 min]	[1x4 min, 1x4 min, 1x2 min],[1x10 min]
(B)20 min + 10 min	[10x1 min, 5x2 min],[1x10 min]	[1x5.5 min, 1x7.5 min,1x7 min],[1x1 0min]
(C)30 min + 10 min	[10x1 min,6x2 min,2x4 min],[1x10 min]	[1x5 min,1x 8 min, 1x17 min],[1x10 min]
(D)45 min + 10 min	[10x1 min,6x2 min,3x4 min,2x5 min],[1x10 min]	[1x5 min, 1x10 min, 1x30 min],[1x10 min]

Table 4-3 Sampling schedules for two sessions of scanning using the same notation as in Table 4-2. The samples taken at different session are separated by square brackets. The first session is taken immediately after tracer injection and second session is taken at 173 minutes post injection.

4.4.2 Percentage Errors and CV - Single Session Scanning

The percentage error for the fitted parameters was calculated by comparing them to the known parameter values used for the simulation. CV was estimated from the variation of parameters over the 100 Monte Carlo simulation runs. The percentage error and CV of estimated K_1, k_2, k_4 and Vd for set 1 at the 5 noise levels are plotted as a function of total study duration for DynSS-1 in Figure 4-5 and for OSS-1 in Figure 4-6. Curves for k_3 were very similar to those of k_2 and are thus not shown. Little systematic change in either percentage error or CV of K_1 is observed as the length of collection time increased from 30 minutes to 4 hours. As the length of collection time increased, both percentage error and CV for k_2, k_3, k_4 and Vd tended to decrease to a plateau at 60 - 90 minutes for both DynSS-1 and OSS-1. Before the plateau, the percentage error increased with the noise level. Little effect of noise on percentage error was observed after the plateau. In contrast, CV was influenced by noise level for all study duration. CV for OSS-1 and DynSS-1 were very similar as were the percentage errors for parameters K_1, k_4 and Vd. However, percentage errors for k_2 and k_3 were more than twice as large for OSS-1 than for DynSS-1.
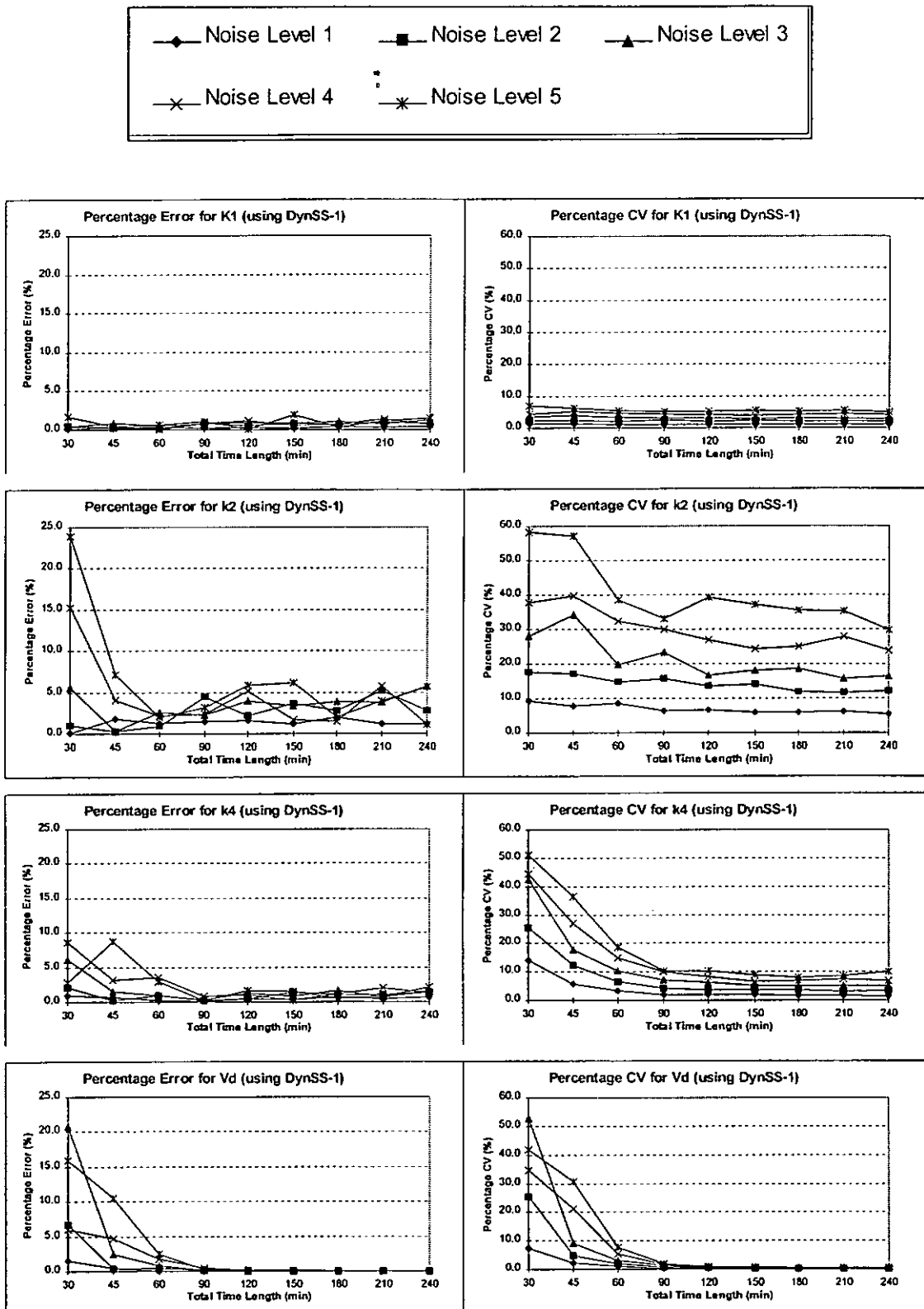
Figure 4-5 Percentage error (left set of graphs) and CV (right set of graphs) of, from top to bottom, estimated K_1, k_2, k_4 and Vd as a function of total sampling time for full dynamic sampling schedule (DynSS-1). For each parameter, percentage error and CV are plotted at each of the 5 noise levels. Results are for parameter set 1. The same y-axis scale has been used for percentage error of all parameters and also for CV to facilitate comparison.
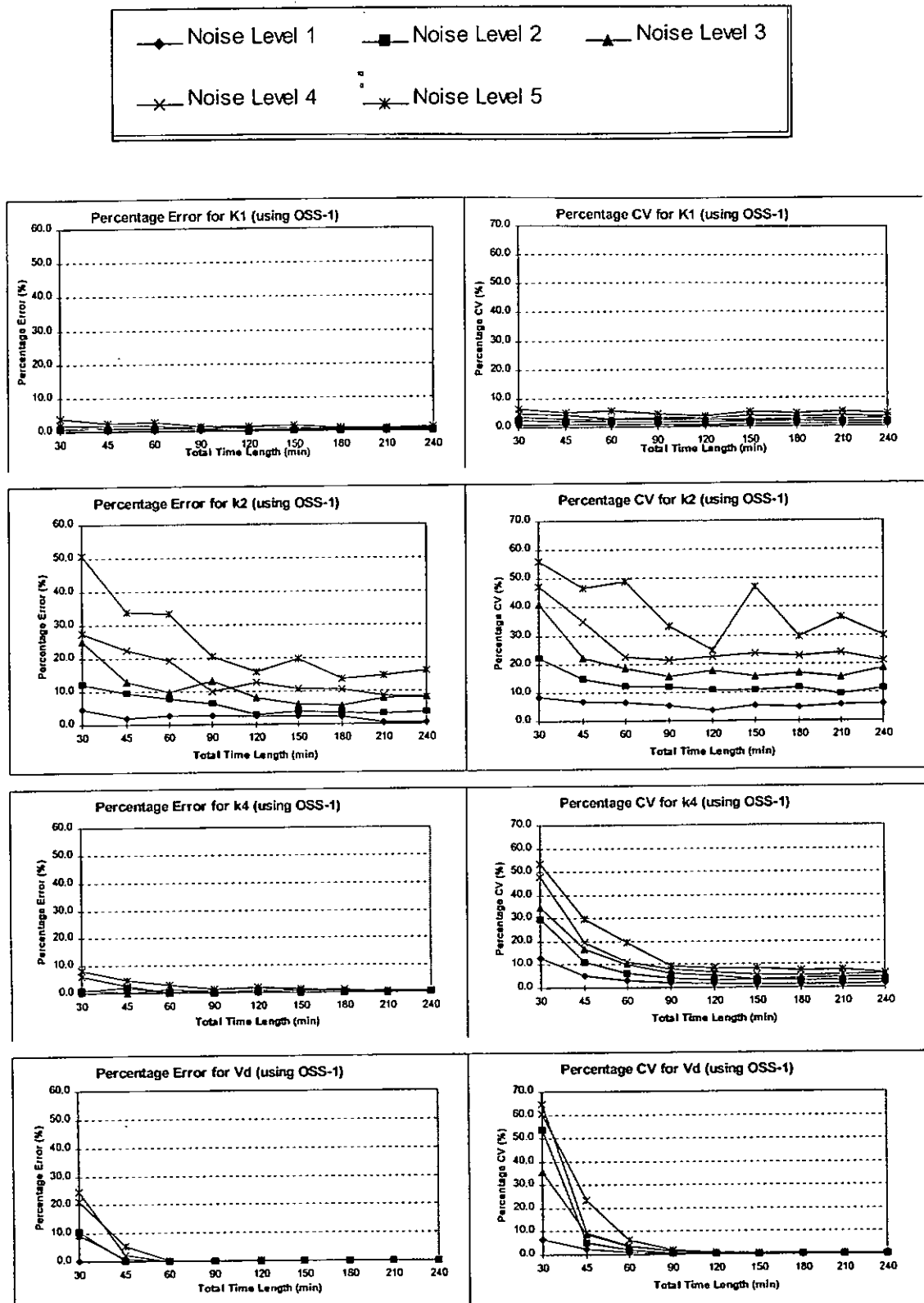
Figure 4-6 Percentage error (left set of graphs) and CV (right set of graphs) of, from top to bottom, estimated K_1, k_2, k_4 and Vd as a function of total sampling time for optimum sampling schedule (OSS-1). For each parameter, percentage error and CV are plotted at each of the 5 noise levels. Results are for parameter set 1. The same y-axis scale has been used for percentage error of all parameters and also for CV to facilitate comparison.

Figure 4-7 is a comparison of the percentage error and CV of the estimated K_1 at different total study duration, for different parameter sets using DynSS-1 or OSS-1. These curves are the average of the results obtained at the different noise levels. The figures show that the percentage error and CV are all below 4% and 11%, respectively. Both percentage error and CV do not decrease as the total time length is increased, i.e. K_1 estimation is not improved by extending the scanning time. Therefore, a 30 minute scanning session is sufficient if only the blood flow indicator K_1 is of interest.

(a)   (b)

(c)   (d)
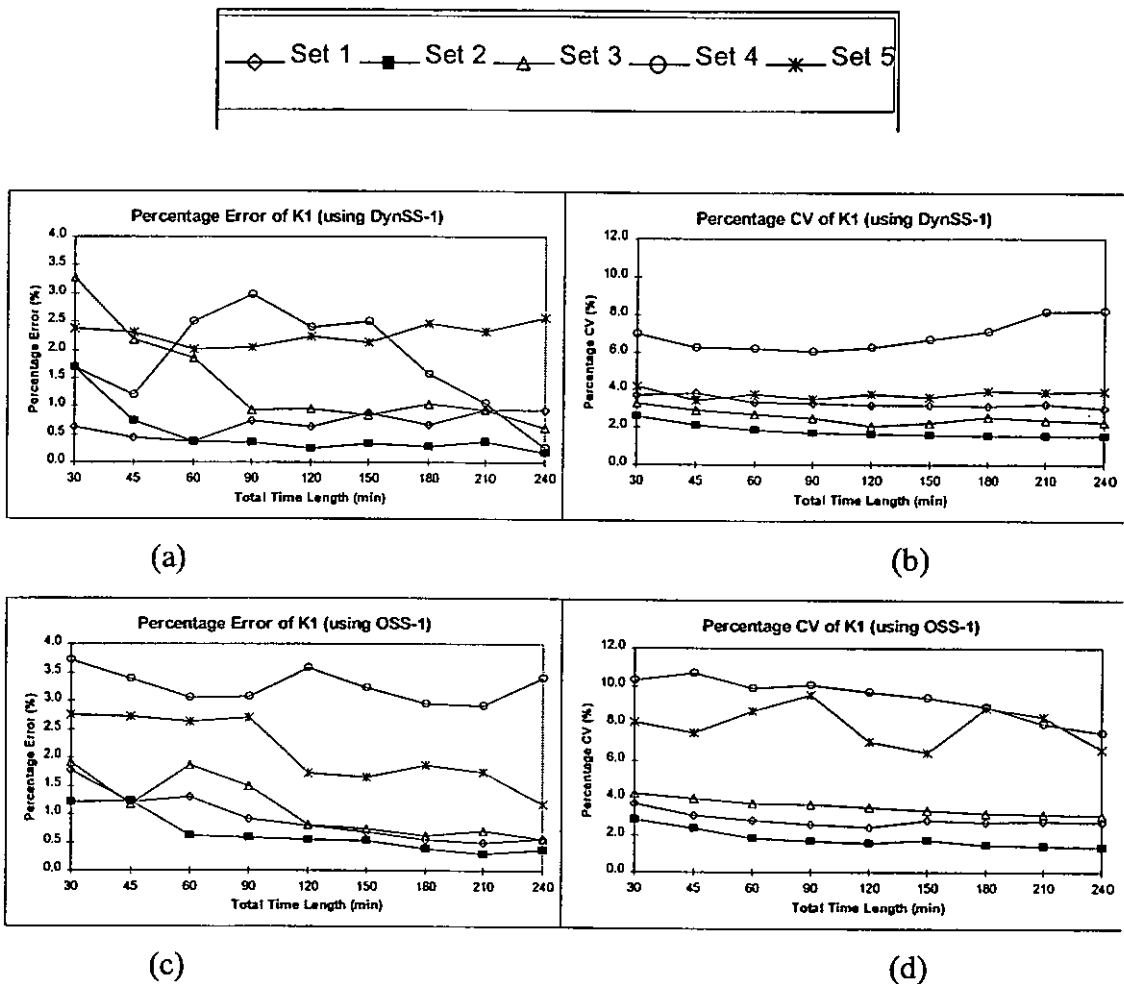
Figure 4-7 Comparison of percentage error and CV for the estimated K_1 at different total time lengths for full dynamic sampling schedule (graphs a and b) and optimum sampling schedule (graphs c and d). Set 1 to Set 5 represent the five selected parameter sets.

Figure 4-8 shows the percentage error and CV of the estimated Vd at different total time lengths of scanning, for different parameter sets and for both DynSS-1 and OSS-1. There is a marked improvement in both percentage error and CV as the scanning time is increased from 30 minutes to 120 minutes. Thereafter, both percentage error and CV decrease to a plateau. To obtain a less than 20% error and CV for Vd, a minimum scanning time length of 120 minutes is required, which may be reduced to 90 minutes if somewhat higher CV of <30% is tolerated in low flow regions.

(a)   (b)

(c)   (d)
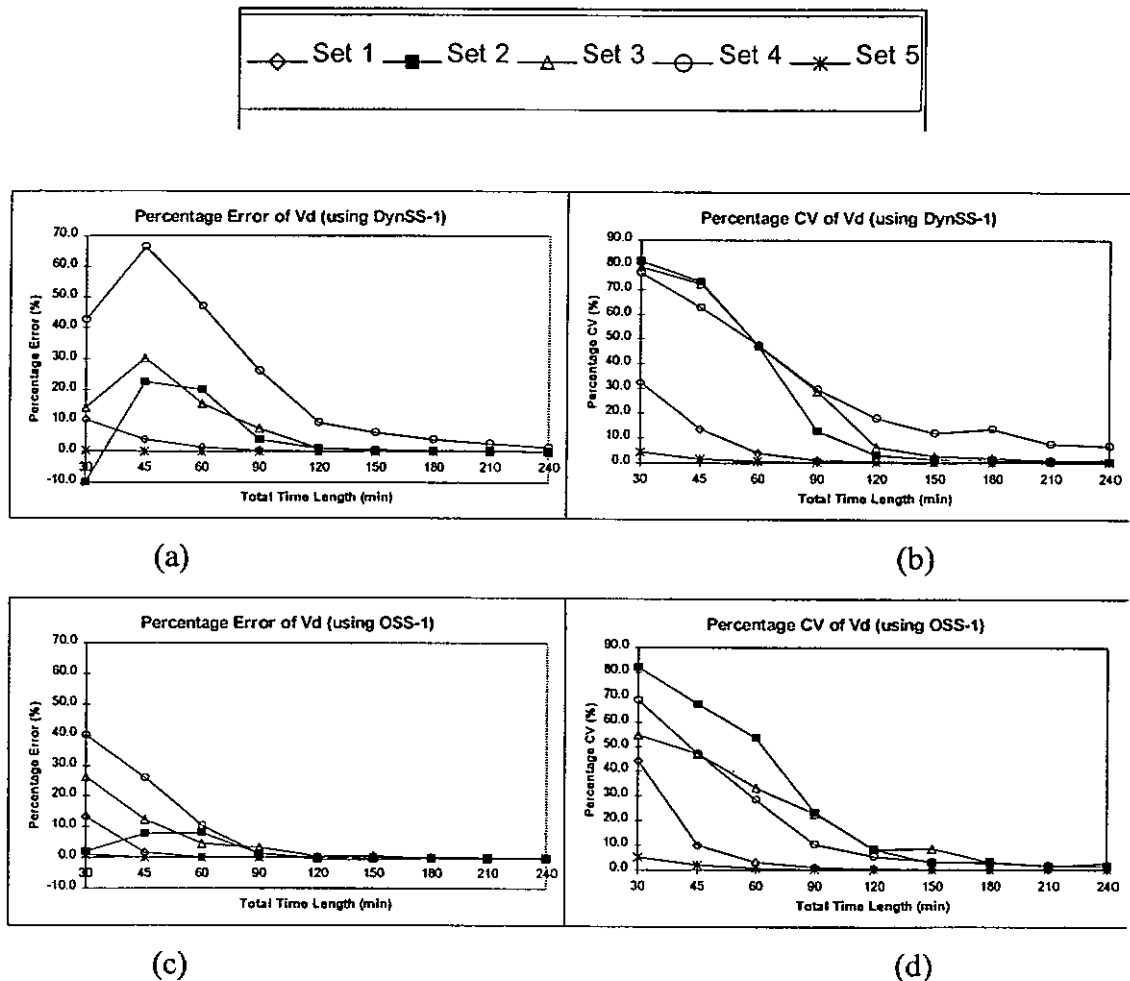
Figure 4-8 Comparison of percentage error and CV of the estimated volume of distribution (Vd) at different total time lengths for full dynamic sampling schedule (graphs a and b) and optimum sampling schedule (graphs c and d). Set 1 to Set 5 represent the five selected parameter sets.

4.4.3 Percentage Errors and CV - Separate scanning sessions

An overall summary of K_1 and Vd estimation as a function of sampling schedule is shown in Figures 4-9 and 4-10. For K_1 estimation, an initial 10-20 minute dynamic in combination with a delayed sample or a single 30 minute dynamic are sufficient. With addition of the delayed scan at approximately 3 hours, the initial dynamic can be reduced to 30 minutes and still achieve similar accuracy and CV for Vd as a full 120 minute scan. However, the 30 minute dynamic plus 10 minute delayed sample is considerably more practical in a routine clinical setting, being similar in acquisition times to current rest-redistribution protocols.
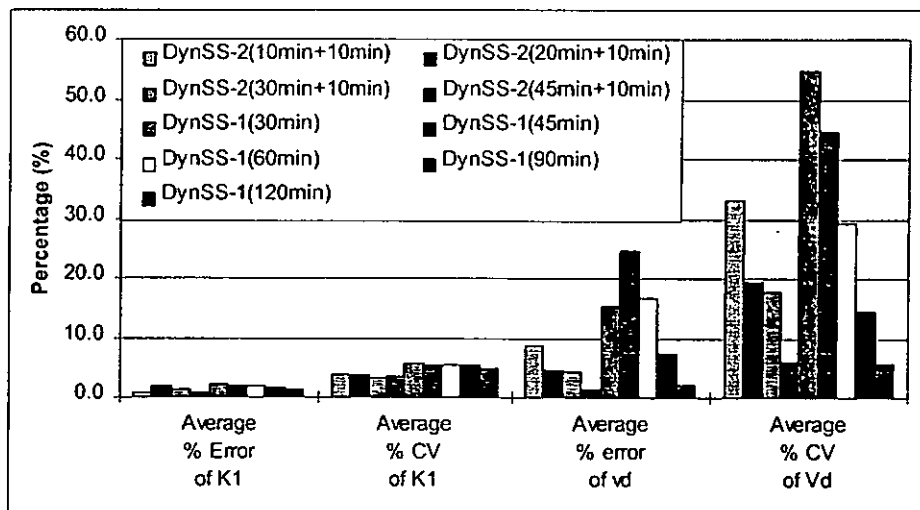
Figure 4-9 Comparison of 2 session (DynSS-2) and 1 session (DynSS-1) full dynamic sampling schedule. The values inside the brackets are the length of the study duration. Average results of the 5 parameter sets are shown.
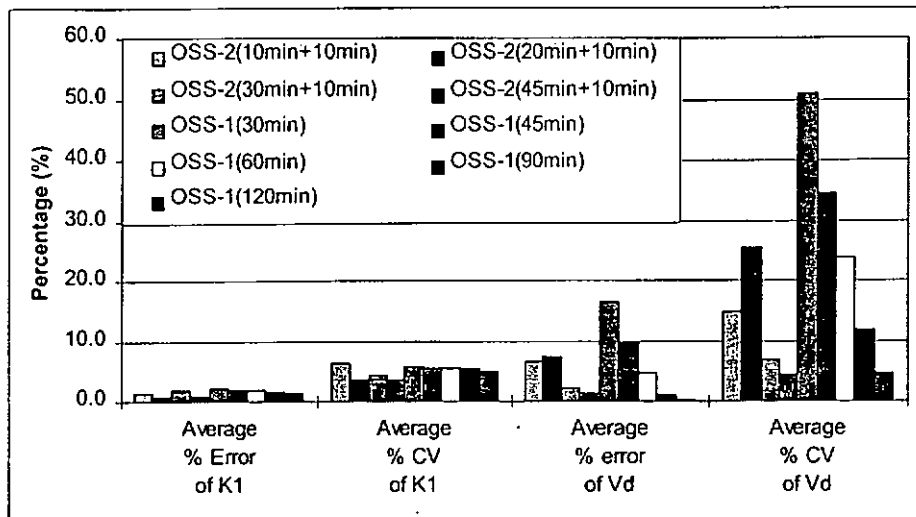
Figure 4-10 Comparison of 2 session (OSS-2) and 1 session (OSS-1) optimized sampling schedule. The values inside the brackets are the length of the study duration. Average results of the 5 parameter sets are shown.

4.5 Discussion

In this study we systematically investigated the reliability of parameter estimation as a function of acquisition time and applied the OSS technique to determine optimized, practical sampling schedules for dynamic Tl-201 SPECT. We found that: 1) Optimum sampling schedule can provide reliably estimates of both K_1 and Vd, comparable to that of full dynamic sampling which often requires to record far more images. 2) K_1 can be estimated with a relatively short study duration of 30 minutes, while estimation of Vd requires at least 90-120 minutes to achieve acceptable precision, highlighting the need for careful selection of study duration to obtain reliable estimates of the parameters of interest. 3) Dividing the scanning into early and delayed sessions allowed accurate estimation of Vd, without requiring an unacceptably long collection time.

4.5.1 Comparison of DynSS and OSS

The optimum sampling scheme generally has a performance comparable to that of full dynamic sampling scheme for estimating K_1 and Vd. Only at very high K_1 (set 5) and low K_1 and high Vd (set 4) is there an appreciably increased CV of K_1 for OSS-1 compared with DynSS-1 (Figure 4-7). Even in these cases, the increase in CV is not excessive and is only in the order of 3-4%. Nevertheless, OSS-1 cannot successfully separate k_2 and k_3 rate constants. The percentage errors for these two rate constants using OSS-1 was more than double that of DynSS-1 (Figures 4-5 and 4-6). Thus if accurate estimates of k_2 and k_3 are required, DynSS-1 is the preferred sampling method.

The optimum sampling schedule substantially reduces the number of required SPECT acquisition frames to only 4, irrespective of total acquisition time, compared with the 18-42 acquisition frames for the full dynamic study. As a result, it can significantly reduce the amount of dynamic image data (and hence the storage space) and speed up the data analysis process in daily clinical applications. The shortest acquisition frame time for OSS is 5 minutes, compared to 1 minute for the DynSS, which makes OSS dynamic SPECT readily implementable on existing SPECT systems.

4.5.2 Minimum time for the measurement of K_1 and Vd

For both OSS-1 and DynSS-1, we found that a 30 minute scanning time length is sufficient for an accurate estimation of K_1 alone (Figures 4-7 and 4-8). Prolonging the scanning time beyond 30 minutes produces no appreciable gain in accuracy or CV. For the 30 minute study duration, percentage errors and CV for Vd are greater than 50% (Figures 4-9 and 4-10). To obtain an accurate estimation for Vd, a 90-120 minute study duration is necessary. This finding is not unexpected, as early uptake of Tl-201 is predominantly related to flow, thus the early dynamics are mostly determined by flow. However, the typically >30 ml/ml Vd of Tl-201 results in slow redistribution, particularly in low flow areas.

Thus, a relatively long study duration is required to obtain reliable estimates of Vd.

For continuous data acquisition sampling schemes (OSS-1 and DynSS-1), patients would be required to remain in the camera for 90-120 minutes to obtain accurate estimates of Vd. This is clearly impractical for routine clinical studies. We thus investigated an alternative sampling scheme, based on a short dynamic at the start of the study and a short delayed scan. We again used the formalism of OSS to find the optimum mid scan time at around 3 hr for the delayed scan and the sampling schedule of the early, short dynamic. With an initial 30 minute dynamic study, accuracy and precision were similar to a continuous collection over 90-120 minutes for both K_1 and Vd (Figures 4-9 and 4-10). The time requirements for the split session sampling scheme are similar to current Tl-201 rest/redistribution studies, and are thus clinically practical. Further, estimation of K_1 and Vd should eliminate the need for 24 hours images, which may in fact reduce the total study time.

4.5.3 Effect of TTAC on OSS Accuracy

The optimum sampling schedule depends on the shape of the TTAC curve. Thus OSS for Tl-201 will vary depending on the exact shape of the TTAC for a particular subject and region, which is not normally known a priori. In this study we determined the OSS based only on TTAC for parameter set 1 and applied this OSS to all the other parameter sets, which were specifically chosen to cover a wide range of K_1 and Vd and hence a wide range of TTAC shapes (Figure 4-3). The results shown in Figures 4-7 and 4-8 demonstrate the validity of using a single OSS schedule for a wide range of TTACs. No systematic difference in percentage error as a function of TTAC is seen between OSS and DynSS. Only CV for K_1 is increased by approximately 3-4% for set 4 and set 5, which represent the extreme deviation from the average TTAC (set 1) used to generate the optimum sampling schedule (Figure 4-3).

In this study we have concentrated on the sampling requirements for the estimation of compartmental model rate constants. Nevertheless, for practically applying the SPECT systems for dynamic studies, a further step is required to accurately estimate the activity in the myocardium with a prerequisite of both accurate attenuation and scatter correction as well as partial volume effects correction. Fortunately, with the increased availability of transmission measurements on particularly multi-detector SPECT systems and algorithms for scatter correction [108-110], quantitative SPECT is becoming more feasible and practical and has in fact been applied to the dog studies used as the basis of this investigation. For compartmental modeling, the arterial plasma concentration of the tracer is also required. Ideally, this is obtained by frequent arterial blood sampling, which is, however, considered too invasive for routine clinical studies. In Chapter 5, we will present a blind deconvolution approach to eliminate the input function requirement for FDG studies and the technique should also be applicable to Tl-201 studies.

4.6 Summary

In this study, we have developed a methodology determining the total acquisition time for optimizing sampling schedule used in dynamic SPECT studies. When applied to dynamic SPECT Tl-201 model, it was found that for myocardial blood flow only, a 30 minute scanning duration is sufficient. Vd estimation requires an additional study at approximately 3 hours, which avoids the need for prolonged continuous dynamic acquisition. Both K_1 and Vd can thus be determined with a clinically practical sampling schedule. This study also highlights that careful consideration needs to be given to total acquisition time to obtain reliable estimates of all parameters of interest, particularly for typical SPECT tracers with slow kinetic components. The method for determining optimum sampling schedule and total acquisition time applied here to Tl-201 should also be applicable to other SPECT tracers.

Chapter 5 Non-Invasive Quantification of Physiological Processes with Dynamic PET using Blind Deconvolution

5.1 Introduction

As introduced in the previous chapters, a prelude requirement of tracer kinetic modeling is the measurement of tracer concentration in blood plasma, i.e. plasma time activity curve (PTAC), which acts as the input function to the tracer kinetic model. PTAC is usually obtained by direct arterial blood sampling (See Section 2.6.1). This process is invasive, time-consuming and requires extra-staff. It also exposes clinical personnel to the danger of radiation and fatal blood infection. Therefore, alternative methods which enable quantification of physiological processes with reduced number of blood samples would be beneficial.

Stefan et al proposed using a population-based input functions (IFs), that were calibrated with two arterialized-venous (a-v) blood samples, in the measurement of regional cerebral metabolic rate of glucose (rCMRGlu) [48]. The population-based IFs were derived from (1) the average of IF from 26 patients and (2) a published model of fluoro-deoxy-2-glucose (FDG) plasma concentration [72]. Their results show that the values for rCMRGlu calculated with different IFs were highly correlated for both non-diabetic and diabetic patients. Although this approach significantly simplifies the measurement of rCMRGlu and requires only two a-v blood samples for calibration, the process of blood sampling, however, cannot be completely eliminated.

Burger et al has examined the possibility of mathematical metabolite correction [49]. The mathematical metabolite correction was implemented by first approximating the input curve after its peak activity by a sum of three decaying

exponentials. The amplitudes and characteristics half times of which were then estimated together with the kinetic tissue parameters using a weighted least squares curve fitting routine. Assessment of the method with simulated data proved its theoretical feasibility. However, this method assumes that the input curve until peak activity has been measured, i.e. we still need to take blood samples at the beginning of dynamic study.

Recently, Carson et al [50] and Watabe et al [51] have proposed techniques that completely eliminate the process of blood sampling. Both methods are developed for estimating the regional cerebral blood flow (rCBF) using PET. Carson et al developed a method to estimate the N flow values and the input function, containing M sample points, simultaneously based on the NxM measurements (M image frames and N pixels for each image frame) with weighted least squares optimization. Watabe's approach is based on the simultaneous analysis of regions with different flows and the algebraic elimination of the arterial input function terms. However, both methods are developed for single compartment model and their extensions to more complex models, e.g. FDG model, still need further investigation. In fact, the solutions are likely to be computationally demanding.

In this chapter, we propose an approach to estimate the physiological parameters for a pre-assumed tracer kinetic model when performing dynamic PET studies, eliminating the requirement of measuring PTAC. The approach consists of two major steps. First, the wavelet transform is used for the denoising of projection data [112]. Second, an eigen-vector based multi-channel blind deconvolution [113] algorithm is applied to estimate the physiological parameters using the dynamic images reconstructed from the denoised projections. This technique is applied to estimate the rCMRGlu based on the FDG model [64]. The performance of the proposed approach is demonstrated using the Monte Carlo simulation. The result illustrates that the proposed approach can provide a comparable performance as that of invasive approach which requires the input curve to be measured.

5.2 Theory for the Proposed Method

The fundamental of the proposed approach is the use of a blind deconvolution technique which is based on eigen-vector decomposition. Since the computation of eigen-vector is sensitive to noise, we employed a denoising step before the blind deconvolution. In this study, we use a wavelet denoising approach [112] to filter the noise appeared in the projections. The denoised projections are then reconstructed using filtered back-projection to give dynamic images. Based on these dynamic images, tissue time activity curves (TTACs) are extracted from regions of interest (ROIs). Finally, blind deconvolution is applied to estimate the kinetic parameters. In the following sections, we will describe how the wavelet denoising and blind deconvolution are applied to the problem.

5.2.1 Wavelet Denoising

Among the numerous denoising methodologies in the literature, linear low pass filtering [114,115] is the most commonly used approach since it is easy to implement with the standard convolution back-projection reconstruction method. However, the linear low pass filtering approach unavoidably blurs the edges and causes the loss of structural information of the original image. Another way of denoising is to model the emission process as a random process and to use reconstruction algorithms based on the statistical model. Shepp and Vardi [58] proposed a Poisson process model for emission tomography which seems to be an excellent model. Maximum likelihood (ML) [58] and maximum a posteriori (MAP) [116] methods based on this model provide alternative solutions for reconstruction from noisy sinogram data. The problem with the ML and MAP techniques is that they are computational expensive. Therefore, in this study, we choose to use a wavelet transform based denoising approach [112] applied to the tomographic data that are contaminated with Poisson noises. Wavelet denoising has the advantage of preserving the structural information of the image when filtering the noise. In addition, when comparing with other wavelet denoising

approaches [117,118], the chosen approach also has the advantages of non-iterative reconstruction and simple computation which make it favorable for daily clinical usage. In the following sections, we will give a brief introduction of the approach. For more details, we refer the reader to [112].

First, we define the two-dimensional discrete dyadic wavelet transform [117] of the sinogram p to be $\{ S_{2^j} p, (W^1_{2^j} p)_{1 \leq j \leq J}, (W^2_{2^j} p)_{1 \leq j \leq J} \}$ where

$$S_{2^j} p = p \otimes \phi_{2^j}(x,y), \quad W^1_{2^j} p(x,y) = p \otimes \varphi^1_{2^j}(x,y)$$

and $\quad W^2_{2^j} p(x,y) = p \otimes \varphi^2_{2^j}(x,y)$ (5.1)

and the wavelets are designed to be the partial derivatives of a smoothing function along x-direction and y-direction, respectively. Denote also the modulus, $M_{2^j} p(x,y)$, and phase, $A_{2^j} p(x,y)$, of wavelet transform as

$$M_{2^j} p(x,y) = \sqrt{\left| W^1_{2^j} p(x,y) \right|^2 + \left| W^2_{2^j} p(x,y) \right|^2}$$

and $\quad A_{2^j} p(x,y) = \arctan\left(W^1_{2^j} p(x,y) \middle/ W^2_{2^j} p(x,y) \right)$ (5.2)

$M_{2^j} p(x,y)$ and $A_{2^j} p(x,y)$ indicate the magnitude and orientation of the gradient vector of the wavelet coefficient at a particular point (x,y). The orientation of the gradient vector of the wavelet coefficients will indicate the direction of maximum local variation of a signal. The first step of the algorithm is to compute the "directional sum" of the wavelet transform modulus, $N_S p$ [112], inside the so-called directional cone of influence, D_S, with the direction indicated by $A_{2^j} p(x,y)$. $N_S p$ at scale s is defined as follow:

$$N_s p(x_0, y_0) = \int_{(x,y) \in D_s} M_s p(x,y) dx dy$$ (5.3)

The term directional cone of influence is referred to [112]. Based on the $N_S p$ calculated at different scale, we compute the inter-scale ratio defined as

$$\text{inter-scale ratio} = N_{2^{j+1}} p(x_0, y_0) / N_{2^j} p(x_0, y_0)$$ (5.4)

It has been shown [117] that we can use the inter-scale ratio condition to discriminate irregular parts of the signal. For wavelet coefficients arising from noise component, the inter-scale ratio will be less than 2, while for those

coefficients corresponding to edges or more regular parts, the inter-scale ratio will be equal to or larger than 2. This provides a simple means for denoising. However, it has also been shown in [112] that, small irregular signals may falsely fulfill the above condition. Therefore, the inter-scale difference condition is also introduced to reject small irregular signal,

$$N_{2^{j+1}} p(x_0, y_0) - N_{2^j} p(x_0, y_0) > \gamma \qquad (5.5)$$

where γ is a threshold. Therefore, we select the wavelet coefficients if the computed inter-scale ratio is equal to or larger than 2 and the inter-scale difference above a certain threshold. Based on the selected wavelet coefficients, we reconstruct the denoised projections using inverse wavelet transform. The denoised projections will be used to reconstruct the dynamic images using the filtered back-projection algorithm. From these images, TTACs from ROIs are extracted and are fed to the blind deconvolution step for estimating the kinetic parameters.

5.2.2 Blind Deconvolution

The study of blind deconvolution attracts much importance recently in the areas of communication, signal processing, as well as geophysics. Its major objective is to estimate the input or the system transfer function only from their convolution output. This seemingly impossible problem has been shown to have unique solution. The current blind deconvolution approaches can be divided into two classes. The ones that rely on high order statistics [119] often require the input function to fulfill a certain kind of statistical characteristics, e.g. identical and independent distribution (i.i.d.), that may be difficult to achieve in some applications. The ones that rely on second order statistics seem to have less requirement on the input data and transfer function that allow them to be applicable to more general problems [113]. In this study, a multi-channel blind deconvolution technique in this class is adopted.

A block diagram for the problem of multi-channel blind deconvolution is shown in Figure 5-1. It is assumed that the number of unknown channels is greater than

one. For simplicity and illustration purpose, we consider the unknown channel

system consists of two channels, each of which is represented by an FDG model.
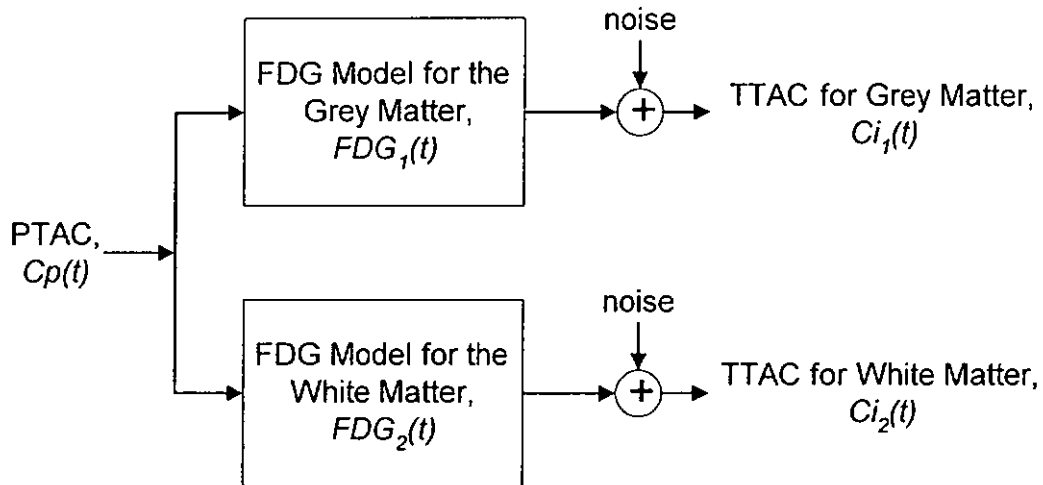
Figure 5-1 Block diagram for the problem of multi-channel blind deconvolution.

As applied to our problem, both unknown channels are fed by the same unknown

input function which is the PTAC, *Cp(t)*. The output signals of the unknown

system are the TTACs, $Ci_i(t)$. These curves are the results of the convolution

integral of PTAC with the impulse response of the FDG models, $FDG_i(t)$, given

as below:

$$Ci_i(t) = FDG_i(t) \otimes Cp(t) \quad i = 1,2 \tag{5.6}$$

Provided an appropriate sampling rate, the convolution integral as shown in (5.6)

can be approximated by a discrete linear convolution. The advantages of using a

discrete linear convolution rather than a convolution integral are, first, we can

speed up the computation, and more importantly, we can apply various well-

established digital signal processing techniques to improve the performance in

estimating the physiological parameters. Nevertheless, it is never possible to

attain such a sampling rate in real practice. For TTAC, usually only 22 samples

taken in an irregular time interval are obtained. Fortunately, due to the

smoothness of the input and output functions, the discrete linear convolution can

still be used by re-sampling the irregularly sampled data to the required sampling

rate using an interpolation. Figure 5-2 shows a typical PTAC generated using the

PTAC model described in Section 2.6.2. Figure 5-3 shows the FDG model

functions (given by Equation 5.7). The parameters for these model functions are

given later in the simulation section. Figure 5-4 shows the TTACs obtained by mathematically performing the convolution integral to the PTAC and the FDG models. Figure 5-5 shows the TTACs by applying the discrete linear convolution with the re-sampled PTAC and FDG models. The difference of them in average is less than -54 dB. This result shows that we can safely approximate the convolution integral in (5.6) by discrete linear convolution.
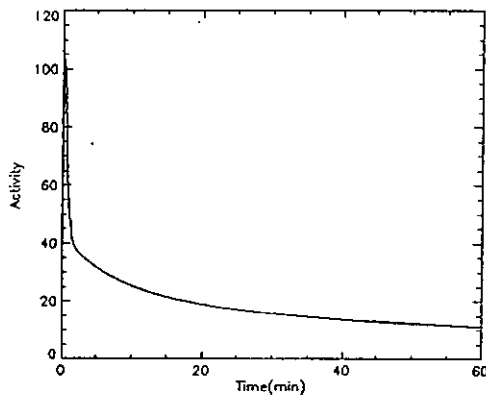
Figure 5-2 A typical PTAC.
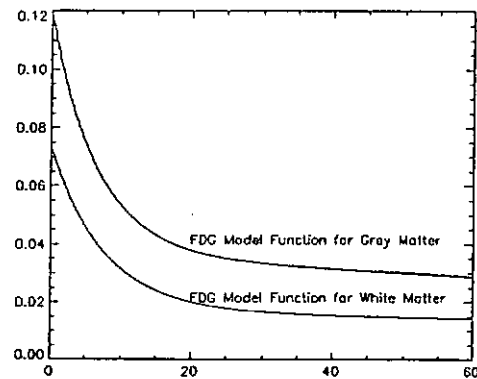
Figure 5-3 FDG model functions.
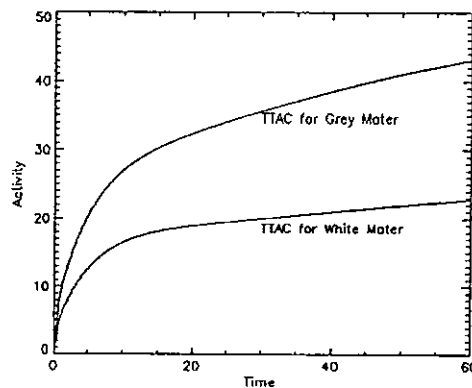
Figure 5-4 TTAC obtained by mathematically performing the convolution integral to the PTAC and the FDG models.
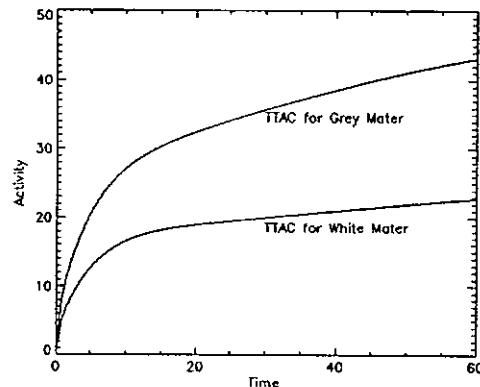
Figure 5-5 TTAC by applying the discrete linear convolution with the re-sampled PTAC and FDG models.

The two unknown channels of the system are the FDG models with different kinetics of, for example, brain grey matter (Region 1) and white matter (Region 2), respectively. The impulse response of the FDG model, $FDG_i(t)$, is given by the following equation (See Section 2.5.1):

$$FDG_i(t) = B_{i,1}e^{-L_{i,1}t} + B_{i,2}e^{-L_{i,2}t} \qquad i = 1,2 \qquad (5.7)$$

where

$$L_{i,1} = (k_{i,2} + k_{i,3} + k_{i,4} - \sqrt{(k_{i,2} + k_{i,3} + k_{i,4})^2 - 4k_{i,2}k_{i,4}})/2$$

$$L_{i,2} = (k_{i,2} + k_{i,3} + k_{i,4} + \sqrt{(k_{i,2} + k_{i,3} + k_{i,4})^2 - 4k_{i,2}k_{i,4}})/2$$

$$B_{i,1} = \frac{k_{i,1}}{\alpha_{i,2} - \alpha_{i,1}}(k_{i,3} + k_{i,4} - L_{i,1})$$

$$B_{i,2} = \frac{k_{i,1}}{\alpha_{i,2} - \alpha_{i,1}}(L_{i,2} - k_{i,3} - k_{i,4}) \qquad (5.8)$$

and $k_{i,1}$-$k_{i,4}$ are the rate constants of the FDG model for grey matter (i=1) or white matter (i=2). Equation 5.8 can be discretized and expressed in Z domain using the following rational system transfer function,

$$Fi(z^{-1}) = \frac{Ni(z^{-1})}{Di(z^{-1})} \qquad i = 1,2 \qquad (5.9)$$

where $Ni(z^{-1})$ and $Di(z^{-1})$ are polynomials in z^{-1} of order Ni and Di, respectively. They are related to the $L_{i,1}$, $L_{i,2}$, $B_{i,1}$ and $B_{i,2}$ as follows:

$$N_i(z^{-1}) = (A_{i,1} + A_{i,2}) + (A_{i,1}e^{-\lambda_{i,2}} + A_{i,2}e^{-\lambda_{i,1}})z^{-1} \qquad (5.10)$$

$$D_i(z^{-1}) = (1 - e^{-\lambda_{i,1}}z^{-1})(1 - e^{-\lambda_{i,2}}z^{-1}) \qquad (5.11)$$

The roots of $Ni(z^{-1})$ and $Di(z^{-1})$ may be inside and/or outside the unit circle. It is also assumed that the transfer functions of FDG models have no common poles and zeros.

The re-sampled TTACs are sent to a two-channel adaptive system shown in Figure 5-6. The channel transfer functions are finite order polynomials $Wi(z^{-1})$ with order Wi. That is, the adaptive channels are FIR, with

$$Wi(z^{-1}) = w_{i,o} + w_{i,1}z^{-1} + \dots + w_{i,Wi}z^{-Wi} \qquad i = 1,2 \qquad (5.12)$$
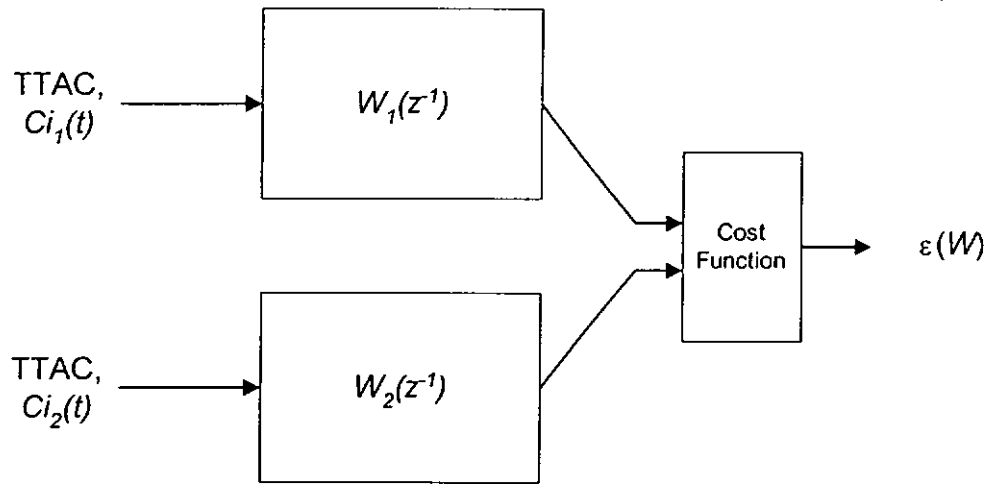
Figure 5-6 Multi-channel adaptive system.

The polynomial coefficients $w_{i,k}$ are assumed to be adaptable via some algorithms. We can also express the polynomial coefficients in vector form as follows:

$$Wi(z^{-1}) = \left[w_{i,0}, w_{i,1}, \ldots, w_{i,Wi} \right]^T \text{ and } W = \left[W_1^T, W_2^T \right]^T \tag{5.13}$$

Denotes $Xi(t)$ as the re-sampled TTACs, such that,

$$Xi(t) = \left[x_i(t), x_i(t-1), \ldots, x_i(t-Wi) \right]^T \text{ and } X(t) = \left[X_1^T(t), X_2^T(t) \right]^T \tag{5.14}$$

We define the error signal, $e(t)$, as:

$$e(t) = W^T X(t) \tag{5.15}$$

and the mean-squared-error, $\varepsilon(W)$, as

$$\varepsilon(W) = \sum_{t=0}^{\tau} |e(t)|^2 \tag{5.16}$$

where τ is the length of time interval. Assuming that the observation signals are noise free, there is a simple relationship between the roots of the unknown FDG transfer functions and the root of the adaptive channels. Assuming that the adaptive channel orders are chosen such that,

$$W_1 = N_2 + D_1 \text{ and } W_2 = N_1 + D_2 \tag{5.17}$$

then, the unique family of solutions for $W_1(z^{-1})$ and $W_2(z^{-1})$ that minimize $\varepsilon(W)$ is given by

$$W_1(z^{-1}) = \alpha N_2(z^{-1}) D_1(z^{-1}) \text{ and } W_2(z^{-1}) = -\alpha N_1(z^{-1}) D_2(z^{-1}) \tag{5.18}$$

where α is an arbitrary constant. With the above family of solutions, we have $\varepsilon(W)=0$. Or in other words, if some W can be found for which $\varepsilon(W) = 0$, then the set of $Ni(z^{-1})$ and $Di(z^{-1})$ will be the solutions and can be obtained by factoring $W_1(z^{-1})$ and $W_2(z^{-1})$. Finally, the rate constants, $k_{i,1}$-$k_{i,4}$, of the FDG model can be obtained by equation (5.8), (5.10) and (5.11).

To calculate the family of Wi that satisfies $\varepsilon(W)=0$, we make use of an eigen-vector decomposition approach similar to that in [113]. More specifically, we calculate $W_1(z^{-1})$ and $W_2(z^{-1})$ as follows:

1. Based on the re-sampled TTACs, i.e. $X(t)$, we produce a data matrix, A_x, as follows:

$$A_x = \left[X^T(\Gamma), X^T(\Gamma - 1), \ldots, X^T(1) \right]^T \tag{5.19}$$

where Γ is the observation interval. Hence,

$$\varepsilon(W) = \sum_{t=0}^{\tau} |e(t)|^2 = \sum_{t=0}^{\tau} |W^T X(t)|^2 = A_x W \tag{5.20}$$

2. Our objective is to determine W such that $\varepsilon(W) = 0$. Or equivalently, we try to solve W in the following homogeneous equation

$$A_x W = 0 \tag{5.21}$$

3. For noisy data, we are interested in the least square solution. That is, we define the sample correlation matrix, R_x, as $R_x = A_x^T A_x$ and solve W in the following equation:

$$R_x W = 0 \tag{5.22}$$

By performing eigen-vector decomposition to R_x, we obtain a set of eigen-vectors and eigen-values. However, we know that

$$W \cong q \tag{5.23}$$

where q is the eigen-vector corresponding to the smallest eigen-values of Rx.

4. Partition q into sub-vectors q_1 and q_2 and obtain the channel transfer function Q_1 and Q_2. The set of transfer function thus obtained by Q_1 and Q_2 provides a basis for the solutions for $W_{1,blind}$ and $W_{2,blind}$.

Lastly, we estimate the parameters by minimizing the following cost function using nonlinear least square curve fitting:

$$\phi(k_{i,1}, k_{i,2}, k_{i,3}, k_{i,4}) = \left| [\hat{W}_1, \hat{W}_2] - W_{1,blind}, W_{2,blind} \right|^2 \tag{5.24}$$

where $\hat{W}_i$ are the adaptive channels evaluated from the estimated parameters $k_{i,1}$-$k_{i,4}$ using (5.18) and $W_{i,blind}$ are the adaptive channels evaluated from the observable TTACs using blind deconvolution.

In summary, the proposed approach can be stated as follows: first, the wavelet denoising is applied to filter the noise in the projections. The denoised projections are then reconstructed using the filtered back projection algorithm. From the reconstructed dynamic images, two TTACs are then extracted from ROIs, e.g. one from the grey matter and the other from the white matter. The two TTACs are then re-sampled to the required rate using interpolation. Based on these two curves, the blind deconvolution technique is applied to estimate the parameters of interest, $k_{i,1}$-$k_{i,4}$.

5.3 Simulation Method

To validate the present method, we carried out a Monte Carlo simulation study. In our simulation, we generated the PTAC numerically using the input function model described in Section 2.6.2. We assume that the time delay of the input function model is equal to zero. The mathematical expression of this simplified input function model, $Cp^{model}(t)$, is given as follows:

$$Cp^{model}(t) = \begin{cases} (A_1 t - A_2 - A_3)e^{\lambda_1 t} + A_2 e^{\lambda_2 t} + A_3 e^{\lambda_3 t} & t > \tau \\ 0 & t \leq \tau \end{cases} \tag{5.25}$$

where, as previously published [72]:

$A_1 = 851.1, A_2 = 21.88, A_3 = 20.81$ [$\mu Ci/ml$]

$\lambda_1 = -4.134, \lambda_2 = -0.1191, \lambda_3 = -0.0104$ [$1/min$]

The transport rate constants, k_1-k_4, for the FDG models are obtained from [64] and are listed in Table 5-1. The derived parameter, K, which is proportional to the metabolic rate of glucose and is equal to $k_1*k_3/(k_2+k_3)$, is also shown in Table

5-1. It is used as a reference for the comparison of the performance of different methods.

	K_1	k_2	k_3	k_4	K
Region 1	0.1200	0.1070	0.0440	0.0059	0.0350
Region 2	0.0740	0.1030	0.0290	0.0038	0.0163

Table 5-1 The transport rate constants, k_1-k_4, for the FDG models. The derived parameter, K, which equals to $k_1 * k_3/(k_2 + k_3)$ and is proportional to the metabolic rate for glucose, is also shown.

Based on the simulated PTAC and the FDG model, TTACs (6×0.167s, 4×0.5s, 1×2min, 11×5min) were generated by convolving the PTAC with the FDG models. These curves are reformatted into dynamic images using the Hoffman brain phantom. The phantom is partitioned into two regions corresponding to the two different kinetics which are typical of brain white matter and grey matter, respectively. Sinogram data are generated with 64 projections, each with 64 bins, assuming 360° rotation. The simulation did not include attenuation, scatter or distance dependent detector response. The projection data were scaled to count densities which might be expected for dynamic PET imaging (with 2k counts/sec in the last frame-interval). Poisson noise was added to the projection data.

Three methods for analysis were compared:

(1) The noisy projection data are reconstructed using filtered back projection (FBP) algorithm. TTACs are extracted from the ROIs. k_1-k_4 are then estimated using non-linear least square, assuming that the PTAC are measured. This simulation describes the traditional approach for dynamic PET studies.

(2) The noisy projection data are reconstructed using FBP. TTACs are extracted from the ROIs and are re-sampled using linear interpolation. The blind deconvolution technique is then applied to estimate k_1-k_4.

(3) Wavelet denoising are applied to the noisy projection data, followed by the FBP to reconstruct the dynamic images. TTACs are extracted from the ROIs

and are re-sampled using linear interpolation. Finally, k_1-k_4 are estimated using the blind deconvolution technique, i.e. without PTAC.

For each method, k_1-k_4 were estimated and the parameter, K, was evaluated. The simulations were carried out for one hundred independent realizations to obtain average performances for each method. The percentage errors compared to the true parameters and the coefficient of variation (CV) of the estimated k_1-k_4 and K's were determined.

5.4 Simulation Results

Figure 5-7a and 5-7d show the original sinogram and the image reconstructed from the projections using the filtered back projection algorithm. The sinogram is then contaminated with Poisson noise. Figure 5-7b and 5-7e show the noisy sinogram and the reconstructed image. The noisy sinogram is then denoised using the wavelet denoising approach. Figure 5-7c and 5-7f show the denoised sinogram and the reconstructed image. They demonstrate that the reconstructed image based on the denoised sinogram provides qualitatively improved reconstruction.
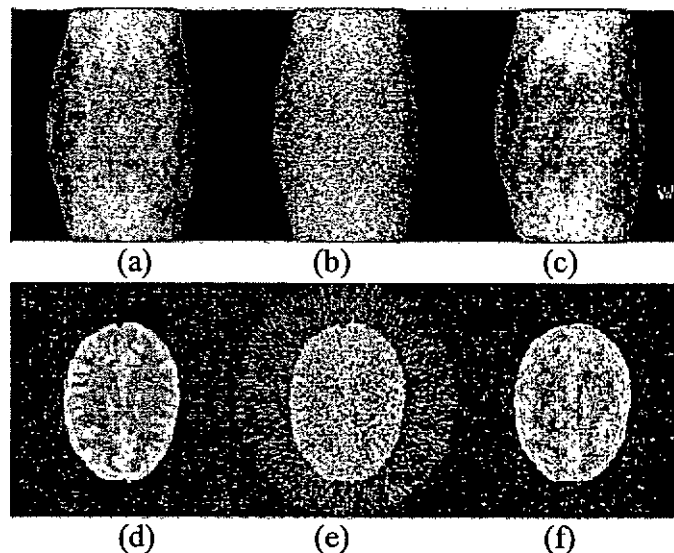
Figure 5-7 The simulated sinogram and reconstructed images. (a) and (d) show the original sinogram and the image reconstructed from the projections using the filtered back projection algorithm. (b) and (e) show the noisy sinogram, contaminated with Poisson noise, and the corresponding reconstructed image. (c) and (f) show the denoised sinogram, using wavelet denoising, and the corresponding reconstructed image.

Table 5-2 shows the percentage error and CV of the estimated k_1-k_4 and K using the three different methods described in the simulation section. The first column indicates the three methods being compared. Method 1 (the Traditional Method) is the approach which simulates the traditional way of performing dynamic PET studies, i.e. using nonlinear least square to fit the TTACs to a pre-assumed kinetic model, assuming that PTAC is measured. Method 2 (Blind deconvolution without denoising) is the method that blind deconvolution is applied without wavelet denoising. Method 3 (Blind deconvolution with denoising) is the method that wavelet denoising is applied to filter the noise in projections. The denoised projections are then reconstructed using the FBP and the blind deconvolution algorithm is applied to estimate the parameters. The second to sixth columns are the k_1-k_4 and K for region 1 while the seventh to eleventh columns are the k_1-k_4 and K for region 2. As can be seen, when blind deconvolution is applied without wavelet denoising, the percentage error of the result is significant (Method 2). This is because the calculation of the eigen-vector is sensitive to noise, in particular, the colored noise. When colored noise exists, the eigen-vector calculated based on the sample correlation matrix will be biased. As a result, the parameters estimated will deteriorate. However, when wavelet denoising is applied to filter the noise in the projections, followed by the blind deconvolution, the result is significantly improved (Method 3). It is interesting to note that the percentage error of the estimated k_1 is lower than the other methods. This is because of the fact that two regions are analyzed simultaneously in the proposed blind deconvolution method. The percentage error of the estimated k_2, k_3 and K are comparable to that of invasive method (Method 1). Although the percentage error of the estimated k_4 is still much larger because of its small value, its existence does not very much contribute to the calculation of K. Hence the error incurred is not significant to the final result as a whole. For the CV, the proposed method is always lower than the other methods.

Error (%)	Region 1					Region 2				
	k_1	k_2	k_3	k_4	K	k_1	k_2	k_3	k_4	K
Traditional method	0.62	-1.26	3.41	12.33	2.78	6.66	0.67	10.06	36.72	12.57
Blind Deconvolution without denoising	-0.03	-43.77	48.57	361.98	90.99	0.03	45.91	73.67	562.01	12.23
Blind deconvolution with denoising	0.00	-3.35	4.93	36.74	6.02	0.00	4.23	7.48	57.04	2.32
CV (%)	k_1	k_2	k_3	k_4	K	k_1	k_2	k_3	k_4	K
Traditional method	2.35	9.80	23.47	82.35	11.15	4.35	11.00	27.74	102.65	13.87
Blind Deconvolution without denoising	0.02	62.69	25.75	61.73	41.83	0.02	24.99	33.42	66.89	7.34
Blind deconvolution with denoising	0.00	4.43	4.63	26.48	6.22	0.00	4.37	6.86	35.80	2.00

Table 5-2 The Error (in percentage) and CV (in percentage) of the estimated k_1-k_4 and K for the three different methods. The first column indicated the three methods compared. The second to sixth columns are the k_1-k_4 and K for region 1. The seventh to eleventh columns are the k_1-k_4 and K for region 2.

5.5 Summary

In this chapter, we proposed a new approach for estimating physiological parameters, based on the measurement obtained from dynamic PET studies. The proposed approach obviates the requirement of blood sampling. It comprises two major steps: wavelet transform is used to filter the noise in projections, and a blind deconvolution algorithm which is based on eigen-vector decomposition is used for parameter estimation. We have performed a Monte Carlo simulation to investigate the performance of the proposed approach. The results demonstrate that the approach can estimate the physiological parameters with an accuracy comparable to that of invasive approach which requires the whole PTAC to be measured. Since the proposed approach obviates the taking of blood samples, it

is non-invasive, simple and it minimizes the possibilities of radiation exposure to clinical personnel and the possibility of spread of infectious diseases. Furthermore, although we applied the proposed technique specifically to the tomographic studies based on FDG model, the proposed technique can also be applied to other tracer kinetic model. Therefore, the proposed technique has widespread clinical appeal.

Chapter 6 Conclusion and Future Extension

6.1 Conclusion of present research

In this work, several areas of performing functional imaging with Positron Emission Tomography (PET) or Single Photon Emission Computer Tomography (SPECT) are investigated. They are : (i) reduction of capital cost associated with PET studies; (ii) the sampling requirement of dynamic studies; and (iii) quantification of physiological processes for dynamic studies obviating the blood sampling procedure.

(i) Reduction of capital cost associated with PET studies

Functional imaging studies require reliable measurement of the time course of tracer in tissue. This can be achieved using stationary detectors as in the ring geometry most commonly available for PET and similarly designed SPECT systems based on detector rings. These systems, however, are usually of very high cost and make them not as popular as the other imaging modalities. Therefore, performing functional system using rotating detectors system arose much interests and its possibility has been demonstrated by a number of research groups. However, the rotating detectors systems have the problem that only partial projection data can be recorded at a time, resulting in an acquisition of inconsistent set of projection for each image reconstruction. The corresponding reconstructed images will suffer from artifacts and affect the accuracy of subsequent parameter estimation.

Therefore, in Chapter 3, we have proposed a novel approach for reconstruction of dynamic images and determination of tracer kinetic parameters using data acquired from a rotating detector system. Fundamental to the approach is the use of the integrated activity over each image acquisition interval, rather than normal assumptions that measurements represent estimates of instantaneous mid-interval values. Based on this premise, an interpolation method is applied to the projection space to better approximate the total counts for each acquisition

interval, closer to that would be obtained for a ring detector system. The resultant interpolated projection are reconstructed into dynamic images and an integral-based model-fitting algorithm is then applied to estimate the kinetic parameters. The reliability of the proposed method has been tested by computer simulations over a range of count densities. The results demonstrate that the proposed approach provides artifact-free images and parameter estimates comparable to those obtained with a ring detector system, as is typical of conventional PET. The technique can potentially be applied to data acquired using systems such as single or multi-detector SPECT, coincidence detection or low-cost PET systems which involve detector rotation rather than a stationary ring of detectors. The techniques therefore have widespread clinical appeal.

(ii) The sampling requirement of dynamic studies

Although there have been some research work on the design of PET image frame sampling schedules to increase the quantitative accuracy, little attention has been paid to systematically investigate the total acquisition duration. For dynamic SPECT studies, the clinical practicality of the total acquisition duration is a particularly important consideration. The slow kinetics of typical SPECT tracers may require unrealistically long total acquisition times to obtain reliable estimation of the slower rate constants.

Therefore, in Chapter 4, we systematically investigated the reliability of parameter estimation as a function of acquisition time and applied the optimum sampling schedule (OSS) technique to determine optimized, practical sampling schedules for dynamic Tl-201 SPECT. We found that 1) blood flow related parameter, K_1, can be estimated with a relatively short study duration of 30 minutes, while estimation of volume of distribution (Vd) requires at least 90-120 minutes to achieve acceptable precision. 2) Dividing the scanning into early and delayed sessions allows accurate estimation of Vd. It avoids the need for prolonged continuous dynamic acquisition (>90 minutes). Both K_1 and Vd can thus be determined with a clinically practical sampling schedule. 3) OSS can provide reliable estimates of both K_1 and Vd, comparable to that of full dynamic

sampling which often requires to record far more images. This study also highlights that careful consideration needs to be given to total acquisition time to obtain reliable estimates of all parameters of interest, particularly for typical SPECT tracers with slow kinetic components. The method for determining optimum sampling schedule and total acquisition time applied here to Tl-201 should also be applicable to other SPECT tracers.

(iii) Quantification of physiological processes for dynamic studies without the blood sampling procedure

One of the inherent components involved in functional studies is the measurement of tracer concentration in blood plasma, i.e. plasma time activity curve (PTAC). PTAC acts as the input function for the tracer kinetic model. The measurement of PTAC are usually invasive, time consuming and tedious. The measurement process also exposes the patient and clinical personnel to the danger of fatal blood infection. Therefore, it is desirable to have alternative method for performing functional studies such that the blood sampling procedure can be eliminated.

In that light, in Chapter 5, we proposed a new approach for estimating physiological parameters from dynamic studies, obviating the requirement of blood sampling. The proposed approach involves the use of wavelet transform to filter the noise in projections, and an eigen-vector based blind deconvolution procedure for parameter estimation. The proposed technique is evaluated using a Monte Carlo simulation. The results demonstrate that the approach can estimate the physiological parameters with an accuracy comparable to that of invasive approach which requires the whole PTAC to be measured. The proposed approach is simple and can be easily handled computationally. While in this study, we applied the proposed technique specifically to the tomographic studies based on FDG model, the technique is also applicable to other tracer kinetic model.

On the whole, we have developed, in this research work, different approaches to minimize the inconvenience of performing functional imaging using emission computed tomography. We hope our achievements can help the technique to be more extensively used in both clinical and academic research environments.

6.2 Future Extension

There are several areas that further research work can be performed. First of all, we believe that further investigation on the proposed approach for performing functional studies using rotating detector systems would be promising. We have carried out a simulation to investigate the performance of the proposed approach. The simulated detection geometry closely resembles to a rotating SPECT system. The applications of the proposed approach to other systems such as coincidence detection system and low-cost PET system which involve detector. rotation may require further work and simulations employing such detection geometry may need to be performed as well.

Besides, we have shown in Chapter 3 that the error introduced in the interpolation step can be corrected by using a normalization method. Indeed, there are alternative approaches to solve this problem. One possible solution is to applied a constraint in the turning value of the parabola so that the best-fit parabola would not deviate significantly from the true curve. It will be fruitful to investigate the alternative strategies.

Further research work on the methodology for optimizing the sampling schedule used in dynamic SPECT studies may be required for practical applications. We have demonstrated that accurate estimation of K_1 and Vd can be obtained by employing a two-session scanning. The next step would be applying the technique to clinical studies for further validation. One practical issue involved in performing a dynamic study using the two-session scanning is the alignment of the dynamic images obtained from these two sessions. The object movement which could lead to errors in parameter estimates or artifacts in functional images is another problem that will be encountered. A possible solution to these

problems may be some on-line object movement correction. In addition, for myocardial studies, the activity obtained from myocardial tissue is only an approximation which represents the average activity among a region of pixels because of the beating of heart. One possible solution for this problem is to employ gated study. All these issues need to be further investigated.

One the other hand, the blind deconvolution technique developed in Chapter 5 can also be further improved. The eigen-vector based approach employed in the proposed method is sensitive to noise, especially color noise. Indeed, there are alternative strategies to perform blind deconvolution. One possible solution is the subspace methods [120]. We believe that further investigation on this aspect is promising.

Besides, in our simulations, we have only added simulated measurement noise which is derived based on real clinical situation. Other physical constraints on the accuracy of measurement such as attenuation, scatter or, in the case of PET, random coincidences, are not included. Simplifications in the overall simulations were considered necessary to isolate the influences under concerned. Hence, the performance of the proposed algorithms when other constraints are included needs further investigation.

Lastly, the validation of the proposed algorithms with real clinical data is promising. With clinical data, the actual applicability and performance of the proposed approaches can be directly demonstrated.

Chapter 7 Bibliography

[1] F. C. Flack, "Recent advances in medical functional imaging", *Engineering Science and Education Journal*, Vol. 3, p. 213-222, 1994.

[2] E. R. Wrenn, M. L. Good, P. Handler, "The use of positron emitting radioisotopes for the localization of brain tumors", *Science*, Vol. 113, p. 525-527, 1951.

[3] W. H. Sweet, "Uses of nuclear disintegration in the diagnosis and treatment of brain tumors", *N. Engl. J. Med.*, Vol. 245, p. 875, 1951.

[4] G. L. Brownell, W. H. Sweet, "Localization of brain tumors with positron emitters", *Nucleonics*, Vol. 11, p. 40, 1953.

[5] C. A. Burham, G. L. Brownell, "A multi-crystal positron camera", *IEEE Trans. Nuclear Sci.*, Vol. 19, p. 201-205, 1972.

[6] H. O. Anger, D. J. Rosenthal, "Scintillation camera and positron camera", in *Medical Radioisotope Scanning*, International Atomic Energy Agency - Vienna, p. 59-68, 1959.

[7] S. Rankowitz, J. S. Robertson, W. A. Higinbotham, A. M. Neil, "Positron scanner for locating brain tumors", *IRE Int. Conv. Rec.*, Vol. 9, p. 49-59, 1962.

[8] J. S. Robertson, A. M. Neil, "Use of a digital computer in the development of a positron canning procedure" *Proc. 4th IBM Medical Symposium*, p. 77-103, 1962.

[9] D. E. Kuhl, R. Q. Edwards, "Image separation radioisotope scanning", *Radiology*, Vol. 30, p. 653-661, 1963.

[10] H. O. Anger, "Multiple plane tomographic scanner", in *Tomographic Imaging in Nuclear Medicine*, Freeman G. S. ed., Society of Nuclear Medicine - New York, p. 2-18, 1973.

[11] G. Muehllehner, R. A. Wetzel, "Section imaging by computer calculation", *J. Nucl. Med.*, Vol. 12, p. 79-87, 1971.

[12] A. E. Todd-Pokropek, "The formation and display of section scans", *Proceedings of the Symposium of the American Congress of Radiology* held at Amsterdam, Excerpta Medica, p. 545-556, 1972.

[13] A. R. Bowley, C. G. Taylor, D. A. Causer, D. C. Barber, W. L. Keyes, P. E. Undrill, J . R. Corfield, J. R. Mallard, "A radioisotope scanner for rectilinear, arc, transverse section and longitudinal section scanning (ASS - The Aberdeen Section Scanner)", *Br. J. Radiol.*, Vol. 46, p. 262-271, 1973.

[14] E. Tanaka, "Multi-crystal section imaging device and its data processing", *Proceedings of the 13th Congress of Radiology, Madrid* held at Amsterdam, Excerpta Medica, p. 81-85, 1973.

[15] J. T. Littleton, C. L. Rumbaugh, F. S. Winters, "Polydirectional body section roentgenography: A new diagnostic approach", *Am. J. Roentgenol, Radium Ther, Nucl, Med.*, Vol. 29, p. 1179-1131, 1963.

[16] D. E. Kuhl, R. Q. Edwards, A. R. Ricci, M. Revicih, "Quantitative section scanning using orhtogonal tangent correction", *J Nucl. Med.*, Vol. 14, p. 196-200, 1973.

[17] D. E. Kuhl, R. Q. Edwards, A. R. Ricci, R. J. Yacob, T. J. Mich, A. Alavi, "The Mark IV system for radionuclide computed tomography of the brain", *Radiology*, Vol. 121, p. 405-413, 1976.

[18] T. F. Budinger, G. T. Gullberg, "Three-dimensional reconstruction in nuclear medicine by iterative least-squares and Fourier transform techniques imaging", *IEEE Trans. Nucl. Sci.*, Vol. 21, p. 2-20, 1974.

[19] D. B. Kay, J. W. Keyes, "First order corrections for absorption and resolution compensation in radionuclide Fourier tomography", *J. Nucl. Med.*, Vol. 16, p. 540-545, 1975.

[20] M. E. Phelps, E. J. Hoffman, N. A. Mullani, M. M. Ter-Pogossian, "Application of annihilation coincidence detection to transaxial reconstruction tomography", *J. Nucl. Med.*, Vol. 16, p. 210-223, 1975.

[21] M. E. Phelps, E. J. Hoffman, N. A. Mullani, M. M. Ter-Pogossian, " Transaxial emission reconstruction tomography: Coincidence detection of positron-emitting radionuclides", in *Non-Invasice Brain Imaging, Radionuclides and Computed Tomography*, H. DeBlanc, J. A. Sorenson, eds., Society of Nuclear Medicine - New York, p. 87-109, 1975.

[22] E. J. Hoffman, M. E. Phelps, N. A. Mullani, C. S. Higgins, M. M. Ter-Pogossian, "Design and performance characteristics of a whole body transaxial tomography", *J. Nucl. Med.*, Vol. 17, p. 493-503, 1976.

[23] M. E. Phelps, E. J. Hoffman, R. E. Coleman, M. J. Welch, M. E. Raichle, E. S. Weiss, B. E. Sobel, M. M. Ter-Pogossian, "Tomographic images of blood pool and perfusion in brain and heart", *J. Nucl. Med.*, Vol. 17, p. 603-612, 1976.

[24] M. E. Phelps, E. J. Hoffman, N. A. Mullani, C. S. Higgins, M. M. Ter-Pogossian, "Design Considerations for a positron emission transaxial tomography (PET III)", *IEEE Trans. Nucl. Sci.*, Vol. 23, p. 516-522, 1976.

[25] M. E. Phelps, E. J. Hoffman, S. C. Huang, D. E. Kuhl, "ECAT: A new computerized tomographic imaging system for positron emitting radiopharmaceuticals", *J. Nucl. Med.*, Vol. 19, p. 635-647, 1978.

[26] R. A. Brooks, G. DiChiro, "Principles of computer assisted tomography (CAT) in radiographic and radioisotopic imaging", *Phys. Med. Biol.*, Vol. 21, p. 689-732, 1976.

[27] T. F. Bindinger, S. E. Derenzo, G. T. Gullberg, W. L. Greenberg, R. H. Huesman, "Emission computed axial tomography with single photon and positron annihilation photon emitters", *J. Comput. Assist. Tomogr.*, Vol. 1, p. 131-145, 1977.

[28] M. M. Ter-Pogossian, M. E. Phelps, G. L. Brownell, J. R. Jr Cox, D. O. Davis, R. G. Evans, "Reconstruction Tomography in Diagnostic Radiology an Nuclear Medicine", University Park Press - Baltimore, 1977.

[29] M. M. Ter-Pogossian, N. A. Mullani, D. C. Ficke, J. Markham, D. L. Snyder, "Photon time-of-flight-assisted positron emission tomography", *J. Comput. Assis. Tomogr.*, Vol. 5, p. 227-229, 1981.

[30] H. Iida, Y. Tamura, Y. Narita, S. Eberl, Y. Ono, "Use of Tl-201 and SPECT for quantitative assessment of regional myocardial blood flow," *J Nucl Med*, Vol. 38, p. 165p, 1997.

[31] D. W. Townsend, M. Wensveen, L. G. Byars, A. Geissbuhler, H. J. Tochon-Danguy, A. Christian, M. Defrise, D. L. Bailey, S. Grootoonk, A. Donath,

"A rotating PET scanner using BGO block detectors: design, performance and applications," *J. Nucl. Med.*, Vol. 34, p. 1367-1376, 1993.

[32] J. S. Karp, G. Muehllehner, D. A. Mankoff, C. E. Ordonez, J. M. Ollinger, M. E. Daube-Witherspoon, A. T. Haigh, D. J. Beerbohm, "Continuous-slice PENN-PET: a positron tomograph with volume imaging capability," *J. Nucl. Med.*, Vol. 31, p. 617-627, 1990.

[33] P. Nellemann, H. Hines, W. Braymer, G. Muehllehner, M. Geagan, "Performance characteristics of a dual head SPECT scanner with PET capability," *IEEE Nuclear Science Symposium and Medical Imaging Conference Record*, Vol. 3, p. 1751-1755, 1995.

[34] A. M. Smith, G. T. Gullberg, P. E. Christian, F. L. Datz, "Kinetic modeling of teboroxime using dynamic SPECT imaging of a canine model," *J. Nucl. Med.*, Vol. 35, p. 484-495, 1994.

[35] H. Iida, H. Ito, M. Munaka, P. M. Bloomfield, S. Higano, M. Murakami, A. Inugami, S. Eberl, Y. Aizawa, I. Kanno, K. Uemura, "A clinical method to quantitative CBF using a rotating gamma camera and I-123 amphetamine (IMP) with one blood sampling," *Eur. J. Nucl. Med.*, Vol. 21, p. 1072-1084, 1994.

[36] H. Iida, H. Ito, M. Nakazawa, J. Hatazawa, H. Nishimura, Y. Onishi, K. Uemura, "Quantitative mapping of regional cerebral blood flow using [123I] N-isopropyl-p-iodoamphetamine (IMP) and single photon emission tomography," *J. Nucl. Med.*, Vol. 35, p. 2019-2030, 1994.

[37] M. Ichise, J. R. Ballinger, H. Golan, D. Vines, A. Luong, S. Tsai, H. F. Kung, "Noninvasive Quantification of Dopamine D2 Receptors with Iodine-123-IBF SPECT," *J. Nucl. Med.*, Vol. 37, p.513-520, 1996.

[38] K. Tan, B. F. Hutton, D. Feng, "Assessment of Errors Due to Changing Activity During Kinetic SPECT Acquisition," *Proceedings, 17th Annual International Conference IEEE Engineering in Medicine and Biology Society*, [ISBN 0-7803-2478-1 (CDROM)], USA, Sept., 1995.

[39] J. M. Links, T. L. Frank, L. C. Becker, "Effect of differential tracer washout during SPECT acquisition," *J. Nucl. Med.*, Vol. 32, p. 2253-2257, 1991.

[40] J. E. Juni, "SPECT of rapidly cleared tracers: imaging a Cheshire cat," *J. Nucl. Med.*, Vol. 33, p. 1206-1208, 1992.

[41] M. A. Limber, M. N. Limber, A. Celler, J. S. Barney, J. M. Borwein, "Direct Reconstruction of Functional Parameters for Dynamic SPECT," *IEEE Trans. Nucl. Sci.*, Vol. 42, p. 1249-1255, 1995.

[42] G. L. Zeng, G. T. Gullberg, R. H. Huesman, "Using linear time-invariant system theory to estimate kinetic parameters directly from projection measurements," *IEEE Trans. Nucl. Sci.*, Vol. 42, p. 2339-2346, 1995.

[43] A. Hawkins, M. E. Phelps, and S. C. Huang, "Effects of temporal sampling, glucose metabolic rates, and disruptions of the blood-brain barrier on the FDG model with and without a vascular compartment: Studies in human brain tumors with PET," *J Cereb Blood Flow Metab*, Vol. 6, p. 170-183, 1986.

[44] B. M. Mazoyer, R. H. Huesman, T. F. Budinger, and B. L. Knittel, "Dynamic PET Data Analysis," *J Comp Assist Tomogr*, Vol. 10, p. 645-653, 1986.

[45] J. Delforge, A. Syrota, and B. M. Mazoyer, "Experimental Design Optimisation: Theory and Application to Estimation of Receptor Model Parameters Using Dynamic Positron Emission Tomography," *Phys Med Biol*, Vol. 34, p. 419-435, 1989.

[46] S. Jovkar, A. C. Evans, M. Diksic, H. Nakai, and Y. L. Yamamoto, "Minimisation of Parameter Estimation Errors in Dynamic PET: Choice of Scanning Schedules," *Phys Med Biol*, Vol. 34, p. 895-908, 1989.

[47] X. Li and D. Feng, "Towards the reduction of dynamic image data in PET studies," *Computer Methods and Programs in Biomed*, Vol. 53, p. 71-80, 1997.

[48] S. Eberl, A. R. Analyat, R. R. Fulton, P. K. Hooper, M. J. Fulham, "Evaluation of Two Population-based Input Functions for Quantitative Neurologic FDG PET Studies." *Eur. J. Nucl. Med.*, Vol. 24, p. 299-304, 1997.

[49] C. Burger, A. Buck, "Tracer kinetic modelling of receptor data with mathematical metabolic correction." *Eur. J. Nucl. Med.*, Vol. 23, p. 539-454, 1996.

[50] R. E. Carson, Y. Yan, R. Sharger, "Absolute Cerebral Blood Flow with [^{15}O]Water and PET - Determination Without a Measured Input Function." *Quantification of Brain Function using PET*, Academic Press, p. 185-190, 1996.

[51] H. Watabe, M. Itoh, V. J. Cunningham, A. A. Lammertsma, P. M. Bloomfield, M. Mejia, T. Fujiwara, A. K. P. Jones, T. Jones, T. Nakamura, "Nonivasive Quantification of rCBF Using Positron Emission Tomography." *Quantification of Brain Function using PET*, Academic Press, p. 191-195, 1996.

[52] E. J. Hoffman, M. E. Phelps, "Positron Emission Tomography: Principles and Quantitation", in *Positron Emission Tomography and Autoradiography: Principles and Applications for the Brain and Heart*, M. E. Phelps, J. Mazziotta, H. Schelbert, eds., Raven Press-New York, p. 237-286, 1986.

[53] M. S. Rosenthal, J. Cullom, W. Hawkins, S. C. Moore, B. M. W. Tsui, M. Yester, "Quantitative SPECT Imaging: A Review and Recommendations by the Focus Committee of the Society of Nuclear Medicine Computer and Instrumentation Council", *J. of Nucl. Med.*, Vol. 36, p. 1489-1513, 1995.

[54] R. N. Bracewell, A. C. Riddle, "Inversion of fan-beam scans in radio astronomy", *Astrophysics J.*, Vol. 150, p. 427-434, 1967.

[55] G. N. Ramachandran, A. V. Lakshminarayanan, "Three-dimensional reconstruction from radiograph and electron micrographs: application of convolutions instead of Fourier transform", *Proc. Natl. Acad. Sci U.S.A.*, Vol. 67, p. 643-650, 1971.

[56] E. L. Kramer, J. J. Sanger, "SPECT Reconstruction Techniques" in *Clinical SPECT Imaging*, Raven Press - New York, p. 43-68, 1995.

[57] A. J. Rockmore, A. Macovski, "A maximum likelihood approach to emission image reconstruction from projection", *IEEE Trans. Nucl. Sci.*, Vol. 23, p. 1428-1432, 1976.

[58] L. A. Shepp, Y. Vardi, " Maximum-likelihood reconstruction for emission tomography", *IEEE Trans. Med. Imag.*, Vol. 1, p. 113-122, 1982.

[59] K. Lange, R. Carson, "EM reconstruction algorithm for emission and transmission tomography", *J. Comput. Assist. Tomogr.*, Vol. 8, p. 305-316, 1984.

[60] L. Kaufman, "Implementing and accelerating the EM algorithm for Positron Emission Tomography", *IEEE Trans. Med. Imag.*, Vol. 6, p. 37-51, 1987.

[61] H. M. Hudson, R. S. Larkin, "Accelerated Image Reconstruction Using Ordered Subsets of Projection Data", *IEEE Trans. Med. Imag.*, Vol. 13, p. 601-609, 1994.

[62] E. R. Carson, C. Cobelli, L. Finkelstein, *The Mathematical Modeling of Metablic and Endocrine Systems*, Wiely - New York, 1983.

[63] M. Berman, R. Schoenfeld, "Invariants in experimental data on linear kinetics and the formulation of models", *J. Appl. Physiol.*, Vol. 27, p. 1361-1370, 1956.

[64] S.C. Huang, M.E. Phelps, E.J. Hoffman, K. Sideris, C.J. Selin and D.E. Kuhl, "Noninvasive determination of local cerebral metabolic rate of glucose in man," *Am. J. Physiol.*, Vol. 238, p. E69-E82, 1980.

[65] L. Sokoloff, M. Reivich, C. Kennedy, M. H. DesRosiers, C. S. Patlak, K. D. Kakurada, M. Sinohara, "The [^{14}C] deoxyglucose method for the measurement of local cerebral glucose utilization: Theory, procedure and normal values in the conscious and anesthethized albino rat." *J. Neurochem.*, Vol. 28, p. 897-916, 1977.

[66] M. E. Phelps, S. C. Huang, E. J. Hoffman, C. Selin, L. Sokoloff, D. E. Kuhl, "Tomographic measurement of local cerebral glucose metabolic rate in humans with (F-18)2-fluoro-2-deoxy-D-glucose: Validation of method." *Ann. Neurol,*, Vol. 6, p. 371-388, 1979.

[67] K. L. Zierler, "Equations for measuring blood flow by external monitoring of radioisotopes", *Circ. Res.*, Vol. 16, p. 309-321, 1965.

[68] R. Fletcher, *Practical Methods for Optimization*, Wiely - New York, 1980.

[69] D. W. Marquardt, "An algorithm for least squares estimation of nonlinear parameters", *SIAM J. Soc. Indust. Appl. Math.*, Vol. 2, p. 431-441, 1963.

[70] D. Feng, D. Ho, K. Chen, L. C. Wu, J. K. Wang, R. S. Liu, S. H. Yeh, "An Evaluation of the Algorithms for Determining Local Cerebral Metabolic Rates of Glucose Using Positron Emission Tomography Dynamic Data", *IEEE Trans. Med. Imag.*, Vol. 14, p. 687-710, 1995.

[71] M. E. Phelps, E. J. Hoffman, C. Selin, S. C. Huang, D. E. Kuhl, "Investigation of (F-18)2-fluoro-2-deoxyglucose for the measurement of myocardial glucose metabolism", *J. Nucl. Med.*, Vol. 19, p. 1311-1319, 1978.

[72] D. Feng, S. C. Huang, X. Wang, "Models for Computer Simulation Studies of Input Functions for Tracer Kinetic Modeling with Positron Emission Tomography", *Int. J. Biomed. Comput.*, Vol. 32, p. 95-100, 1993.

[73] D. Feng, X. Wang, H. Yan, "A computer Simulation Study on the Effects of Input Function Sampling Schedules in Tracer Kinetic Modelling with Positron Emission Tomography (PET)," *Comput. Methods Programs Biomed.*, Vol. 45, p. 175-186, 1994.

[74] D. Feng, X. Wang "A Method for Biomedical System Modeling and Physiological Parameter Estimation Using Indirectly Measured Input Functions," *Int. J. Sys. Sci.*, Vol. 26, p. 723-739, 1995.

[75] D. Feng, X. Li, S. C. Huang, "A New double Modeling Approach for Dynamic Cardiac PET Studies Using Noise and Spillover Contaminated LV Measurements," *IEEE Trans. Biomed. Eng.*, Vol. 43, p. 319-327, 1996.

[76] K. Chen, S. C. Huang, D. C. Yu, "The effects of measurement errors in the plasma radioactivity curve on parameter estimation in positron emission tomography", *Phy. Med. Biol.*, Vol. 36, p. 1183-1200, 1991.

[77] D. Feng, X. Wang, "A computer Simulation Study on the Effects of Input Function measurement noise in tracer kinetic modeling with positron emission tomography (PET)," *Comput. Bio. Med.*, Vol. 23, p. 57-68, 1993.

[78] T. F. Budinger, S. E. Derenzo, W. L. Greenberg, G. T. Gullberg, R. H. Huesman, "Quantitative potentials of dynamic emission computed tomography", *J. Nucl. Med.*, Vol. 19, p. 309-315, 1978.

[79] R. E. Carson, Y. Yan, M. E. Daube-Witherspoon, N. Freedman, S. L. Bacharach, P. Herscovitch, "An approximation formula for the variance of

PET region-of-interest values", *IEEE Trans. Med. Imag.*, Vol. 12, p. 240-250, 1993.

[80] E. M. Stokely, E. Sveinsdottir, N. A. Lassen, P. Rommer, "A single-photon dynamic computer-assisted tomograph (DCAT) for imaging brain function in multiple cross-sections," *J. Comput. Assist. Tomogr.*, Vol. 41, p. 230-240, 1980.

[81] I. Kanno, K. Uemura, Y. Miura, S. Miura, Y. Hirose, K. Koga, H. Hattori, "The Headtome: a hybrid emission tomograph for brain. Design concepts and preliminary results," *Medical Radionuclide Imaging 1980*, Vol. 1, IAEA, Vienna 1981, p. 153-164, 1980.

[82] B. L. Holman, P. A. Carvalho, R. E. Zimmerman, K. A. Johnson, S. S. Tumeh, A. P. Smith, S. Genna, "Brain perfusion SPECT using an annular single crystal camera: initial clinical experience," *J. Nucl. Med.*, Vol. 31, p. 1456-1461, 1990.

[83] B. D. Bok, A. N. Bice, M. Clausen, D. F. Wong, H. N. Wagner Jr., "Artifacts in camera based single photon emission tomography due to time activity variation", *Eur. J. Nul. Med.*, Vol. 13, p. 439-442, 1987.

[84] K. Nakajima, N. Shuke, J Taki, "A Simulation of dynamic SPECT using radio-pharmaceuticals with rapid clearance", *J. Nucl. Med.*, Vol. 33, p. 1200-1206, 1992.

[85] K. Tan, B. F. Hutton, D. Feng, "A New Approach for Parameter Estimation in SPECT Dynamics Using A Rotating Camera," *Eur. J. Nucl. Med.*, Vol. 21 [Suppl], S29, 1994.

[86] R. E. Carson, S. C. Huang, M. V. Green, "Weighted integration method for local cerebral blood flow measurements with positron emission tomography," *J. Cereb. Blood Flow Metab.*, Vol. 6, p. 245-258, 1986.

[87] K. Chen, S. C. Huang, D. Feng, "New Estimation Methods that Directly Use the Time Accumulated Counts in the Input Function in Quantitative Dynamic PET Studies," *Phys. Med. Biol.*, Vol. 39, p. 2073-2090, 1994.

[88] P. C. Chiao, W. L. Rogers, N. H. Clinthorne, J. A. Fessler, A. O. Hero, "Model-based Estimation for Dynamic Cardiac Studies using ECT," *IEEE Trans. Med. Imag.*, Vol. 13, p. 217-227, 1994.

[89] I. Kanno, A. A. Lammerstsma, J. D. Heather, J. M. Gibbs, C. G. Rhodes, J. C. Clark, T. Jones, "Measurement of Cerebral Blood Flow Using Bolus Inhalation of $C_{15}O_2$ and Positron Emission Tomography: Description of the Method and Its Comparison with the $C_{15}O_2$ Continuous Inhalation Method," *J. Cereb. Blood Flow and Metab.*, Vol. 4, p. 224-234, 1984.

[90] E. Tsui, T. F. Budinger, "Transverse Section Imaging of Mean Clearance Time," *Phys. Med. Biol.*, Vol. 23, p. 644-653, 1978.

[91] P. Herscowitch, J. Markham, M. E. Raichle, "Brain blood flow measured with intravenous O-15 water I: Theory and error analysis," *J. Nucl. Med.*, Vol. 24, p. 782-789, 1983.

[92] Z. Wang, D. Feng, "Continuous-time system modelling using the weighted-parabola-overlapping numerical integration method," *Int. J. System Sci.*, Vol. 23, p. 1361-1369, 1992.

[93] P. J. Davis, P. Rabinowits, *Methods of Numerical Integration*, Academic Press - New York, 1975.

[94] X. Li, D. Feng, K. Chen, "Optimal Image Sampling Schedule: A New Effective Way to Reduce Dynamic Image Storage Space and Functional Image Processing Time," *IEEE Trans. Med. Imag.*, Vol. 15, p. 710-719, 1996.

[95] B. E. Oppenheim, J. D. Krepshaw, "Dynamic hepatobiliary SPECT: a method for tomography of a changing radioactivity distribution," *J. Nucl. Med.*, Vol. 29, p. 98-102, 1988.

[96] A. Kato, D. Menon, M. Diksic, L. Yamamoto, "Influence of the input function on the calculation of the local cerebral metabolic rate of glucose in the deoxyglucose method," *J. Cere. Blood Flow Metabol.*, Vol. 4, p. 41-46, 1984.

[97] S. Takikawa, V. Dawan, P. Spetsieris, W. Robeson, T. Chaly, R. Dahl, D. Margouleff, D. Eidelberg, "Noninvasive quantitative fluorodeoxyglucose PET studies with an estimated input function derived from a population-based arterial blood curve," *Radiology*, Vol. 188, p. 131-136, 1993.

[98] R. L. Philips, C. Y. Chen, D. F. Wong, E. D. London, "An Improved Method to Calculate Cerebral Metabolic Rates of Glucose Using PET," *J. Nucl. Med.,* Vol. 36, p. 668-1679, 1995.

[99] Y. Onishi, Y. Yonekura, S. Nishizawa, F. Tanaka, H. Okazawa, K. Ishizu, T. Fujita, J. Konishi, and T. Mukai, "Noninvasive Quantification of Iodine-123-Iomazenil SPECT," *J Nucl Med,* Vol. 37, p. 374-378, 1996.

[100] P. C. Chiao, E. P. Ficaro, F. Dayanikli, W. L. Rogers, and M. Schwaiger, "Compartmental analysis of technetium-99m-teboroxime kinetics employing fast dynamic SPECT at rest and stress," *J Nucl Med,* Vol. 35, p. 1265-1273, 1994.

[101] D. Feng, X. Li, and W. C. Siu, "A New Dimension in Image Data Compression: Theory and Principles for the Minimisation of Image Frames in Dynamic Biomedical Function Imaging," *IEEE Trans Med Imag,* submitted 5/1996.

[102] K. Ho-Shon, D. Feng, R. A. Hawkins, S. Meikle, M. Fulham, and X. Li, "Optimised Sampling and Parameter Estimation for Quantification in Whole Body PET," *IEEE Trans Biomed Eng,* Vol. 43, p. 1021-1028, 1996.

[103] A. Chatziioannou, M. Dahlbom, and C. K. Hoh, "Studies On the Use of Transmission Scans for Whole Body PET Attenuation Correction," *1993 IEEE Conference Record, Nuclear Science Symposium and Medical Imaging Conference,* Vol. 2, p. 1111-1115, 1993.

[104] Y. Onishi, Y. Yonekura, T. Mukai, S. Nishizawa, F. Tanaka, H. Okazawa, K. Ishizu, T. Fujita, H. Shibasaki, and J. Konishi, "Simple Quantification of Benzodiazepine Receptor Binding and Ligand Transport Using Iodine-123-Iomazenil and Two SPECT Scans," *J Nucl Med,* Vol. 36, p. 1201-1210, 1995.

[105] F. Mori and J. J. DiStefano III, "Optimal nonuniform sampling interval and test input design for identification of physiological system from very limited data," *IEEE Trans Auto Cont,* Vol. 24, p. 893-900, 1979.

[106] J. J. DiStefano III, "Optimised blood sampling protocols and sequential design of kinetic experiments," *Am J Physiol,* Vol. 240, p. R259-R265, 1981.

[107] J. V. Beck and K. J. Arnold, *Parameter Estimation in Engineering and Science*, John Wiley & Sons - New York, 1977.

[108] S. R. Meikle, B. F. Hutton, and D. L. Bailey, "A transmission dependent method for scatter correction in SPECT," *J Nucl Med*, Vol. 35, p. 360-367, 1994.

[109] Y. Narita, S. Eberl, H. Iida, B. F. Hutton, M. Braun, T. Nakamura, and G. Bautovich, "Monte Carlo and experimental evaluation of accuracy and noise properties of two scatter correction methods for SPECT," *Phys Med Biol*, Vol. 41, p. 2481-2496, 1996.

[110] Y. Narita, H. Iida, and S. Eberl, "Monte Carlo evaluation of accuracy and noise properties of two scatter correction methods," *IEEE Conference Record, Nuclear Science and Medical Imaging Conference*, Vol. 2, p. 1434-1439, 1996.

[111] J. B. Bassingthwaighte, B. Winkler, and R. B. King, "Potassium and Thallium uptake in dog myocardium," *J Nucl Med*, Vol. 38, p. 264-274, 1997.

[112] T. C. Hsung, P. K. Lun, "Denoising by Singularity Rejection" *Proceeding of 1997 International Symposium on Circuits and Systems*, Vol. 1, p. 205-208, 1997.

[113] M. I. Gurelli, C. L. Nikias, "EVAM: An Eigenvector-based Algorithm for Multichannel Blind Deconvolution of Input Colored Signals" *IEEE Trans. Signal Process.*, Vol. 43, p.134-149, 1995.

[114] D. T. Kuan, A. A. Sawchuk, T. C. Strand, P. Chavel, "Adaptive noise smoothing filter for images with signal-dependent noise" *IEEE Trans. Patt. Anal. Machine Intell.*, Vol. 7, p. 165-177, 1985.

[115] D. Yang, *Noise smoothing in direct Fourier positron emission tomography*, M.S. thesis, Illinois Institute of Technology, 1991.

[116] E. Levitan, G. T. Herman, "A maximum a posteriori probability expectation maximization algorithms for image reconstruction in emission tomography" *IEEE Trans. Med. Imaging*, Vol. 6, p185-192, 1987.

[117] S. Mallat, W. L. Hwang, "Singularity detection and processing with wavelets" *IEEE Trans. Info. Theory*, Vol. 38, p. 617-643, 1992.

[118] D. L. Donoho, "De-noising by Soft-Thresholding" *IEEE Trans. Info. Theory*, Vol. 41, p. 613-627, 1995.

[119] Zhang, et al, "FIR system identification using High Order Statistics alone" *IEEE Trans. on Signal Processing*, Vol. 42, p. 2854-2858, 1994.

[120] J. B. G. del Moral, E. Biglieri, "Blind Identification of Digital Communication Channels with Correlated Noise", *IEEE Trans. Signal Processing*, Vol. 44, p.3154-3156, 1996.